Aus dem Bereich Physiologie
Theoretische Medizin und Biowissenschaften
der Medizinischen Fakultät
der Universität des Saarlandes, Homburg/Saar

Versatile LCP surface microelectrodes for combining electrophysiology and *in vivo* two-photon imaging in the murine CNS

Dissertation

zur Erlangung des akademischen Grades eines Doktors der Naturwissenschaften

der Medizinischen Fakultät
der UNIVERSITÄT DES SAARLANDES

2020

vorgelegt von Michael Schweigmann
geb. am 08.05.1979 in Homburg

Tag der Promotion: 08.04.2021

Dekan: Prof. Dr. Michael D. Menger

Berichterstatter:
Prof. Dr. Frank Kirchhoff
Prof. Dr. Klaus P. Koch
Prof. Dr. Valentin Stein

Table of Content

Abbreviations

2P-LSM	two-photon laser-scanning microscopy (microscope)
ATP	adenosine triphosphate
AMPA	α-amino-3-hydroxy-5-methyl-4-isoxazolepropionic acid
CE	counter electrode
CNS	central nervous system
CPE	constant phase element
CSC_C	charge storage capacity (cathodic)
DAPI	4′,6-Diamidin-2-phenylindol
dpE	days post electrode surgery
ECoG	electrocorticograms
EEG	electroencephalography
EPC	electroplating condition
f	frequency
FOV	field of view
GABA	γ- aminobutyric acid type A
GFP	green fluorescent protein
GFAP	glial fibrillary acidic protein
IBA1	ionized calcium-binding adapter molecule 1
I	current
I_{CC}	constant current
I_{PC}	pulsed current
IR	infrared
LCP	Liquid Crystal Polymer
LED	light emitting diode
LFP	local field potential
RE	reference electrode
US	ultrasound
VEP	visually evoked potentials
WE	working electrode
wpE	weeks post electrode surgery
Z	impedance
|Z|	magnitude of impedance

List of Figures

List of Tables

Abstract

Neurons and astrocytes are highly interconnected and form a complex cellular network for signal processing in the brain. The electrical activity of neurons and astroglial Ca^{2+} signals are tightly coupled. Parallel recording of electrical activity and Ca^{2+} signals can help to identify the molecular mechanisms of neuron-glia communications. In this work, flexible liquid crystal polymer microelectrode arrays for electrical recordings and stimulations during two-photon laser-scanning microscopy (2P-LSM) were developed.

The arrays were designed for standard craniotomies used for cortical 2P-LSM *in vivo* imaging. Being of low weight, thin and flexible, they can be easily positioned between the dura mater and the glass coverslip. Three different designs were constructed: arrays (1) with eight circular electrodes (arranged in a matrix of three by three elements, sparing the center), (2) with sixteen circular electrodes (four by four matrix) and (3) with eight rectangular electrodes (placed in four groups of 2 single sites). The initial contact sites of gold were coated with nanoporous platinum to decrease the impedance of the electrode tissue contacts and to increase the charge transfer capability. The biocompatibility of the electrodes was confirmed by immuno-histochemistry.

Electrical recordings and Ca^{2+}-imaging were performed in mice with neuronal or astroglial expression of the genetically encoded Ca^{2+}-sensor GCaMP3. With the sixteen channel electrode arrays, an estimation of the spatially resolved electrical activity pattern within the cranial window could be described. The eight channel arrays were used in studies for simultaneous acquisition of Ca^{2+} (using 2P-LSM) and electrical signals. In addition, Ca^{2+} signals could be elicited by electrical stimulation. Using different stimulation intensities and depth of anesthesia, the change of brain activity during transition from anesthetized to awake state was investigated. In addition, the LCP technology was transferred from the cortical to a spinal cord application.

Zusammenfassung

Neurone und Astrozyten bilden ein komplexes interagierendes zellulares Netzwerk zur Signalverarbeitung im Gehirn. Dabei sind die elektrische Aktivitäten der Nervenzellen und die Ca^{2+} Signale der Astrozyten eng aneinander gekoppelt. Parallele Aufzeichnungen der elektrischen Aktivität und der Ca^{2+} Signale können helfen, die molekularen Mechanismen der Neuron-Glia-Kommunikation zu identifizieren. Innerhalb dieser Arbeit wurden flexible Flüssigkristall-Polymer-Mikroelektrodenarrays für elektrische Aufzeichnungen und Stimulationen für die Zwei-Photonen-Laserscan-Mikroskopie (2P-LSM) entwickelt.

Die Elektrodenarrays wurden für Standard-Kraniotomien entwickelt, die für die kortikale *in vivo* 2P-LSM verwendet werden. Sie sind dünn, flexibel und von geringem Gewicht und können leicht auf der Dura positioniert werden. Drei verschiedene Designs wurden konstruiert: Arrays (1) mit acht runden Elektroden (angeordnet in einer drei mal drei Matrix, ohne die mittlere Elektrode), (2) mit sechzehn kreisförmigen Elektroden (vier mal vier Matrix) und (3) mit acht rechteckigen Elektroden (angeordnet in vier Gruppen von zwei einzelnen Standorten). Die ursprünglichen Elektrodenkontakte aus Gold wurden mit nanoporösem Platin beschichtet, um die Gewebekontaktimpedanz zu verringern und die Ladungsübertragungsfähigkeit zu erhöhen. Die Biokompatibilität der Elektroden immunhistochemisch getestet.

Elektrische Aktivität und Ca^{2+} Signale wurden bei Mäusen mit neuronaler oder astroglialer Expression des Ca^{2+}-Indikators GCaMP3 aufgezeichnet. Mit den sechzehn Kanal-Elektroden-Arrays konnten die elektrische Aktivität entlang der Kortexoberfläche innerhalb der Kraniotomie charakterisiert werden. Die achtkanaligen Arrays wurden zur gleichzeitigen Erfassung von Ca^{2+} (mit 2P-LSM) und elektrischen Signalen verwendet. Darüber hinaus konnten Ca^{2+} Signale durch elektrische Stimulation hervorgerufen werden. Mit verschiedenen Stimulationsintensitäten und der Tiefe der Anästhesie (Isofluran) wurde die Veränderung der Hirnaktivität beim Übergang von anästhesiert zu wach beobachtet. Zusätzlich konnte die Flüssigkristall-Polymer -Technologie von der kortikalen auf die spinale Anwendung übertragen werden.

1 Introduction

Many different diseases (such as epilepsy, multiple sclerosis, and Parkinson's) of the central nervous system (CNS) have a great disabling impact on everyday life and cannot be cured, as of today. Injuries (such as traumatic brain injury or stroke) can also very often have long-term effects on patients, and the latter's cognitive and motor abilities can often only be partially restored. One reason is the complex cellular network in the CNS. Neurons and glial cells are highly interconnected and communicating via different pathways. By deciphering cell activities and reactions in detail, and also in combination, better therapies can be developed. Hence, it is important to develop new methods as well as combine and optimize existing methods.

1.1 The central nervous system of the mouse

The CNS of mammals consists of the brain and the spinal cord. It transits and processes sensory information, and coordinates and regulates organ functions and motion. Therefore, many different functional brain regions and complex information and modulation pathways exist (Figure 1.1, Table 1.1; Watson et al., 2012; Kandel et al., 2000; Shepard, 2004; Derdikman und Knierim, 2014). An example is the visual pathway, which starts from the retina and goes over the optic nerve, the optic tract, the lateral geniculate nucleus (LGN, a structure inside the thalamus), and ends in the primary visual part of the cerebral cortex. Some fibres leave the optic tract (before reaching the LGN) and go to the midbrain, e.g. to execute the pupillomotor reflex or eye movement. Others end in the hypothalamus (influencing the circadian rhythm) (Remington, 2012).

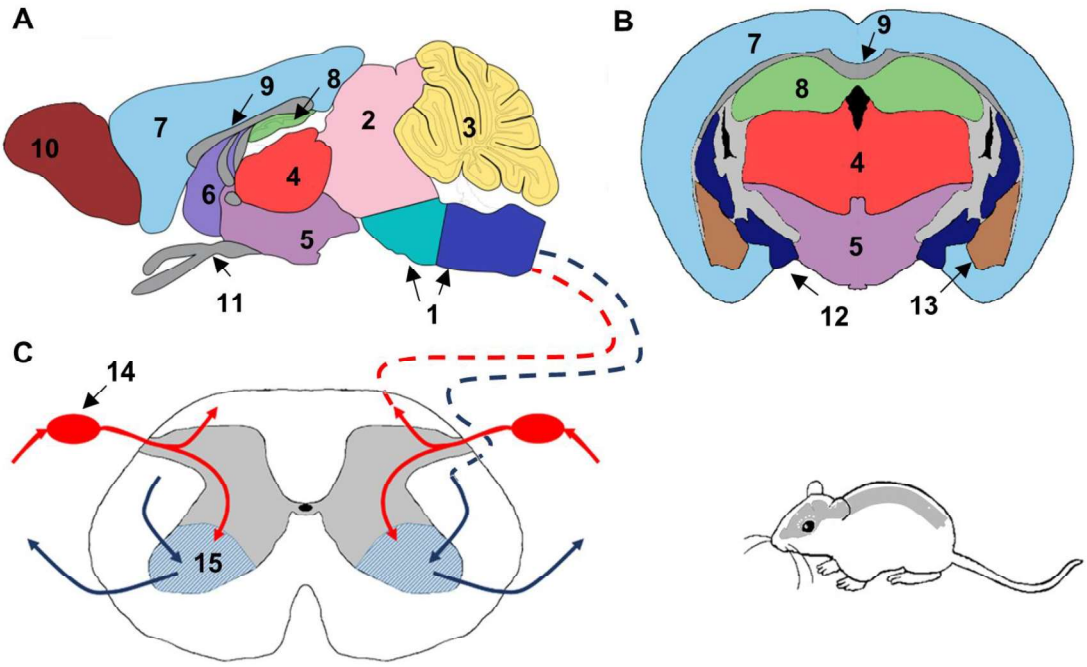

Figure 1.1: Simplified overview of the murine central nervous system with illustrations of the different brain regions in a sagittal section (A, adapted from GENSAT), a coronal section (B, adapted from Allen mouse brain atlas), and of the spinal cord with efferent and afferent fibres (C, adapted from Shepard, 2004). For numbers see Table 1.1.

Afferent fibres from the peripheral nervous system (PNS) transfer somatosensory information via the dorsal root ganglia (DRGs) through the spinal cord to the somatosensory cortex. Within the spine, DRGs are coupled with dorsal column nuclei, which have a long axon projecting to the thalamus for a first processing. Similar to the visual system, the information ends in the primary somatosensory part of the cerebral cortex (Shepard, 2004). Motor tasks involve several brain regions as well, including the cerebral (motor) cortex, striatum (part of the basal ganglia), and cerebellum. These areas have a strong interaction and interconnections with other regions like the hippocampus and thalamus. The motor outputs are fed forward via efferent fibres in the spinal cord to the ventral horns (spine output regions with motor- and interneurons), which are the relay stations to the peripheral nervous system. The DRGs are also connected to the ventral horns, so that there is a direct path between somatosensory and motor system (Kandel et al., 2000; Shepard, 2004).

Table 1.1: Selection of CNS regions (according to Figure 1.1)

No	CNS region	Functions
1	Brain stem (Medulla oblongata; Pons)	The brain stem includes several functional centres for vital autonomic functions (e.g. digestion, breathing, heart rate), and conveys neuronal signals.
2	Midbrain	Processing of sensory information and control of motor functions (for example eye movements and auditory and visual reflexes).
3	Cerebellum	Modulation of movements (force, range, learning).
4	Thalamus	Acting as relay station, first processing of the majority of the information for the cerebral cortex (from the rest of the CNS).
5	Hypothalamus	Regulation of autonomic, endocrine, and visceral functions (e.g. stomach, intestine).
6	Septum	Connection zone to the cerebral cortex.
7	Cerebral Cortex	High-level information processing (sensory, motor, associative and analytical region, sophisticated control of behaviour).
8	Hippocampus	Involved in learning, memory, and spatial navigation.
9	Corpus Callosum	Axonal fibres connecting the hemispheres of the cerebral cortex.
10	Olfactory Bulb	Olfaction.
11	Optic Nerve and Optic Tract	Axonal fibre bundle that transmits visual information.
12	Striatum	Involved in motor tasks (part of basal ganglia)
13	Amygdala	Processing fear, emotion.
14	Dorsal Root Ganglion	Transmission of sensory information to the CNS.
15	Ventral Horn	Transmission of motor information to the peripheral nervous system.

1.1.1 Neuronal organization of the cortex

The cerebral cortex of the mouse is responsible for a high-level motor and sensory information processing. In accordance with the different tasks, the cortex displays clustered areas (Figure 1.2A, Mohajerani et al., 2013). In mammals, the cortex is organized in six layers, whereas in mice, layers 2 and 3 cannot be separated (DeFelipe, 2011; Douglas and Martin, 2004). Approximately 80% of the neurons within the cortical

tissue are glutamatergic (excitatory) neurons. Pyramidal-shaped neurons are located in layer 2/3, layer 5, and layer 6, whereas star-shaped glutamatergic neurons are mostly present in layer 4 (Figure 1.2B). Pyramidal neurons are mainly interconnected within cortical areas, between different cortical areas (both hemispheres), and with the thalamus and striatum. The remaining 20% of neurons are GABAergic (inhibitory) interneurons balancing the activity of glutamatergic neurons. They are located in layers 2 to 6 and are highly interconnected within the cortex, but also receiving strong inputs from the thalamus as well. In layer 1, there is a high-density of neuronal synaptic interaction (Harris and Shepherd, 2015; Harris and Mrsic-Flogel, 2013; Thomson and Lamy, 2007).

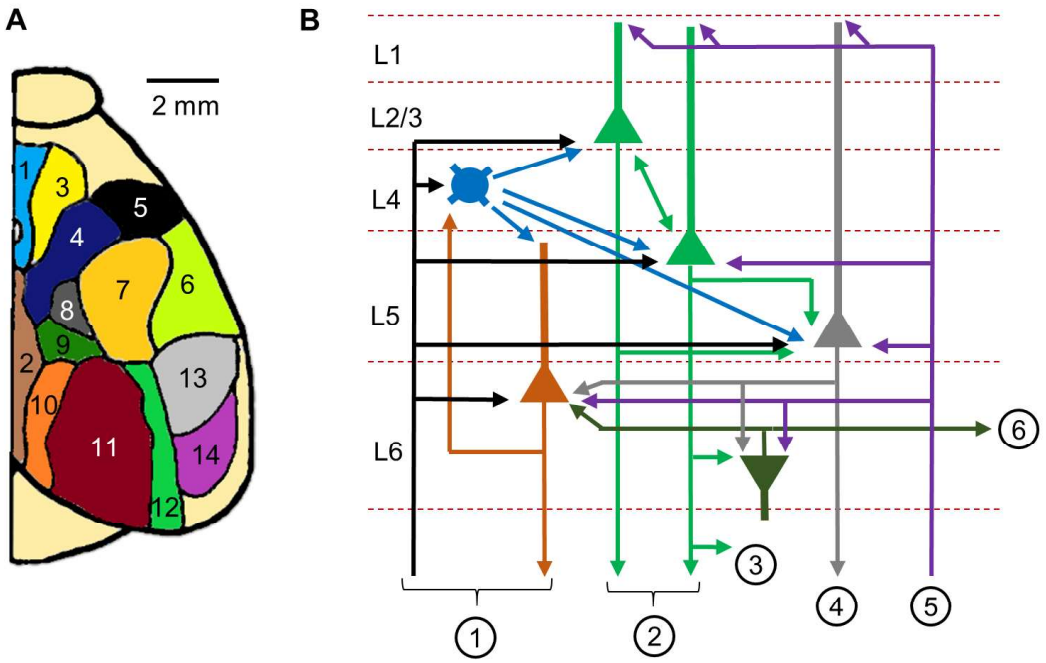

Figure 1.2: Cellular organisation and interconnection of the mouse brain. A) Areas of the cortex associated with distinct sensory of motor functions (adapted from Mohajerani et al., 2013). Cortical area: 1) secondary motor, 2) retrospenial, 3) primary motor, 4) primary hindlimb sensory, 5) primary upper lip sensory, 6) area with secondary forelimb sensory and secondary barrel sensory, 7) primary barrel sensory, 8) primary trunk and primary shoulder / neck sensory, 9) parietal association, 10) mediomedial secondary visual, 11) primary visual, 12) lateral secondary visual sensory, 13) primary auditory, 14) temporal association layer. B) Cortical layers and the complex neuronal interconnections of excitatory neurons in the somatosensory cortex (adapted from Harris and Mrsic-Flogel, 2013). ① from/to primary thalamus, ② to high-order cortex and contralateral cortex, ③ to bilateral striatum, ④ to subcerebral targets, higher order thalamus, ipsilateral striatum, ⑤ from higher order cortex and thalamus, ⑥ to "long range" cortical targets.

1.1.2 Glial cells of the CNS

Another class of cells within the CNS are glial cells. These can be found throughout the complete CNS, interacting with adjacent neurons. Different types are classified in accordance with their functionality (Figure 1.3). Related to this work are astrocytes, oligodendrocytes, and microglia.

Astrocytes:

Astrocytes are star-shaped cells interacting with blood vessels, different cells of the CNS, and neuronal synapses. Astrocytes control the blood flow through the vessels, provide energy for cell metabolism, maintain brain homeostasis, sense, and modulate neuronal synaptic transmission (Volterra and Meldolesi, 2005). Each astrocyte controls a distinct region, and they have only a small overlap (Volterra and Meldolesi, 2005). Astrocytes can communicate together over gap junctions and purinergic transmitters, prominently ATP (adenosine triphosphate) and adenosine (Volterra and Meldolesi, 2005; Fields and Burnstock, 2006; Guerra-Gomes et al., 2018). Thereby, astrocytes can spread neuronal information sensed at synapses to other astrocytes, which modulate synapses in different regions. Glial cells have not only numerous receptors for purinergic transmitters, but also for all major neurotransmitters, which make the interaction between all cells even more complex (Fields and Burnstock, 2006). For neuro-synaptic modulation, astrocytes can uptake and release neurotransmitters as “gliotransmitters” (Volterra and Meldolesi, 2005; Guerra-Gomes et al., 2018). They can increase both the excitability and the inhibition of synapses (Volterra and Meldolesi, 2005). In addition, transmission at the neuronal synapses can be modulated by the way how astrocyte processes enwrap synaptic elements of neurons (Volterra and Meldolesi, 2005). This regulates the isolation of the synaptic cleft and controls the adjacent release of neurotransmitters during neuronal communication (Volterra and Meldolesi, 2005; Fields and Burnstock, 2006).

Oligodendrocytes:

Oligodendrocytes form the myelin sheets wrapped around the axons in the CNS, which is important for fast saltatory action potential propagation (Tomassy et al., 2015; Simons and Nave, 2015; Saab et al., 2016). They have between 20 and 60 myelinating processes, which are connected to different axons (Simons and Nave, 2015). The myelinated length of axon internodes can vary in the range of approximately 20 µm and 200 µm, with up to 100 turns from the oligodendrocyte process (Simons and Nave, 2015). Apart from this very important function in bioelectrical information transmission, oligodendrocytes provide axons with lactate, which is important for the neuronal ATP

production (Simons and Nave, 2015; Saab et al., 2016). Oligodendrocytes are connected via gap junctions with other oligodendrocytes and astrocytes (Simons and Nave, 2015), and are involved in purinergic signal communication and can, for example, react to ATP released during action potential propagation with activity-dependent myelination (Fields and Burnstock, 2006; Tomassy et al., 2015).

Microglia:

Microglia are the immune cells of the CNS, which continuously survey the brain homeostasis with their fine processes (Nimmerjahn et al., 2005; Szepesi et al., 2018). Upon any insult, they become active, and rapidly change their morphological appearance. The soma gets larger and the processes shorter. In a state of high activation, they evolve into phagocytic or amoeboid microglia that have largely lost their processes (Nimmerjahn et al., 2005; Kettenmann et al., 2013). They migrate to the source of change, which could be dead cells or foreign substances. Apart from the functionality of the tripartite synapse (Volterra and Meldolesi, 2005) formed by neurons (pre- and post-synapse) and astrocytes, microglia can also modulate synaptic plasticity, and are involved in learning-related synapse formation (Jebelli et al., 2015; Kettenmann et al., 2013). They respond to synaptic activity-dependent crosstalk (released neurotransmitters in the surroundings) (Fields and Burnstock, 2006; Jebelli et al., 2015; Szepesi et al., 2018).

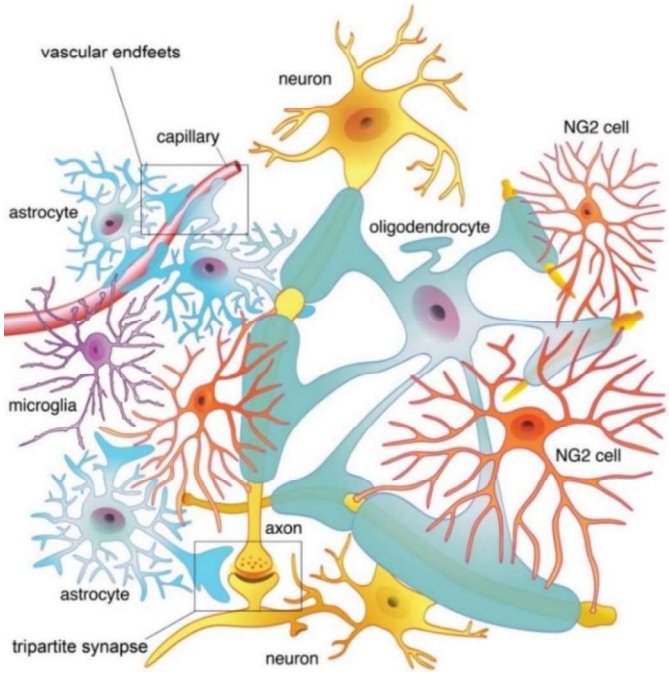

Figure 1.3: Overview of glial cells and their contact sites and positions within the CNS

1.2 Recording of electrical brain activity

1.2.1 Recordings from the surface cover mainly post-synaptic potentials

The acquisition of the electrical activity of brain tissue is performed at different levels of invasiveness, ranging from recordings at the head surface (electroencephalography, EEG) to intracellular recordings within the brain. Depending on the application, different signal amplitudes and frequency bands (Table 1.2) have to be taken into consideration for signal processing and signal evaluation (Buszáki et al., 2012; Mollazadeh et al., 2008). With electrocorticograms (ECoGs), extracellular local field potentials (LFPs) are acquired from the cortical brain surface. These extracellular fields are the superposition of the single electrical cell activity. Therefore, the LFP can contain fast action potentials as well as slow ionic processes in glial cells.

Table 1.2: Commonly used frequency bands of bioelectrical signals (Yazdan-Shahmorad et al., 2013; Martin, 1991)

Name	Frequency range
Delta	0.5 Hz – 4 Hz
Theta	4 Hz – 8 Hz
Alpha	8 Hz – 13 Hz
Beta	13 Hz – 30 Hz
Gamma	30 Hz – 200 Hz
Low Gamma	30 Hz – 60 Hz
High Gamma	60 Hz – 200 Hz

From an extracellular perspective at an excitatory synapse, the positive charges are reduced in the area of the synaptic membrane. Temporarily, this makes this area - in relation to the extracellular area of the remaining cellular membrane segments - more negative, and forms a minus pole. Since the synapse is considerably smaller than the postsynaptic region, a positive pole is formed along the postsynaptic membrane with decreasing strength. This results in an asymmetric field structure for individual neuronal dipoles. In general, LFP frequency bands are less than 100 Hz on due to non-

synchronized neuronal activities at physiological conditions. Synchronized neuronal activity can lead to higher signal frequencies in LFP recordings (Buszáki et al., 2012).

1.2.2 Anaesthetics alter neuronal activity

The administration of different anaesthetics leads to a more synchronized neural activity (Lissek et al., 2016; Land et al., 2012). “Anaesthetic agents act on different molecular targets (Solt and Forman, 2007; Nau, 2008; Sanders et al., 2008; Urban, 2008; Zeller et al., 2008), which in turn alter neuronal network activity. It is thought that isoflurane operates by increasing activity of γ-aminobutyricacid type A receptors ($GABA_AR$) and potassium channels (Franks and Lieb, 1988; Rudolph and Antkowiak, 2004; Hemmings et al., 2005; Eikermann et al., 2011). Ketamine appears to inhibit N-methyl- D-aspartic acid (NMDA) receptor activity (Rudolph and Antkowiak, 2004; Hemmings et al., 2005) and addition of xylazine, a α_2-adrenoreceptor agonist, to ketamine enhances its sedative effects (Green et al., 1981; Lu et al., 2008) and exerts anticonvulsive properties (Green et al., 1981). Finally, urethane (ethyl carbamate) appears to act on both inhibitory and excitatory molecular targets (Hara and Harris, 2002).” (Lissek et al., 2016).

1.2.3 Visually evoked potentials in mice

Mice have different photo-receptors in the retina and can see in two different wavelength (light) bands. In cones, they have s-opsin and m-opsin, enabling vision in the ultraviolet light range and in the green light range, respectively (Figure 1.4A). Rhodopsin in rods enables bright-dark vision in the same light range (Tan et al., 2015). Visually evoked potentials (VEPs) recorded from the mouse cortex are different for various stimulation light and surrounding light intensities. When the mouse is dark-adapted, already lower light amplitudes are sufficient to provoke VEPs, and the delay in the first negative wave is shorter (Figure 1.4B). With increasing stimulation amplitude, the delay of the first wave gets shorter, and the amplitude of the negative wave becomes higher and goes into saturation (Ridder and Nusinowitz, 2006).

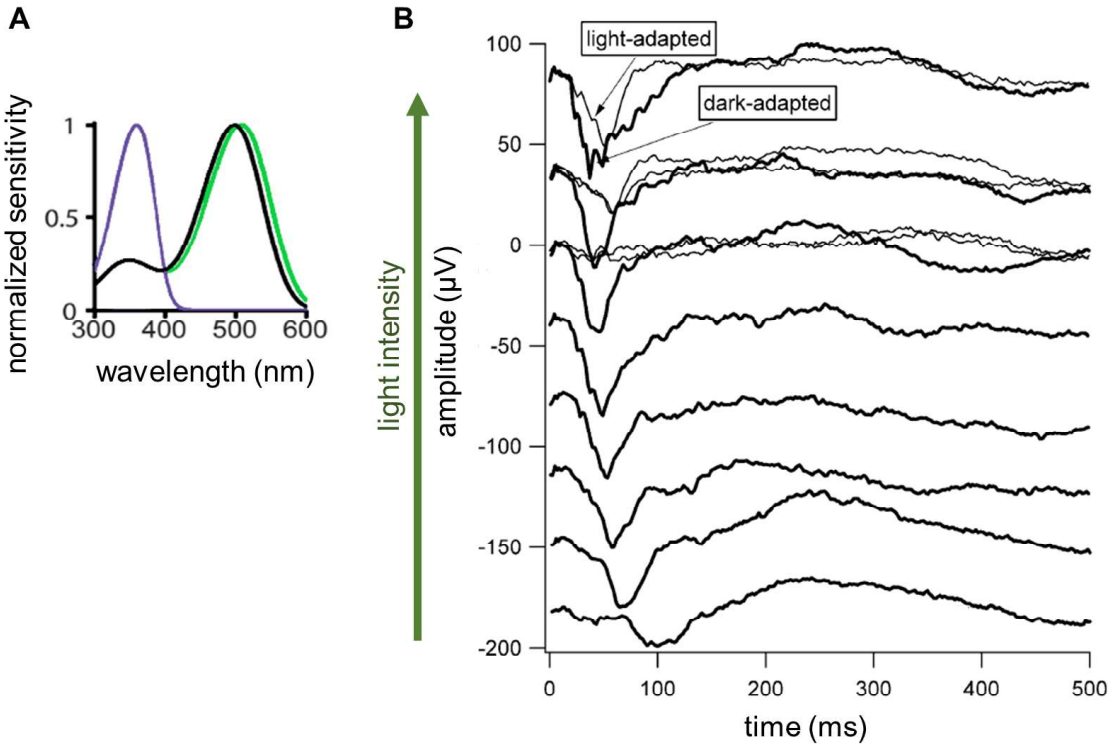

Figure 1.4: VEP response is different for various light conditions. A) Relative sensitivity in mouse vision. Purple line indicates sensitivity range of s-opsin; green line of m-opsin and black line of rhodopsin (modified from Tan et al., 2015). B) VEPs recorded from the bone over the visual cortex with a stainless steel electrode show the light dependency of the evoked potential (modified from Ridder and Nusinowitz, 2006).

1.3 Electrical stimulation of the CNS

Electrical stimulation of the CNS is used e.g. in clinical routine to treat diseases like Parkinson's disease by deep brain stimulation or depression by transcranial electric stimulation (Beudel et al., 2016; Kirsch and Nichols, 2013). In addition, first outcomes show that in case of stroke or traumatic brain injury, electrical stimulation of the brain can aid rehabilitation (Adkins, 2015). When artificially triggering neuronal action potentials with electrical stimulation, the voltage-dependent conductivity of the cell membrane for sodium ions (Na^+) is exploited. With an electric field, the extracellular ion concentration at the membrane are changed and the membrane potential is reduced. If the stimulus threshold is reached, with the opening of the Na^+ channels, an action potential is created. The interaction of the electric field and the excitable tissue is the base for artificial stimulation. It depends on the applied field and on cell orientation, cell

type, cellular structure, and the resulting field distribution generated by this anisotropic tissue (Rattay, 1998; Basser and Roth, 2000; Radman et al., 2009; Ye and Steiger, 2015).

1.3.1 Estimation of stimulation threshold for cortical neurons

It has been pointed out that for pyramidal tract neurons of the cat motor cortex, an average excitability constant of about 1290 µA/mm^2 (range about 1000 to 1550 µA/mm^2) was estimated with a stimulation pulse width of 0.2 ms (Tehovnik et al., 2006). The term average excitability constant is the ratio of stimulation current to activate 50% of the cells to the squared distance between cell and stimulation electrode (Figure 1.5A). For axons, the constant can vary between 300 µA/mm^2 (large myelinated fibres) and 27000 µA/mm^2 (small unmyelinated fibres). Stimulations in the visual cortex (V1) of monkeys were possible, with a current distance relationship of 675 µA/mm^2 (Tehovnik et al., 2006). Because these values were achieved with needle microelectrodes, a spherical current distribution around the electrode can be assumed in the first approximation, which is mainly valid in the range of approximately 100 µm to 450 µm. In closer distances, a linear relationship, and, in wider ranges, a cubic relationship between current strength and electrode distance is given for cortical neurons (Rattay and Wenger, 2010; Rattay, 2013). However, it gives an estimate which currents have to be applied for electrical stimulation. Taking a sphere surface in consideration, from the average excitability constant a current density value can be calculated using the factor 4π. The necessary current densities for stimulations can be estimated to approx. 100 µA/mm^2 for the large pyramidal neurons of the motor cortex, and 25 µA/mm^2 to 2150 µA/mm^2 for axons.

1.3.2 Time and charge dependency of electrical stimulation

In addition to the stimulation amplitude, the duration of the stimulation pulse is also important, since the artificial activation of the neurons depends on the ion shift at the membrane. The shorter the stimulation time, the higher the stimulation amplitude that has to be chosen (Figure 1.5B). Two terms exist: rheobase current, which describes the minimum current needed to evoke an action potential, and chronaxie, which describes the duration of the stimulation pulse at which twice of the minimum stimulation current is needed (Cogan, 2006). Apart from the activation of neuronal tissue, the stimulation

needs to be safe to avoid tissue and/or electrode damage. Applying a monophasic negative current/voltage will have the best outcome in stimulation efficiency, but will also corrode the electrode, which leads to tissue damage when implanted electrodes are used. To prevent this, the stimulation signal should be charge-compensated, meaning that a negative and a positive current transfer the same amount of electrical charge during stimulation (Merrill et al., 2005)

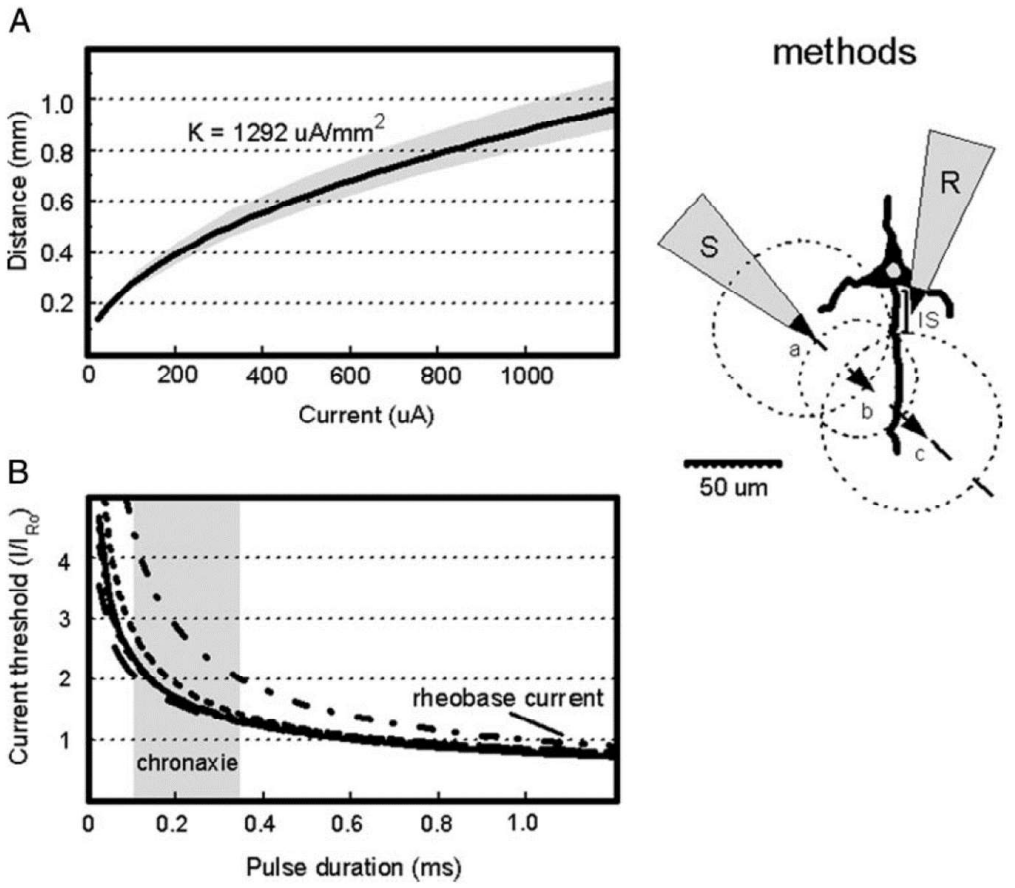

Figure 1.5: Some factors influencing electrical stimulation. A) Current to squared distance relationship of motor neurons in cats described with the average excitability constant (K). B) Relationship of stimulation pulse width and normalized stimulation threshold amplitude for six pyramidal neurons (represented by different lines). (I_{R0}: rheobase current; S: Stimulation electrode; R: recording electrode) (Tehovnik et al., 2006)

1.4 Electrodes for recording and stimulation of CNS cells

Various electrodes have been developed that can record or stimulate neuronal tissue in different applications. With scalp or epicranial electrodes over the brain, the electroencephalogram is recorded (Figure 1.6). Epidural or subdural electrodes are used to acquire the electrocorticogram (ECoG) and with intracortical electrodes LFPs and single spike activities are captured. Usually, the electrodes become smaller with increasing invasiveness because of the tissue damage. In addition, the resolution depends on the size of the electrode sites and the electrode distance to the neuronal structure. For stimulation, the situation is the same. Using small electrodes close to the neuronal structure, a lower stimulation current can be used to achieve the current density threshold for electrical tissue activation compared to large or distal electrodes.

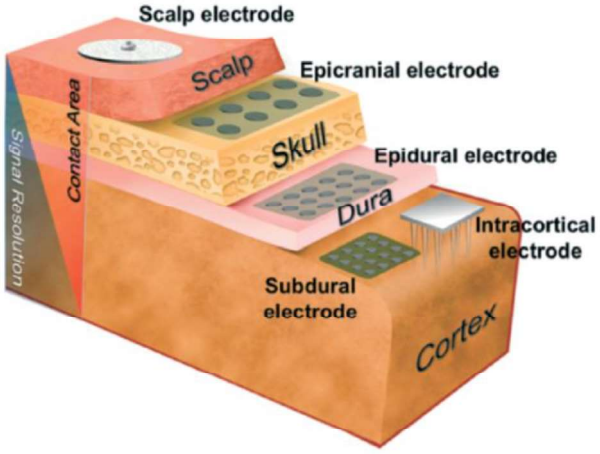

Figure 1.6: Electrode types in accordance with the position after application or implantation (Lee et al., 2016). Typically, the signal resolution can increase with the invasiveness of the electrodes.

1.4.1 Tissue response to implanted electrodes

By using implantable microelectrodes, the electrical recording and stimulation can be performed at high spatial resolution. Needle-shaped microelectrodes are used as a single device to acquire LFPs and action potentials from a single point or arranged in an array horizontal to the cortical surface. Multipolar needle electrodes enable the bioelectrical recording across through the cortex. With their implantation, however, the tissue will be damaged, and cell reactions will occur. An inflammatory process will be initiated, which will activate the reaction of microglia and astrocytes, and an astrocytic

scar will be formed around the electrodes (Minnikanti et al., 2010; Potter et al., 2012; Salatino et al., 2017). The cellular response, for example, can be reduced by using soft and flexible materials (Du et al., 2017) or by using anti-inflammatory glucocorticoid drugs such as dexamethasone to attenuate inflammatory processes (Spataro et al., 2005; Groothuis et al., 2014; Kozai et al., 2016).

1.4.2 Characterization of electrochemical properties of electrodes

When an electrode is inserted into a solution, electrochemical reactions take place at the electrode-electrolyte interface, forming a phase boundary and an electrochemical half-cell. Helmholtz described as early as in 1879 (Geddes, 1997) that under the influence of a polarizing current, an electric double layer forms between a metallic electrode and an electrolyte, with the excess ions of the electrolyte being arranged at a certain distance from the electrode. With this process, an electrode potential - the so-called open circuit potential - is formed. It can be described by the Nernst equation (Ciobanu et al., 2007).

Common techniques to characterize the electrochemical properties of the electrode are cyclic voltammetry and impedance spectroscopy (Cogan, 2008). Both techniques use a three-electrode setup consisting of a working electrode (WE), reference electrode (RE), and a counter electrode (CE) (Figure 1.7A). WE is the electrode to characterize, CE acts as a current sink, and RE is usually a high stable electrode to generate a reference point for the voltage measurements. RE is required to measure and regulate the voltage over the WE (potentiostatic approach). Cyclic voltammetry is a method to characterize the electrochemical reactions at the electrode surface and can be used to compare electrodes to their ability to drive currents. The potential at the WE is swept within the water electrolysis window and the current flow through WE is measured. Integrating the current flow over sweep time is a measure about the charge transfer capability and is called charge storage capacity (CSC) (Cogan, 2008; Kumsa et al., 2016). Hence, the cathodal part of the CSC (CSC_C) has become common practice to characterize and compare electrodes used for stimulation (Figure 1.7B).

The results of the electrochemical impedance spectroscopy describe the small signal frequency behaviour of an electrode. During the measurement, a sinusoidal voltage is applied to WE and CE, which is regulated in accordance to the measured voltage from WE to RE. The current flow through WE is measured and the impedance of WE is

calculated. The impedance of the electrode is very often presented in a diagram split in magnitude and phase (Figure 1.7C). Because of the electrochemical double layer at the electrode surface, the electrode magnitude of the impedance is lower for higher frequencies.

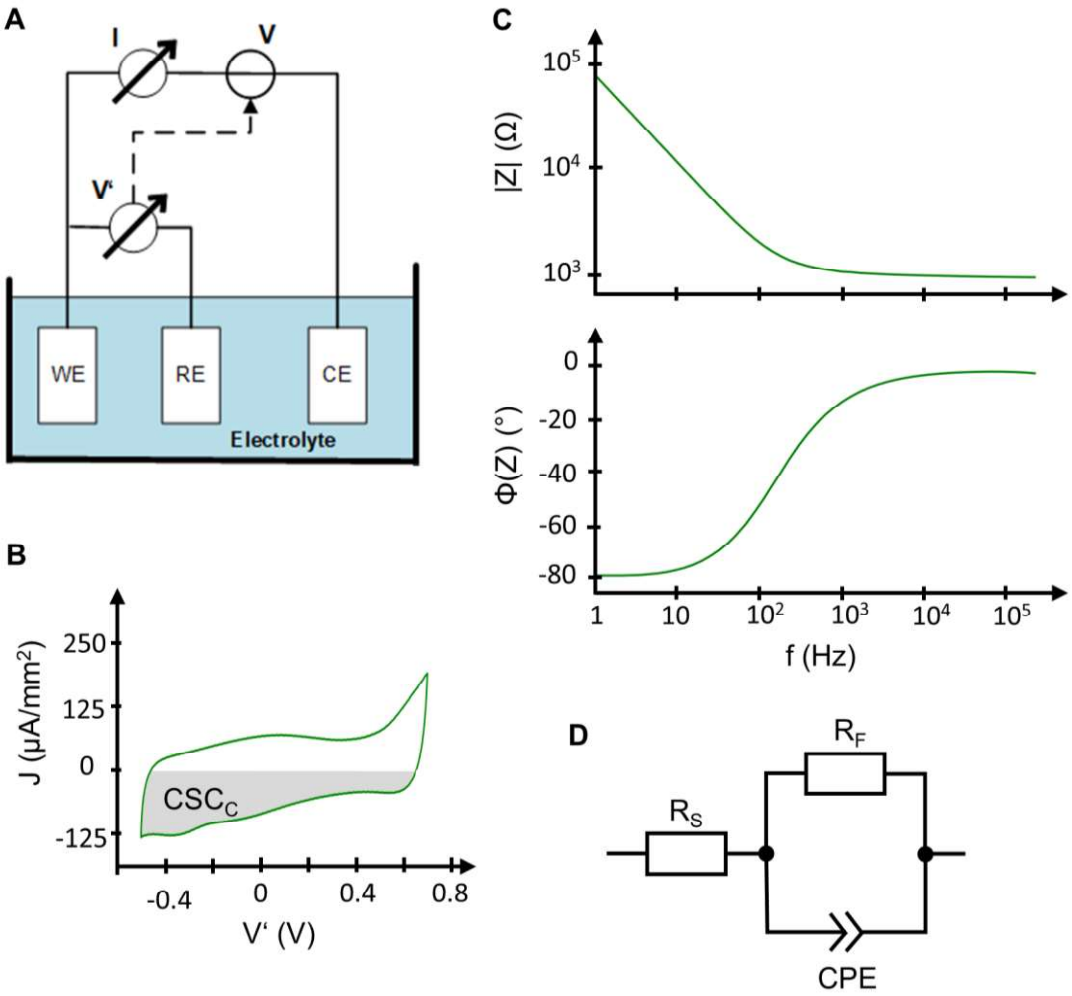

Figure 1.7: Electrochemical characterization and characteristics of electrodes. A) Three-electrode setup for potentiostatic measurements (WE: working electrode, RE: reference electrode, CE: counter electrode, I: current, V: full cell voltage V': voltage over WE [half-cell voltage]). B) Example of a voltammogram to estimate the cathodic charge storage capacity (CSC_C: grey area; J: Current density). C) Typical impedance curve of a metal electrode presented in magnitude (|Z|) and phase (Φ) (f: frequency). D) Electrode model with a constant phase element (CPE), diffusion resistor (R_F), and solution spreading resistor (R_S).

1.4.3 Electrode model

It started with Helmholtz, who described the phase boundary at the electrode electrolyte interface, followed by the development of various electrode models (Geddes, 1997). An appropriate model for metal electrodes describes the electrode impedance by using three elements. Two resistors and a mathematical construction, a so-called constant phase element (CPE), are used (Figure 1.7D). The CPE describes the phase boundary with respect to surface inhomogeneities. The resultant impedance (Z_{CPE}) is given by the empirical relationship of Eq. 3 (Franks et al., 2005). When the angle factor alpha (α) is one, CPE represents the simple Helmholtz double layer capacitance. A resistor (R_F) in parallel with CPE describes the possibility to drive direct currents, provoking Faradaic reactions. A resistor in series (R_S) describes the electrical spreading resistance from the electrode into the solution (and in some cases, added with the resistance of interconnection leads). R_S depends on the geometry of the electrode (Eqs. 1–2, Franks et al., 2005). The complete electrode impedance (Z_{El}) can be calculated with Eq. 4.

$$R_S = \frac{\rho \ln(4)}{\pi l} \quad \text{for square-shaped electrodes} \qquad \text{Eq. 1}$$

$$R_S = \frac{\rho}{4r} \quad \text{for round-shaped electrodes} \qquad \text{Eq. 2}$$

$$Z_{CPE}(f) = \frac{1}{Y_0 (j2\pi f)^{\alpha}} \qquad \text{Eq. 3}$$

$$Z_{El}(f) = \frac{R_F}{R_F Y_0 (j2\pi f)^{\alpha} + 1} + R_S \qquad \text{Eq. 4}$$

R_S: Solution resistor; ρ: solution resistivity (72 Ωcm for physiological saline (Franks et al., 2005); l: length of electrode side (square-shaped electrode); r: radius of electrode site (round-shaped electrode); Z_{CPE}: Impedance of the Constant Phase Element; Y0: Admittance magnitude of Z_{CPE}; f: frequency; j=1/√(-1); α: angle factor of Z_{CPE}; Z_{EL}: Impedance of Electrode; R_F: diffusion resistor.

1.4.4 Platinum electroplating

With the ongoing miniaturization of the electrodes to achieve greater selectivity, it is difficult to use simple metal electrodes. The electrochemical properties of traditional materials forming smooth electrode tissue connection (like thin metal foils) are not sufficient to achieve good signal recordings because of a high noise. In stimulations, electrode damage and electrolysis at the electrode-tissue interface may occur because of high current density at small electrodes (Suner et al., 2005; Szostak et al., 2017, Cogan, 2008; Merrill, 2005). To improve the effective surface area and thereby, the electrodes' electrochemical properties, nanoporous gold or platinum on the top of the electrode is quite often used. For electrical stimulation, platinum is preferred on account of the higher ability (approximately 3.5 times; Stieglitz, 2004) to drive charges over the electrode-tissue contact.

Different methods to produce highly porous platinum coatings (called platinum black) based on platinum reduction are already known and widely used (Kloke et al., 2011; Xu and Zhang, 2014; Chen and Holt-Hindle, 2010). For (electro)chemical deposition, a common approach is to use a salt of hexachlorplatinum acid dissolved in distilled water (Kloke et al., 2011; Boehler et al., 2015; Schüttler, 2007), partial completed with non-biocompatible additives to achieve higher porous surfaces (e.g. lead nitrate (Tsuei et al., 1991; Schüttler et al., 2005), copper (Boretius et al., 2011)). These additives could not be detected on the final coating, however, if they are still present and migrate to the outside, large cell responses could arise. Also, without such additives, an increase in the effective surface area in the range of factor 20–500 is still possible. In Schüttler, 2007, different manufacturing processes for the production of porous platinum layers in microelectrodes were compared. Electroplated platinum black on sputtered platinum and platinum foil were tested with the best results, using laser roughening prior to the electroplating process for both base materials because of the higher surface area.

1.5 Two-photon laser scanning microscopy in living mice

1.5.1 Two-photon laser scanning microscope

In vivo two-photon laser scanning microscopy (2P-LSM) is a common technique to observe cells or cell activity in the mouse CNS. High quality cellular signals are achieved by using high photon density at fluorescent molecules. Two photons have to arrive 'simultaneously' (within approximately 0.5 fs) at the molecules to shift outer electrons in an excited state. Falling back in the ground state generates a light emission (Helmchen and Denk, 2005). Usually, a pulsed laser system and an objective are used to focus the infrared (IR) laser beam, which scans the plane or volume to observe (Figure 1.8A). Focusing the laser beam also has the advantage of a high spatial resolution. Owing to the two-photon excitation, the wavelength of the excitation light is higher (approximately twice) than the emission wavelength. Optical filters can be used to separate the emitted light, which are detected with high-sensitive photomultiplier tubes (PMTs) from the optical path (Helmchen and Denk, 2005; So et al., 2000).

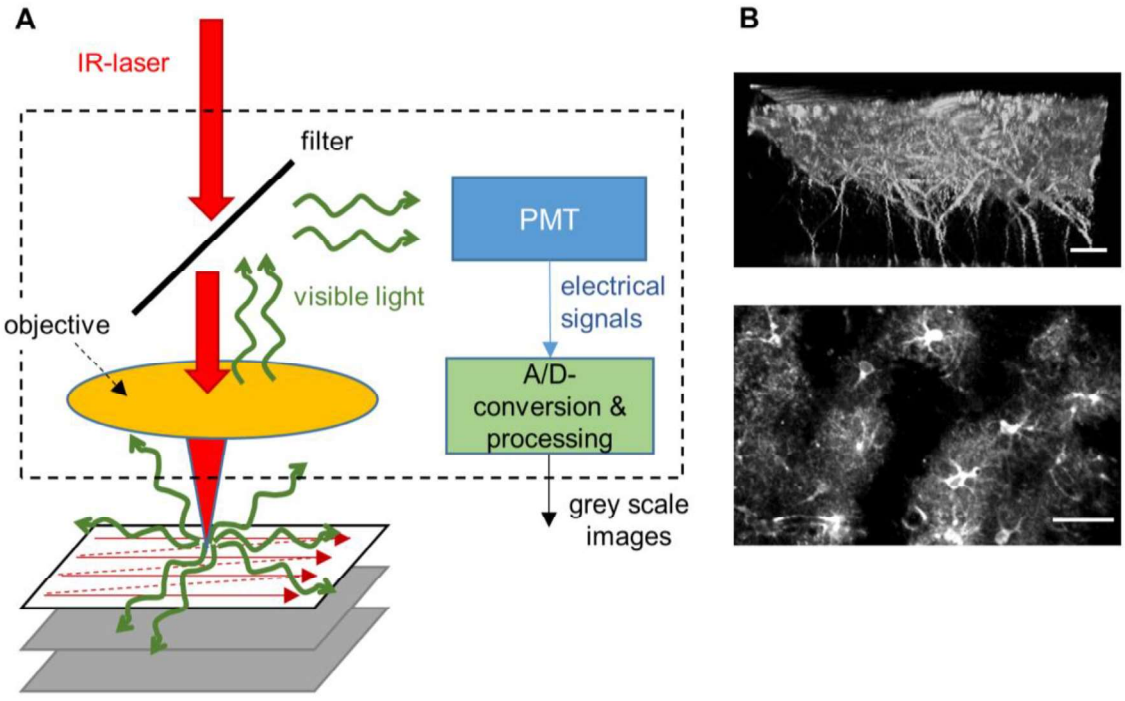

Figure 1.8: Visualizing cells and cell activity with 2P-LSM. A) Basic principle of a typical 2P-LSM device showing the paths of IR laser beam and visible light. The tissue is scanned line by line by using moving mirrors to control the laser beam. With a synchronized digitization (A/D conversion) of the photomultiplier tube (PMT) output signals the images are generated. B) Top: 3D-reconstructed image of axons in layer 1 of the somatosensory cortex showing the high interconnection of neurons. A mouse with neurons expressing a yellow fluorescent protein under the control of the neuronal Thy1-

promoter (Winter et al., 2007); (image from the Department of Molecular Physiology, CIPMM). At the bottom: maximum intensity projection of an activity-dependent time series of astrocytes in the somatosensory cortex of a mouse with astrocytes expressing the genetically encoded Ca^{2+} indicator GCaMP3 (GLAST-CreERT2 x R26-CAG-lsl-GCaMP3). The cell bodies and processes can be clearly identified and indicate the spatial coverage of each astrocyte (scale bars indicate 50 µm).

1.5.2 Ca^{2+} signalling in neurons and astrocytes

Calcium ions (Ca^{2+}) are an important cellular messenger in excitable cells (Nowycky and Thomas, 2002). Intracellular Ca^{2+} transients may occur due to the release of internal stored ions or due to influx by activation of various ionotropic receptors or Ca^{2+} channels (Nowycky and Thomas, 2002; Guerra-Gomes et al., 2018). Free Ca^{2+} ions will be stored within the cell in the endoplasmic reticulum or transported to the extracellular space with the help of active Ca^{2+} pumps and transporters (Nowycky and Thomas, 2002; Shigetomi et al., 2016). Ca^{2+} triggers or changes different cellular functions, like the release neurotransmitters at neuronal synapses (Citri and Malenka, 2008) or of gliotransmitters (for example, ATP, glutamate) from astrocytes sensing neurotransmitters (Figure 1.9) (Volterra and Medolesi, 2005; Shigetomi et al., 2016, Guerra-Gomes et al. 2018).

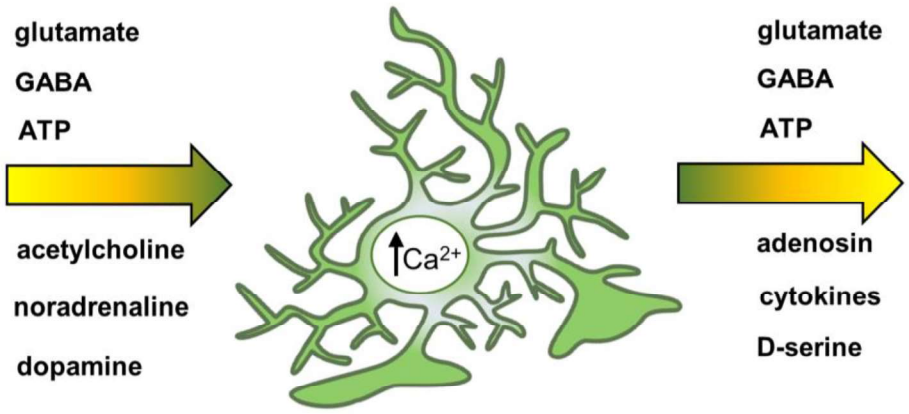

Figure 1.9: Astrocytic Ca^{2+} transients are connected with a variety of extracellular signals and can trigger gliotransmitter release (adapted from Guerra-Gomes et al., 2018 and Volterra and Medolesi, 2005).

1.5.3 Genetically encoded Ca^{2+} indicator GCaMP3

A wide range of fluorescent molecules for *in vivo* experiments are available, which can be incorporated into living cells in different ways (Richard et al., 2018). One possibility is the use of transgenic mouse lines. Morphology and/or activity of neurons and glial cells can be visualized by expressing fluorescent molecules in a tissue- and cell-specific fashion. Intracellular Ca^{2+}, as indicator of cell activity, can be investigated with genetically encoded Ca^{2+} indicators in neurons (Tian et al., 2009; Ankerboom et al., 2012) as well as in astrocytes (Shigetomi et al., 2016). They consist of a Ca^{2+}-binding domain and at least one fluorescent protein (Tian et al., 2009). A state-of-the art genetically encoded Ca^{2+} indicator is GCaMP3, which is widely used in neurons and glial cells. When Ca^{2+} is bound, it can be excited in a broad IR wavelength range (approximately 900 nm to 1000 nm) using 2P-LSM and it will emit light in the wavelength range around 510 nm (Ankerboom et al., 2012).

2 Aim

New research tools are required to gain deeper insights into the complex functionality of the mouse central nervous system (CNS). This can be achieved by developing new or improved methods or by combining known methods. For this thesis

1. electrical recording and stimulation using novel surface electrodes was combined with 2-photon laser scanning microscopy (2P-LSM) of mice *in vivo,* and

2. the overall performance of the combined system was assessed in various experimental setups.

It is a challenging to combine the different approaches in the living animal. 2P-LSM has a very high spatial resolution and allows contactless access to brain or spinal cord tissue wherever an optical path is possible. This means that a relatively large tissue volume (almost at the size of a µl) can be observed with 2P-LSM with sub-µm spatial resolution. The electrical recordings or stimulations via electrodes require direct contact with the tissue and cannot support such spatial selectivity over a large tissue volume. Therefore, a compromise must be found that allows the analysis or control of electrical cell activity within the window for 2P-LSM.

2.1 Development of novel microelectrodes

Considering the possible volume range of 2P-LSM, many multichannel microelectrodes have to be implanted into the cortical tissue or spinal cord to detect single neuronal activities within this volume. However, it is known that implantable electrodes cause inflammatory processes and gliosis around the electrodes (Minnikanti

et al., 2010; Potter et al., 2012; Salatino et al., 2017), which affect *in vivo* studies at the cellular and subcellular levels. Hypothesizing that no cell activation will occur by using surface electrodes, electrodes that can be placed on the dura will be developed (Figure 2.1). Owing to the different anatomical conditions and surgical methods to receive optical access to the brain (via craniotomy) or to the spinal cord (via laminectomy) (Cupido et al., 2014; Fenrich et al., 2012), the primary focus is on the brain. In a second step, the results will be transferred to the spinal cord.

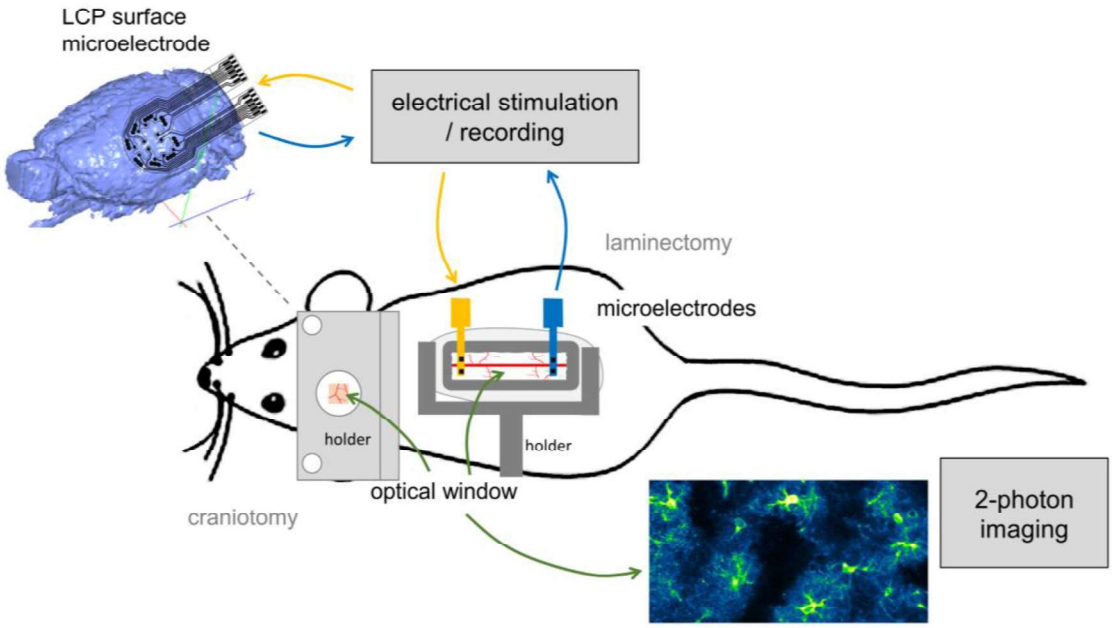

Figure 2.1: Illustration of the aim of this work. Combination of electrophysiology, using surface electrodes, and 2P-LSM to investigate molecular pathways and cellular communications in the CNS of mice under physiological and pathophysiological conditions.

2.2 Probing the biocompatibility and long-term stability

The hypothesis that surface electrodes will have no significant influence on the cellular network has to be tested. Therefore, the short-term and long-term influences of the surface electrode array on the cortical tissue of the CNS will be investigated. Inflammatory processes can be identified by analysing the responses of microglia and astrocytes. In addition, the bone regeneration of a craniotomy will be observed to determine the long-term stability of the optical window with an applied electrode array.

2.3 Linking electrical network activity and Ca^{2+} transients

In combined experiments, the parallel use of microelectrode arrays and 2P-LSM will be investigated. The cellular activity of neurons and astrocytes in genetically modified mice will be recorded by visualizing the binding of Ca^{2+} to the green fluorescent indicator protein GCaMP3. At the same time, the electrical activity of the cells resulting mainly from the ion flow of sodium ions (Na^{+}) and potassium ions (K^{+}) across the cell membrane will be recorded, or initiated with electrical stimulation. In addition, network activity will be changed by varying the depth of anaesthesia or by kainate injection into the cortex, which leads to epileptic seizures (modified after Bedner et al., 2015).

3 Materials and Methods

3.1 Surface electrode arrays

The commercially available liquid crystal polymer (LCP) technology (Dyconex AG, Switzerland; Bihler et al., 2017) was selected for the surface electrodes (Figure 3.1). It is a novel technology in the field of microelectrodes and thus under ongoing industrial development. However, the LCP technology promises a good compromise between miniaturization, costs, and availability. In addition, the industrial LCP structures are flexible, but thicker compared to electrodes made of polyimide or parylene C, making them more robust and easier to handle. The LCP technology consisted of three polymer layers, each 25 µm thick. The outer layers served as base and top insulation, which were connected with the inner adhesive layer. The electrical structure was formed with two layers of gold. An inner gold layer served as the interconnection plane and, with the outer layer, the electrode sides and solder pads were formed. Both gold layers were connected by gold vias, which were produced by a galvanic process. This means that the gold electrode sites (and solder pads) were already coated with galvanized gold. Owing to the company's confidentiality obligation, no detailed information about the technology and manufacturing processes were available. A special electrode assembling process was established to produce reliable microelectrode arrays for *in vivo* experiments. A miniaturized 18-pole plug (NPD-18-18-AA-GS, Omnetics) was soldered with a low temperature solder paste (CR11, EDSYN GmbH Europe) on the terminal pads. To improve the mechanical stability and to preclude short circuits during the animal studies, epoxy resin (TC-EP05-24, TOOLCRAFT) was used to cover the connector and pads. At the end, the electrode sites were covered with nanoporous platinum during an electroplating process (Chapter 3.2).

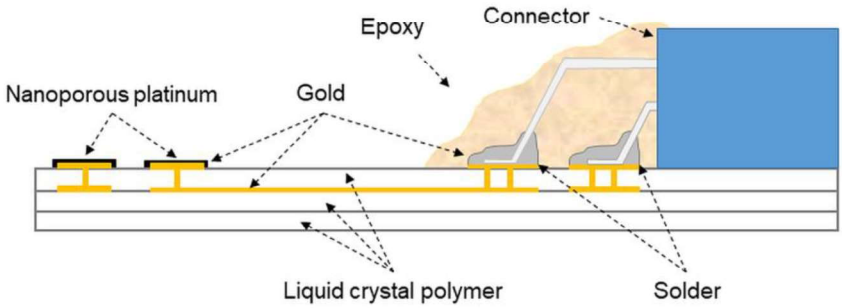

Figure 3.1: Overview of the electrode technology.

3.1.1 Numerical Simulation

To estimate how a stimulation electrode could be designed, numerical simulations with COMSOL Multiphysics V5.1 were performed. A block model (

Figure 3.2) was created to assess the electrical current distribution in the cortical tissue for different sizes of electrodes (electrode geometry in Chapter 4.1.1). The focus was on the current distribution under the electrode sites, avoiding electrode defects because of material limitations, and on the current distribution within the optical window (for 2P-LSM) enabling a direct stimulation of neurons. The model consisted of two-layers mimicking white matter and grey matter. Both were assumed as frequency-independent isotropic materials with electrical conductivities of 0.126 S/m (white matter) and 0.276 S/m (grey matter) (Datta et al. 2011). This simplification enabled the use of the model in stationary condition. A high conductive material (gold) was selected from the COMSOL database to model the electrode sites, which leads to a uniform potential distribution at each site. Due to low electrode impedances at short stimulation pulses the simulations were performed without an electrode-tissue impedance.

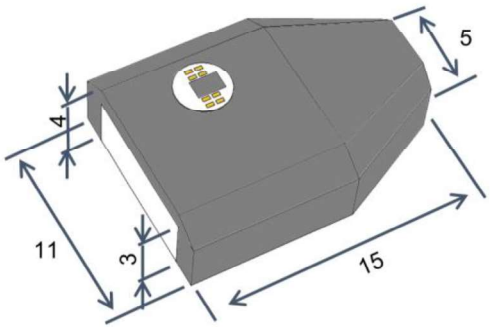

Figure 3.2: Simplified block model of the murine brain with applied electrode. The LCP base material is for illustration only and was not used in the simulation.

3.2 Platinum electroplating

3.2.1 Electroplating set-up

In order to improve the electrochemical properties of the LCP electrodes, an electroplating system was set up to apply a coating of nanoporous platinum (Figure 3.3). This included a LabView control software, a digital-to-analogue converter (NI USB-6003, National Instruments) and a voltage-controlled stimulator (ISO-STIM01D, NPI electronic GmbH). Although the ISO-STIM01D has more functions, it has always been used in voltage-controlled current mode. A large mesh electrode (platinized titanium, Jentner Plating Technology GmbH) acted as a counter electrode in the set-up for uniform current distribution. The probe and the counter electrode were introduced into the electroplating solution of 5 g hexachloroplatinic acid (H_2PtCl_6, Sigma-Aldrich Co. LLC) dissolved in 375 ml distilled water without additives. Enabling ultrasound application during the electroplating process, the solution with the electrodes was placed in a basin filled with tap water and equipped with an ultrasound module (Emmi®-12HC, EMAG AG). For a precise current-controlled process, each individual electrode site was separately galvanized.

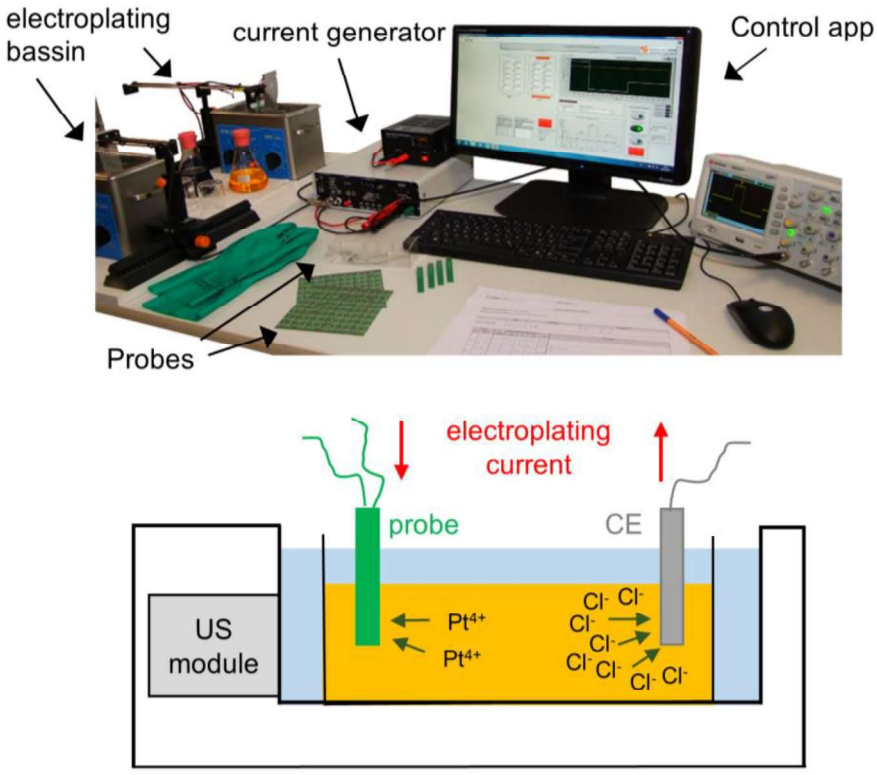

Figure 3.3: Top) Image of the electroplating set-up. Bottom) Schematic of the arrangement for electroplating (US: ultrasound, CE: counter electrode).

3.2.2 Probe preparation

To prepare the electroplating probes, individual small wires (108.301.12.36/PFA, Ø 0,0123 mm^2, Rotronik-Kabel) were soldered on the terminal pads with a low-temperature solder paste (CR11, EDSYN GmbH Europe). The connections were covered with epoxy resin (TC-EP05-24, TOOLCRAFT) for mechanical fixation and electrical insulation. A standard 2.5 mm row connector was soldered to the wires to provide an electrical connection to the electroplating and measuring system. The electrodes were electrochemically characterized by determining the electrode impedance and the cathodic charge storage capacity (CSC_C). A system was constructed with the measuring system Interface 1000 (Gamry Instruments). The microelectrode arrays were placed in the small measuring cell and connected to a multiplexer to switch manually between the single electrode sites (Figure 3.4).

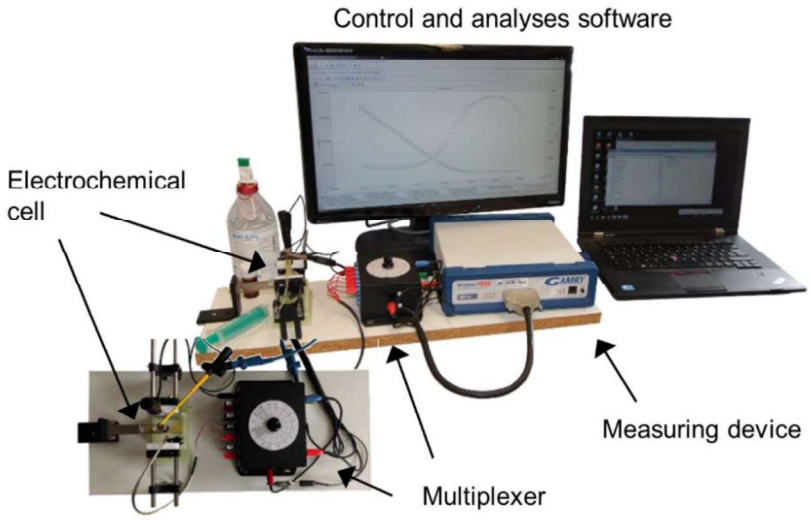

Figure 3.4: Overview of the measuring system for electrochemical characterization.

A sequence of cyclic voltammetry, observation of the open circuit potential and impedance spectroscopy, performed before and after electroplating, was used (Table 3.1). Measurements were made in 0.9% saline solution with a large stainless steel counter electrode (220 mm^2) and a silver/silver chloride reference electrode (RE-1B, ALS Co. Ltd.). The determination of the CSC_C, the electrode model parameters, and the magnitude of the electrode impedance at 10 Hz was done with the analysis software Gamry Echem Analyst V 6.20 (Gamry Instruments). The value at a frequency of 10 Hz was selected because this value was in contrast to the frequently used impedance value at a frequency of 1 kHz within the typical frequency range of

ECoG recordings. In addition to the platinum-plated electrode sites, only the solution resistance would be visible at 1 kHz. Thus, different electroplating results would not be comparable at 1 kHz, since the solution resistance depends only on the size and geometry of the electrode.

Table 3.1: Sequence and parameters for electrochemical characterization

Measurement	**Settings**	
Cyclic voltammetry	Voltage limits	- 0.7 V to 0.5 V against potential at reference electrode
	Scan speed	1 V/s
	Step size	2 mV
Open Circuit Potential	Observation time	300 s
Impedance Spectroscopy	Frequency range	1 Hz to 100 kHz 10 points per decade 5 measurements per frequency
	Measuring voltage	50 mV against open circuit potential

3.2.3 Electroplating parameters

Different conditions and parameters were tested to identify the impact of current density, current type, and electroplating duration on the LCP electrodes (Table 3.2 to Table 3.4). The round-shaped electrodes were treated with constant and with pulsed currents and the rectangular electrodes with pulsed currents. The technical parameters of the pulsed currents were chosen with respect to the current amplitudes and total electroplating charge of the constant current processes. In addition, the pulse and pause times were selected to achieve stable electrode potentials during current pulse application. The impact of ultrasound was investigated by variation of the intensity for electroplating with pulsed current of the round-shaped electrodes. For the electroplating with constant current and for the rectangular-shaped electrodes, the ultrasound module was set to 50%.

Table 3.2: Overview of electroplating parameters

Parameter	Range	Impact on
Current density	0.1 kA/m^2 to 0.4 kA/m^2	nucleation electroplating rate (mass transfer)
Current type	constant or pulsed	constant against alternating nucleation rate
Electroplating time (constant current)	30 s to 90 s	mass transfer
Pulse width (pulsed current)	0.5 s to 1 s	mass transfer
Pause (pulsed current)	1 s	diffusion time
Pulse number	60 to 120	mass transfer
Ultrasound	0%, 50%, 100%	quality, stability

Table 3.3: Electroplating conditions (EPC) for the round-shaped electrodes using constant current (I_{CC}) or pulsed current (I_{PC}). J: current density, t: constant current electroplating time, Q: calculated charge transferred during electroplating process for both methods (electrode site area: 0.018mm^2), US: ultrasound setting of the device, N: number of applied pulses during pulsed electroplating, t_1: pulse time of pulsed current, t_2: pause between two current pulses.

Constant current					Pulsed current						
EPC	**J (kA/m^2)**	**t (s)**	**Q (µC)**	**US (%)**	**EPC**	**J (kA/m^2)**	**N**	**t_1 (s)**	**t2 (s)**	**Q (µC)**	**US (%)**
I_{CC1}	0.1	60	105.0	50	I_{PC1}	0.2	60	1	1	210.0	50
I_{CC2}		75	131.3		I_{PC2}		90			315.0	
I_{CC3}	0.2	30	105.0	50	I_{PC3}	0.3	60	0.667	1	210.1	100
I_{CC4}		45	157.5		I_{PC4}		90			315.0	
I_{CC5}		60	210.0		I_{PC5}		120			424.2	
I_{CC6}		75	262.5		I_{PC6}		60			212.1	50
I_{CC7}		90	315.0		I_{PC7}		90			315.0	
I_{CC8}	0.3	30	157.5	50	I_{PC8}		120			424.2	
I_{CC9}		60	315.0		I_{PC9}	0.4	60	0.5	1	210.0	100
I_{CC10}		90	472.5		I_{PC10}		90			315.0	
I_{CC11}	0.4	30	210.0		I_{PC11}		60			210.0	
I_{CC12}		60	420.0		I_{PC12}		90			315.0	

Table 3.4: Electroplating conditions (EPC) for rectangular-shaped electrodes with pulsed current (I_{PC}). J: current density, N: number of applied pulses during pulsed electroplating, t_1: pulse width, t_2: pause between two current pulses, Q: calculated charge transferred during electroplating process for both methods (electrode site area: 0.08mm^2), US: ultrasound setting of the device.

EPC	J (kA/m^2)	N	t_1 (s)	t_2 (s)	Q (µC)	US (%)
I_{PC1}	0.2	60	1	1	960.0	50
I_{PC2}		90			1,440.0	
I_{PC3}		120			1,920.0	
I_{PC4}	0.3	60	0.667	1	960.5	50
I_{PC5}		90			1,440.8	
I_{PC6}		120			1,921,0	
I_{PC7}	0.4	60	0.5	1	960.0	50
I_{PC8}		90			1,440.0	
I_{PC9}		120			1,920.0	

3.2.4 Modelling

The evaluation of the electrode impedance with a measured magnitude value at one frequency is widely used and accepted to enable a quick comparison. A more detailed evaluation of the frequency-dependent electrode impedance was additionally performed by comparing the values of an electrode model. Therefore, the common model for metal electrodes with a constant phase element (CPE) parallel to a diffusion resistance (R_F) and a solution resistance in series (R_S) was used (see Chapter 1.4.3). The model parameters were extracted with the built-in fitting tool of the Gamry Echem Analyst V 6.20 software (Gamry Instruments).

3.3 Animal maintenance

3.3.1 Animal handling and care

All animal studies were carried out at the University of Saarland and were approved by the Saarland state's "Landesamt für Gesundheit und Verbraucherschutz" in Saarbrücken (Germany). For all surgeries and experiments under anaesthesia, isoflurane was used to sedate the animals supported by a gas flow of Oxygen (0_2) with 0.6 l/min and Nitrous Oxide (N_2O, laughing gas) with 0.4 l/min. The animals were placed on a heating plate to preserve the body temperature at normal level (approximately 35.5°C–37.5°C) and fixed with ear bars (craniotomy) or head holders (experiments). The eyes were protected from drying out by applying Bepanthen (Bayer). The animals were treated with painkillers (buprenorphin hydrochloride – 0.1 µl / 10 g body weight) and anti-inflammatory drugs (dexamethasone hydrochloride – 0.2 mg / 1 kg body weight). The health of the mouse was observed by body weight and mouse grimace scale.

3.3.2 Laboratory mice

Three different genetically encoded mouse lines, all with C57Bl/6N background at minimum age of 12 weeks, were used (Table 3.5). The mice expressed the Ca^{2+} dependent fluorophore (GCaMP3) in primary neurons or in astrocytes.

Table 3.5: List of genetically encoded mouse lines

Mouse line	Short description	Reference
Nex-Cre x R26-CAG-lsl-GCaMP3	Activity-dependent calcium indicator in neurons.	Goebbels et al. 2006 Paukert et al. 2014
GLAST-CreERT2 x R26-CAG-lsl-GCaMP3	Activity-dependent calcium indicator in astrocytes (brain).	Mori et al. 2006 Paukert et al. 2014
GFAP-CreERT2 x Rosa26-CAG-lsl-GCaMP3	Activity-dependent calcium indicator in astrocytes (spine).	Hirrlinger et al. 2006 Paukert et al. 2014

3.4 Evaluation of biocompatibility and long-term stability

3.4.1 Identification of cellular reactions

With immunohistochemistry, the cellular reactions of the tissue to the surface electrode arrays were analysed. Therefore, electrode arrays with eight round-shaped electrode sites (Chapter 4.1.1) were applied on the dura of the murine brain (GLAST-CreERT2 x R26-CAG-lsl-GCaMP3 mouse). On day 3 and day 28 after the surgery, the brain of the mice were collected, sliced, and further treated for automated microscopy (AxioScan Z.1; Zeiss Jena, Germany) of fluorescent cell staining. The standard procedure for mouse perfusion and sample preparation is given in the Appendix (Chapter 8.1) and was done by Laura Caudal (Department of Molecular Physiology, CIPMM). With the antibodies for the staining (Table 3.6 and Table 3.7), astroglial Ca^{2+}-indicator GCaMP3 (GFP), reactive astrocytes (GFAP), and microglia (IBA1) could be labelled. In addition, 4′,6-Diamidin-2-phenylindol (DAPI) was used to label the cell nuclei.

Table 3.6: Primary antibodies (bind to cell specific antigens)

Antibody	**Species**	**Dilution**	**Manufacturer**
GFP	Goat	1:1000	Rockland
GFAP	Mouse	1:500	Novocastra
IBA1	Rabbit	1:500	Wako

Table 3.7: Secondary antibodies (are fluorophores and bind to the first antibody)

Antibody	**Species**	**Dilution**	**Manufacturer**
Alexa 488 conjugated anti goat IgG	Donkey	1:1000	Invitrogen
Alexa 546 conjugated anti mouse IgG	Donkey	1:1000	Invitrogen
Alexa 647 conjugated anti rabbit IgG	Donkey	1:1000	Invitrogen

The slice images were loaded into Matlab (Matlab 2018a, MathWorks) and analysed with a customized semi-automatic script. For each hemisphere a standard eight-point polygon was manually fitted to the image covering an area of 1.5 mm^2 ± 0.1 mm^2. For quantification of the fluorescent cell images the mean values were calculated from these areas. The same polygons were used for the four staining images of one slice.

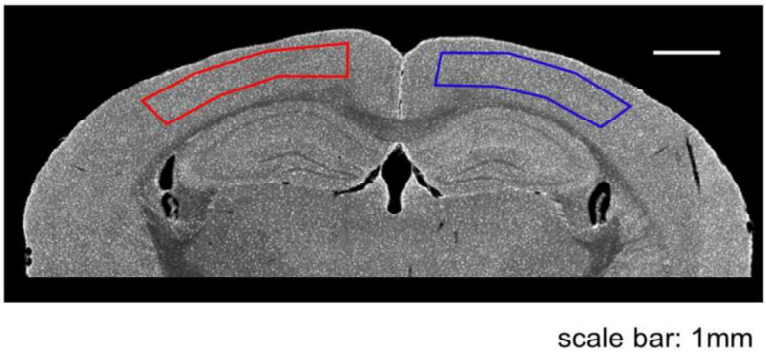

Figure 3.5: Analysed cortical regions for quantification of the fluorescent cell images in Matlab (at an example with DAPI staining).

3.4.2 Observing window transparency and angiogenesis

The quality of 2P-LSM strongly depends on the optical access to the tissue. For this reason, the transparency of the cortical window was visually observed. In addition, the angiogenesis on the electrode within the craniotomy was analysed. For this purpose, a camera (AxioCam ERc 5s, Carl Zeiss; resolution: 2560 pixel x 1920 pixel, pixel size 2.2 µm x 2.2 µm) mounted on a stereomicroscope (Stemi 2000-C, Carl Zeiss) was used. With the ZEN-Software (ZEN 2.3 (blue edition), Carl Zeiss) single images were captured and saved without any image processing. With a customized Matlab tool (Matlab 2018a, MathWorks), the angiogenesis was automatically analysed. The influence of dexamethasone was investigated, because former experiments within the department indicated that dexamethasone hydrochloride could have a positive influence on window transparency. For this study, three different dexamethasone protocols were used (Table 3.8).

With a custom-made tool to analyse the angiogenesis (Figure 3.6) on the electrode surface, the original images (A) were loaded into Matlab, split into the three different colour channels (red, green, blue), and converted to grey-scale images (B). Because no structural information were visible, with the red channel, image masks were

generated by detection of the round electrode head and brightness thresholding (C). The other two channels were averaged and used for vessel detection. A median filter (45 pixel x 45 pixel; Appendix Chapter 8.3) was applied to increase the intensity of the electrode interconnection tracks, which were also visible on the images, in contrast to the vessels (D). Median filtering is a typical processing method to reduce small “foreground” information e.g. noise (Najarian and Splinter, 2012). These background images were used to calculate the difference images from the averaged channels (E). After masking and binarization (F), the number of bright pixels was counted and the area covered by the vessels were calculated (G).

Table 3.8: Dexamethasone groups to study the angiogenesis on electrodes

Dexamethasone group	**Administration of dexamethasone**
1	No dexamethsone
2	Dexamethasone in the first 3 days after surgery
3	Dexamethasone in the first 3 days after surgery and every 7th day

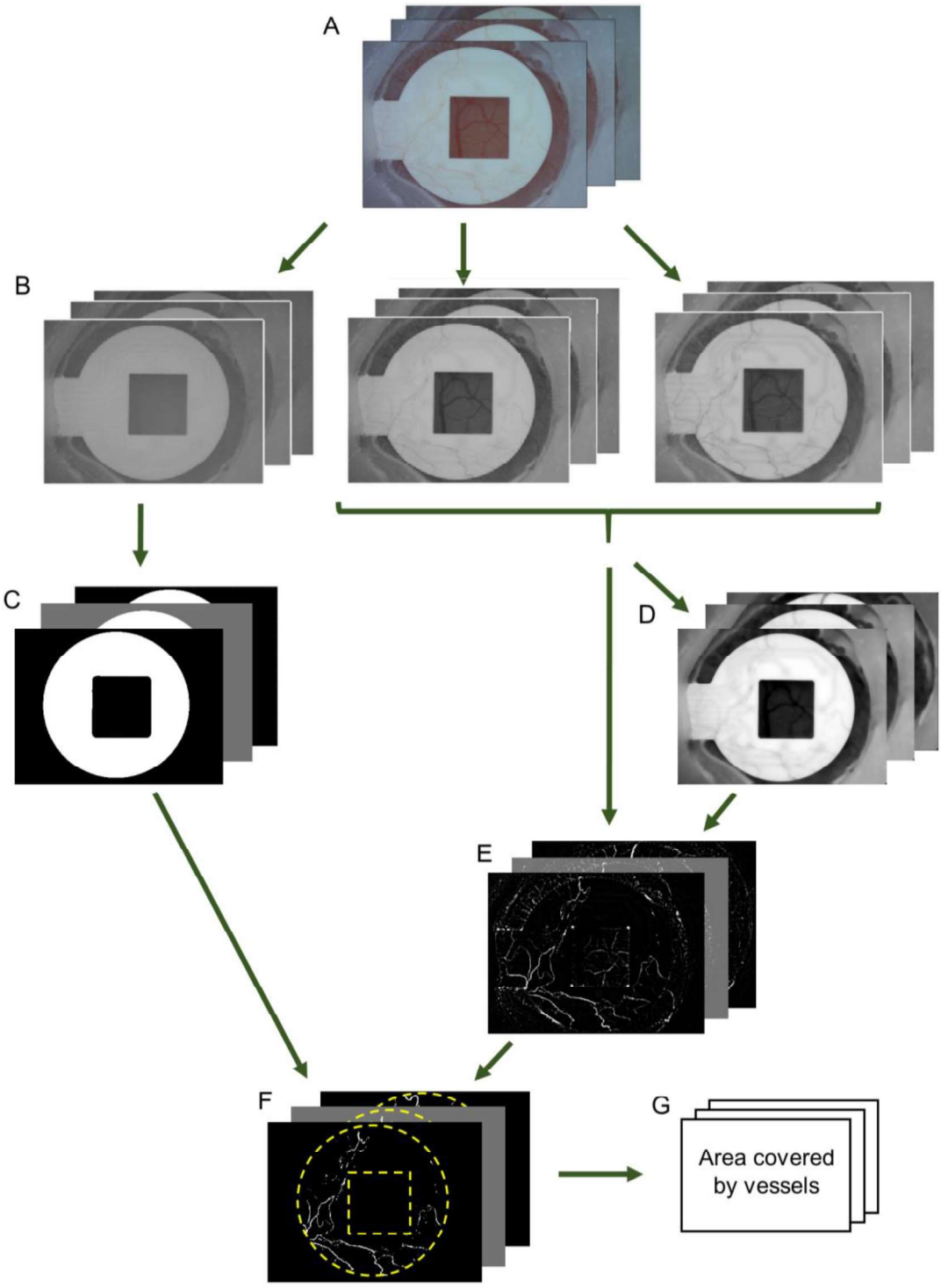

Figure 3.6: Processing steps of the Matlab tool to analyse the angiogenesis on the electrode surface. A) Original images with reddish vessels on the electrode surface. B) RGB images of A converted in grey scale images. C) Generated masks from the image of the red channel. D) Images after median filtering of the mean images from green and blue channel. E) Substraction image of B (mean image if green and blue channel) and C. F) Final image after binarization and masking. G) Determination of the area covered by blood vessels.

3.5 Two-photon laser-scanning microscopy

In vivo 2P-LSM was performed with a four-channel custom-made device (Figure 3.7; block diagrams of device and filter settings is given in Appendix Chapter 8.2) controlled by the software ScanImage (SI 2017b). The excitation wavelength of the IR-Laser was 910 nm (generated of a tuneable Chameleon Ultra II Laser, Coherent) and focused with a 20x water-immersion objective (W Plan-Apochromat, Carl Zeiss). For Ca^{2+}-imaging, the photomultiplier tube H10770PB-40 (Hamamatsu) was used. The sizes of the images and the scanning speeds were changing in accordance with the field of view (FOV), but the resolution was always set to 0.5 µm x 0.5 µm pixel edge length. Independently of the number of recorded channels, the 2P microscope was equipped with all optical filters.

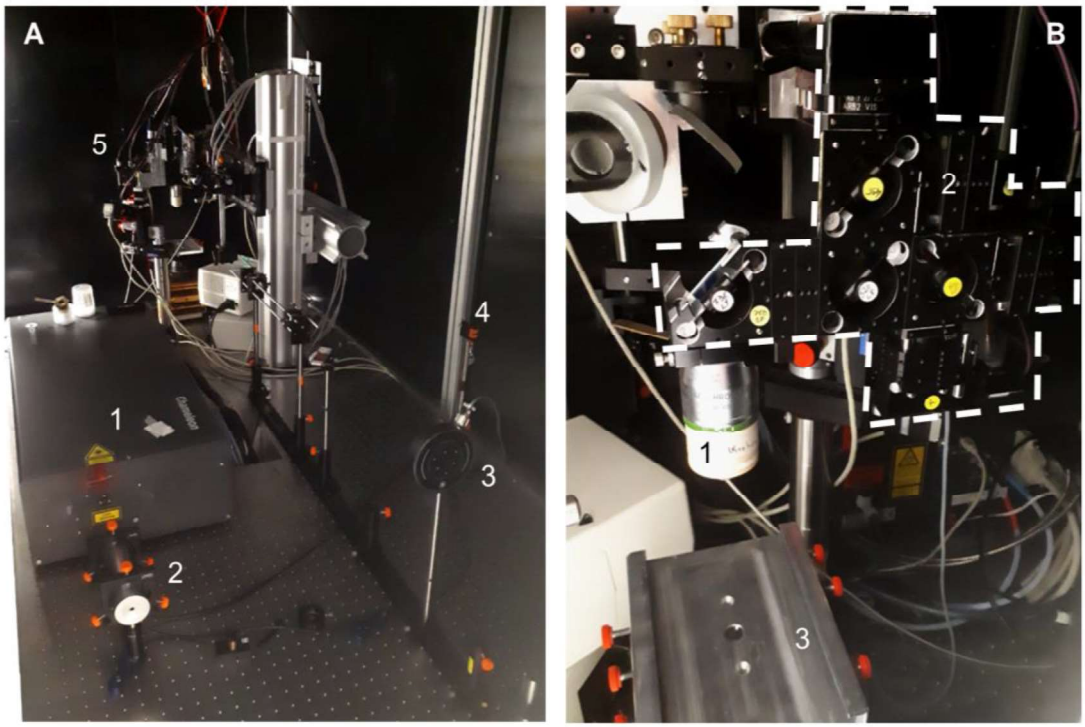

Figure 3.7: Custom-made two-photon microscope. A) Overview of main components inside the microscope cabinet. 1) Laser; 2) Pockels cell for laser power control; 3) shutter to enable tissue excitation during imaging; 4) photodiode for calibration; 5) scan head providing the interface for *in vivo* 2P-LSM. B) Optical recording unit of the scan head. 1) Objective; 2) filter and photomultiplier tube unit (four channels); 3) mouse table base.

Image processing was done with Matlab 2018a. In the first step movement artefacts of the acquired time series were reduced with a pixel-based correlation algorithm to align the single images (Evangelidis and Psarakis, 2008). In the second step, for astrocytic Ca^{2+} related signal the custom-made software MSparkles (developed by G. Stopper, Department of Molecular Physiology, CIPMM) was used to automatically identify and to classify single Ca^{2+} transients. For neuronal Ca^{2+} related signals a customized script was used to select the pixels inside single cells or along a line and to calculate the mean image brightness. In additional steps, Matlab was used for parameter extraction and visualization.

3.6 Technical equipment for electrophysiology

3.6.1 Set-up for recording of the electrical activity

Two recording set-ups were used. The first was a 16-channel recording system while the second was a commercial four-channel recording system with integrated stimulation module (PowerLab 26T, ADInstruments, amplitude resolution: 16 Bit).

The first recording system (Appendix Chapter 8.4) was built with a 16-channel biosignal amplifier (g.USBamp, g.tec medcial engineering) and a self-developed recording software (Matlab / Simulink, MathWorks), which was running on a commercial personal computer (CPU: i7-4770HQ 3.4 GHz, main memory 8 GB RAM, hard drive: SSD SATA 6 Gb/s, Windows 7). The recording device was connected via a USB 2.0 link and the signals were acquired with 1.2 kS/s. For each input user-selectable input filters were assigned, which were chosen with a band pass filter of 0.5 Hz to 250 Hz and a notch filter of 50 Hz. An additional preamplifier (g.HEADstage, gTec) to avoid input saturation of the biosignal amplifier from the electrodes' open circuit potential was used. The recording software collected and stored the signals. The electrical brain activity could be visualized in the time domain as well as in the frequency domain. In combined experiments with 2P-LSM or stimulations (electrical, visual), one or two input channels were used to acquire synchronization signals. No filters were applied to the synchronization signals. Matlab 2018a was used to visualize and analyse the signals after recording.

3.6.2 Set up for electrical stimulation

The stimulation system was constructed with a commercial available stimulator (ISO-STIM 01D, NPI electronic) connected via a digital-to-analogue output card (NI PCI-6723, National Instruments) and a self-developed control software (LabView, National Instruments) running on the same personal computer as the software for the recording device. For synchronization purposes with the recording system or with the two-photon microscope, a second output channel of the analogue output card was used. The output sampling rate was always set to 100 kHz.

3.6.3 Set up for visually evoked potentials

Visually evoked potentials (VEP) were generated by using a round green light emitting diode (LED) with a peak wavelength of 505 nm (bluish green colour) and spectral half wavelength of 40 nm (MCL053BGC, multicomp). The LED was covered with a black tube, which was used to hold the same distance (2 cm) to the mouse eye and to minimize light artefacts using the LED during 2P-LSM. The electrical recordings were performed with the multichannel recording system (Chapter 3.6.1), and in recording-only studies, the mice were placed in a Faraday cage. With this, the electrical noise of the surroundings could be minimized. After initial experiments, the minimal light conditions could be estimated (see Appendix Chapter 8.5). The stimulation device described earlier was used to drive the LED currents. Matlab was used to analyse the evoked potentials by calculation of the energy equivalent of the VEP in total (Eq. 5) and separated in the different frequency bands after a fast Fourier transformation was done (Figure 3.8).

$$E = \frac{1}{\mathrm{f}_S} \sum_{i=1}^{n} |x_i|^2 \qquad \text{Eq. 5}$$

E: Equivalent of signal energy; f_s: sampling rate of the acquisition; x_i: one ECoG sampling point; n: total number of sampling points

3.6.4 Visually evoked potentials in mice after cuprizone-induced demyelination

Cuprizone is a copper-chelating toxin that selectively affects oligodendrocytes and induces demyelination in mice when administered with food. It influences the cell metabolism with a continuous, but not completely understood, process, and leads to the death of oligodendrocytes as long as the food is administered. Remyelination starts within a few days after the re-administration of normal food and goes on for approximately two weeks (Linder et al. 2007). For food preparation, a mixture of 1.5 g (0.3 %) or 1 g (0.2%) cuprizone powder, 500 g high nutrient power food, and 350 ml water was mixed, pressed, dried, and stored at 4°C. The mice had unrestricted access to food. To check whether the VEP could be used to identify an ongoing demyelination, ECoG were compared in mice fed with cuprizone and with normal food. Cuprizone feeding started with the 0.3% mixture one week after surgery and was maintained for one week, followed by the 0.2% mixture for two weeks. VEPs were recorded twice per week per mouse.

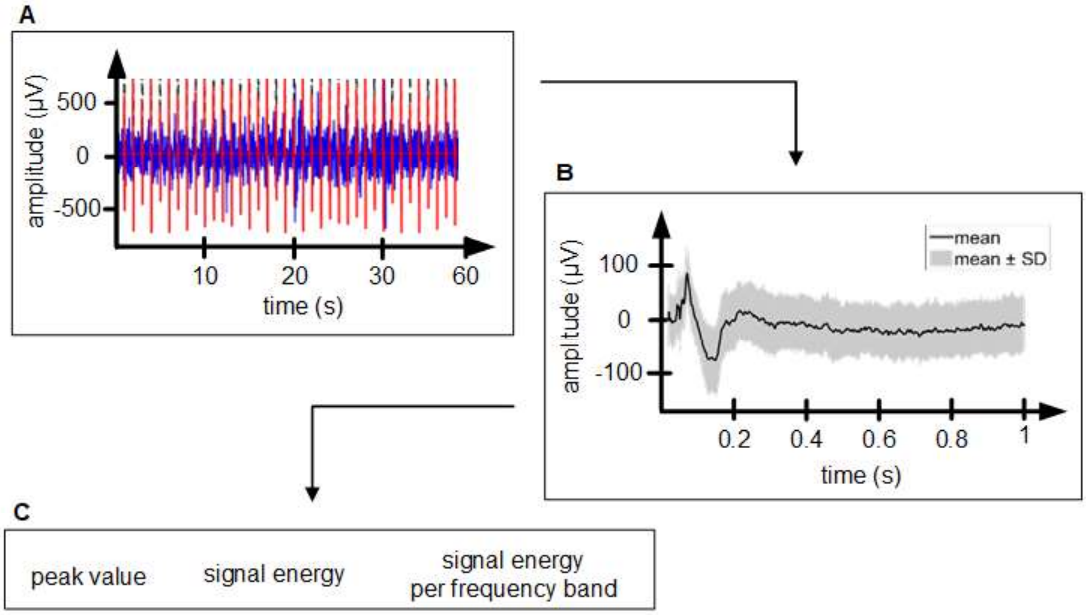

Figure 3.8: Calculation of the energy equivalent of the visually evoked potentials. A) Recorded ECoG (blue) and the stimulation synchronization signal (red). B) Calculated VEP by signal averaging in accordance to the stimulations single stimulations. C) Identification of peak value, calculation of the energy (area under squared VEP) and calculation of the signal energies per frequency band after fast Fourier transform.

4 Results

4.1 Cortical surface electrode arrays

4.1.1 Electrode design

Three different electrodes were designed for the stimulation and recording of the brains' electrical activity (Figure 4.1A, B). Arrays with (1) 16 circular electrodes (four-by-four matrix), with (2) eight circular electrodes (arranged in a matrix of three-by-three elements, sparing the centre), or with (3) eight rectangular electrodes (placed in two groups of four single sites) providing different main properties. Electrodes (2) and (3) had large optical windows to enable 2P-LSM in large tissue regions. The round electrode heads were 3 mm in diameter for the eight channel electrodes and 4 mm in diameter for the 16-channel electrode. These values were selected with respect to the size of the standard craniotomies and the necessary space for the electrode sites. The catwalk of each electrode array had a length of 3 mm and a width of 1.1 mm. The same nanoconnector was used for all electrode arrays, therefore the size of the connector pad area was 8.2 mm x 7.4 mm for each one. The distance between the electrode sites and the optical window as well as the round-shaped electrode site sizes were chosen as per the manufacturer's minimum recommendations. For the 16-channel array, the arrangement of the round-shaped sites was chosen uniformly spaced (centre–centre distance: 750 µm). The electrode size and the electrode gap were adapted to the eight-channel electrode array. The size and arrangement of the rectangular-shaped electrode sites (two groups of four 400 µm x 200 µm electrode sites) were chosen in accordance to the simulation results. The electrode sites can be used in single electrode configuration for a higher selectivity, or connected together generating a

broader and more uniform current distribution. A good compromise in terms of selectivity and current transfer capability was found.

One or two additional wires could be soldered to the 18-pin connector (Figure 4.1C) when using additional ground or reference electrodes. With the epoxy resin, the connector and the additional wires were well secured. A scanning electrode microscope was used to visualize the surface structure of the electrode sites (Figure 4.1D). The site surface indicates a stable rough surface with a ball-like structure. After the experiments, no gold or platinum remnants were observed on the brain of a mouse. The white LCP base structure of the electrode, which reflects most of the IR laser beam of the two-photon microscope, enabled an easy access to the window for imaging. But due to the laser focusing for high-resolution two-photon excitation (So et al., 2000; Helmchen and Denk, 2005), a shadowing effect decreased the accessible area with increasing imaging depth (Figure 4.1E). The strength of this effect depended strongly on the physical properties and settings of the microscope. With a window edge length of 1 mm, an imaging depth of 400 µm was estimated for a FOV edge length of 512 µm. When the FOV size was chosen smaller, the imaging depth could be increased.

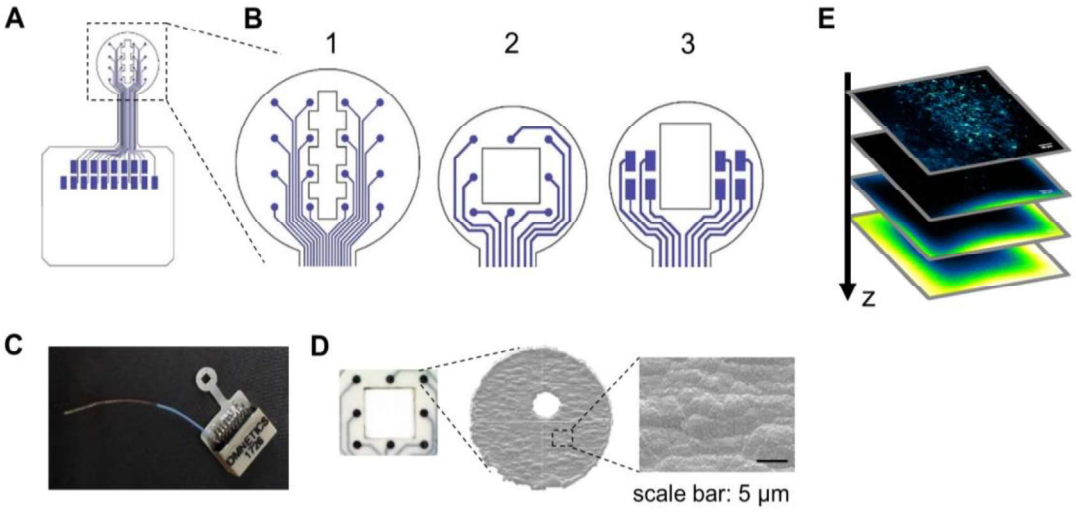

Figure 4.1: LCP electrodes for cortical application. A) General design of the surface electrode array consisting of the round-shaped electrode head, the connector area and a small catwalk enabling the application of the electrode head inside a craniotomy. B) Designs of the three different electrode heads. (1) sixteen-channel electrode with focus on recording, (2) eight-channel electrode with focus on combined 2P-LSM and electrical recording and (3) eight-channel electrode with focus combined 2P-LSM and electrical stimulation. C) Image of an assembled electrode array with one additional wire to connect a separate ground-electrode. D) Eight-channel electrode head and scanning electrode microscope image of one electrode site, showing the surface structure. (E) Example of shadow effect due to the laser focusing. The surface of the electrode around the window reflects the laser beam whereby the detectable tissue area decreases with the imaging depth. The IR reflection is visible as bright border.

4.1.2 Current density reduction by enlargement of electrode sites varies within the cortical tissue

Numerical simulation with COMSOL Multiphysics was used to estimate the current distribution under the electrode and within the cortical tissue supporting the electrode design process (Figure 4.2).

In a first simulation a configuration with two electrode sites, varied in size, was used in combination with a constant current of 200 µA. After current application to the electrode sites, the current did not enter the tissue homogeneously (Figure 4.2A). This effect was already described as edge effect (Wang et al., 2016). At the electrode edges, the current density and the material stress were highest at these locations. With an increase in the distance to the electrode (direction into the tissue), the edge effect in the current distribution decreased. The stress to the electrode sites could be reduced by selecting larger electrode sites. However, this resulted in a general decrease in the current density under the electrode, and a higher current would have been necessary enabling electrical stimulation.

In order to obtain information about the relationship between the residual current density and the electrode geometry, the current density was calculated for different electrode sizes (Figure 4.2A, B). The analysis was performed by increasing the electrode width from 50 µm to 400 µm or 600 µm (electrode site length 400 µm) and by increasing the electrode site length from 100 µm to 400 µm or 600 µm (electrode site width 400 µm). The results showed that the residual current density under the electrode was much lower than in the FOV, and that the reduction decreased with increasing distance. The effect of the increasing electrode site length on the current distribution in the field of view was less than the influence of the electrode site width. The difference between the current density in the tissue under the electrode and the tissue below the electrode window decreased with larger electrode sites. This could be important for a safe stimulation considering electrode stability and tissue damaging (Merrill, 2005). Based on these results and to create a more flexible electrode design, the size of a single electrode was determined to be 200 µm x 400 µm. These were arranged in two groups of four electrodes each to the left and right of the electrode window. Thus, it was also possible to generate larger electrodes by using two or four electrodes together (Figure 4.2C). Additionally, it was possible to use the electrode sites with different currents to influence the area of direct electrical activation.

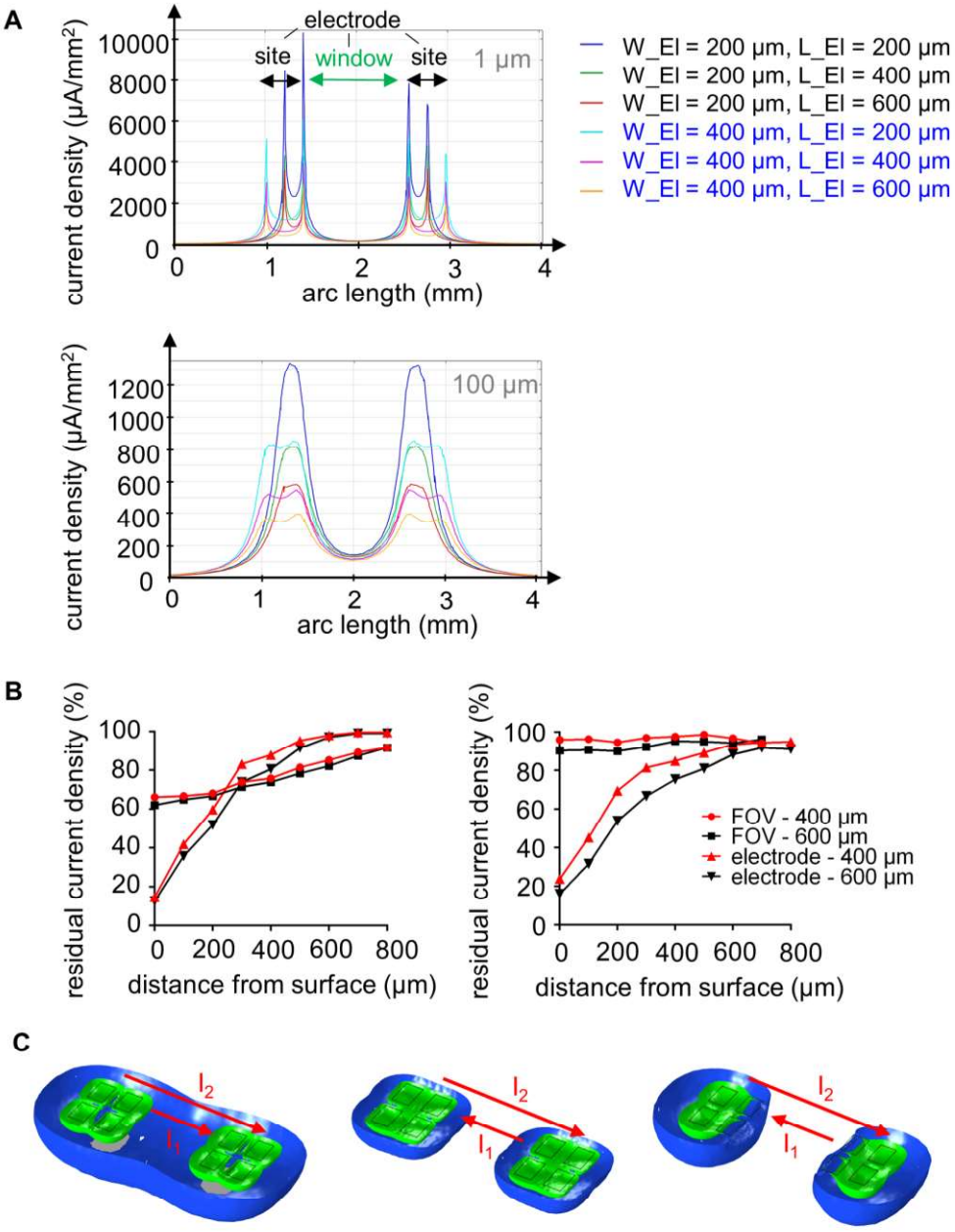

Figure 4.2: Current density distribution in numerical simulations. A) Current density distribution with used current of 200 µA along two straight lines (1 µm and 100 µm below the surface) across the electrode sites and FOV in a two electrode site configuration. B) Analysis of the residual current density in the middle of FOV and of electrode sites for different distances from the surface into the cortical tissue. Left: change of the electrode width from 50 µm to 400 µm or 600 µm (electrode length 400 µm). Right: change of length of electrode from 100 µm to 400 µm or 600 µm (electrode width 400 µm). C) Examples of current distribution using different electrode stimulation currents. Blue surface represents the area where a current density of 100 µA/mm^2 was calculated, green surface represents 500 µA/mm^2. I_1: current between the inner electrodes, I_2: current between the outer electrodes. Left: the outer and the inner electrodes drive the same current (I_1=I_2=30 µA). Middle: the inner electrodes drive the inverse current of the outer electrodes (I_1=I_2=30 µA). Right: inner electrodes drive a current with lower amplitude than the outer electrodes, which flows in the opposite direction (I_1=10µA, I_2=50 µA).

4.2 Platinum electroplating improves the electrochemical characteristics of the LCP electrodes

4.2.1 Application of ultrasound prevents coating defects

During the electroplating processes with current densities above or equal to 0.3 kA/m^2, gas bubbles were clearly visible on the surface of the electrode sites (Figure 4.3A). The bubbles generated by water electrolysis isolated the surface. This led to an inhomogeneous and incomplete platinum coating of the electrode surface. Holes of different sizes were created in the platinum layer, reducing the stability of the coating. In addition to the defects visible immediately after the electroplating process, the electrochemical characterization also blasted off parts of the coatings and increased the size and number of the defects (Figure 4.3C, D). With the use of ultrasound, the bubbles could be immediately removed from the surface and the platinum electroplating could be performed over the entire electrode surface (Figure 4.3B).

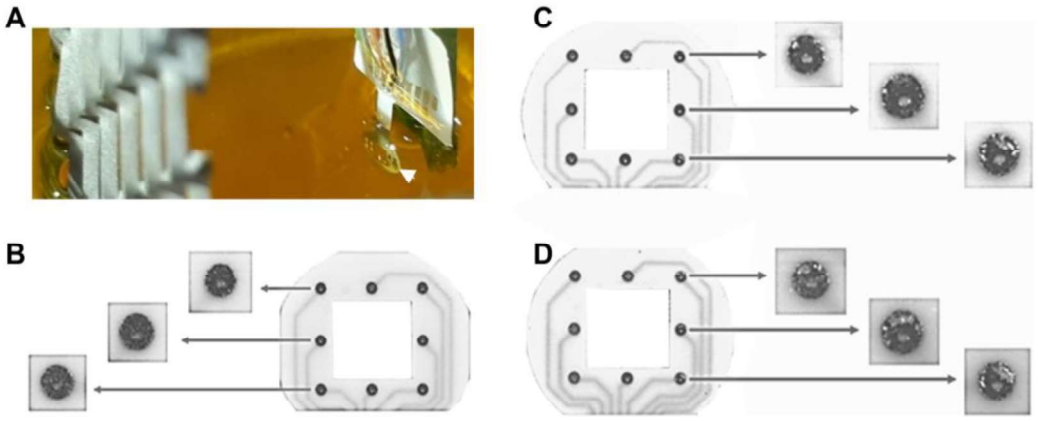

Figure 4.3: Gas bubble formation during electroplating process. A) Rectangular-shaped electrode during an electroplating process with a high current density of 0.5 kA/m^2 provoking a large hydrogen bubble on the electrode contact (white arrowhead). B - D) Differences in platinum electroplating with and without US at a current density of 0.3 kA/m^2 applied to round-shaped electrodes. B) Electrode sites after electrochemical characterization if US was used. C) Electrode sites prior electrochemical characterization if no US was used. D) Electrode sites of C) after electrochemical characterization.

4.2.2 Electroplating with constant current is highly parameter-dependent

Electroplating of the electrode sites from the round shaped electrode with constant current was done with four different current densities ranging from 0.1 kA/m^2 to 0.4 kA/m^2 (see Chapter 3.2.3). The electroplating time was between 30 s and 90 s, in steps of 15 s or 30 s.

The impedance magnitude at a frequency of 10 Hz ranged (over all values) from approximately 30 kΩ to 400 kΩ (Figure 4.4A), showing a high dependence on the electroplating parameters. The impedances were highest (mean values around 300 kΩ) due to the use of a current density of 0.1 kA/m^2. About 50% of this electrode impedance could be achieved with 0.3 kA/m^2 and 0.4 kA/m^2 for the selected plating times. In addition, the results for the two highest current densities showed no significant difference (mean values between 130 kΩ and 180 kΩ). With a current density of 0.2 kA/m^2, the lowest impedance with a mean value of approximately 40 kΩ could be achieved. The impedance magnitude decreased gradually with increasing electroplating time until a plating time of 75 s was reached. Thereafter, an increase in the impedance magnitude was visible, indicating that the highest surface roughness had already been achieved. With a plating time of 90 s the value of the impedance was in the same range as with a plating time of 60 s. Compared to the gold electrodes, the impedance reduction was always over 90% (Figure 4.4B). In the best case, the impedance was reduced to a value of around 1% from the original value.

With the electroplating processes, cathodic charge storage capacities in the range of approx. 1,500 µC /cm^2 to 10,000 µC/cm^2 could be achieved (Figure 4.4C). The trend of all measurements was in line with the electrode impedance magnitude, showing the best result at a current density of 0.2 kA/m^2 and an electroplating time of 75 s. The lowest CSC_C were achieved with a current density of 0.1 kA/m^2. The CSC_C for 0.3 kA/m^2 and 0.4 kA/m^2 were in between and showed a low dependence on the plating time.

The open circuit potential (OCP) measured against an Ag/AgCl reference electrode was measured after a waiting time of 300 s following the cyclic voltammetry. The mean values were almost in the range of 0.41 V to 0.48 V with a variation of approximately 50 mV within one electroplating condition (Figure 4.4D). Only the OCP values of the

third process (0.2 kA/m^2, 30 s) were around 0.1 V. This large difference indicated incomplete coating of the electrode sites with platinum.

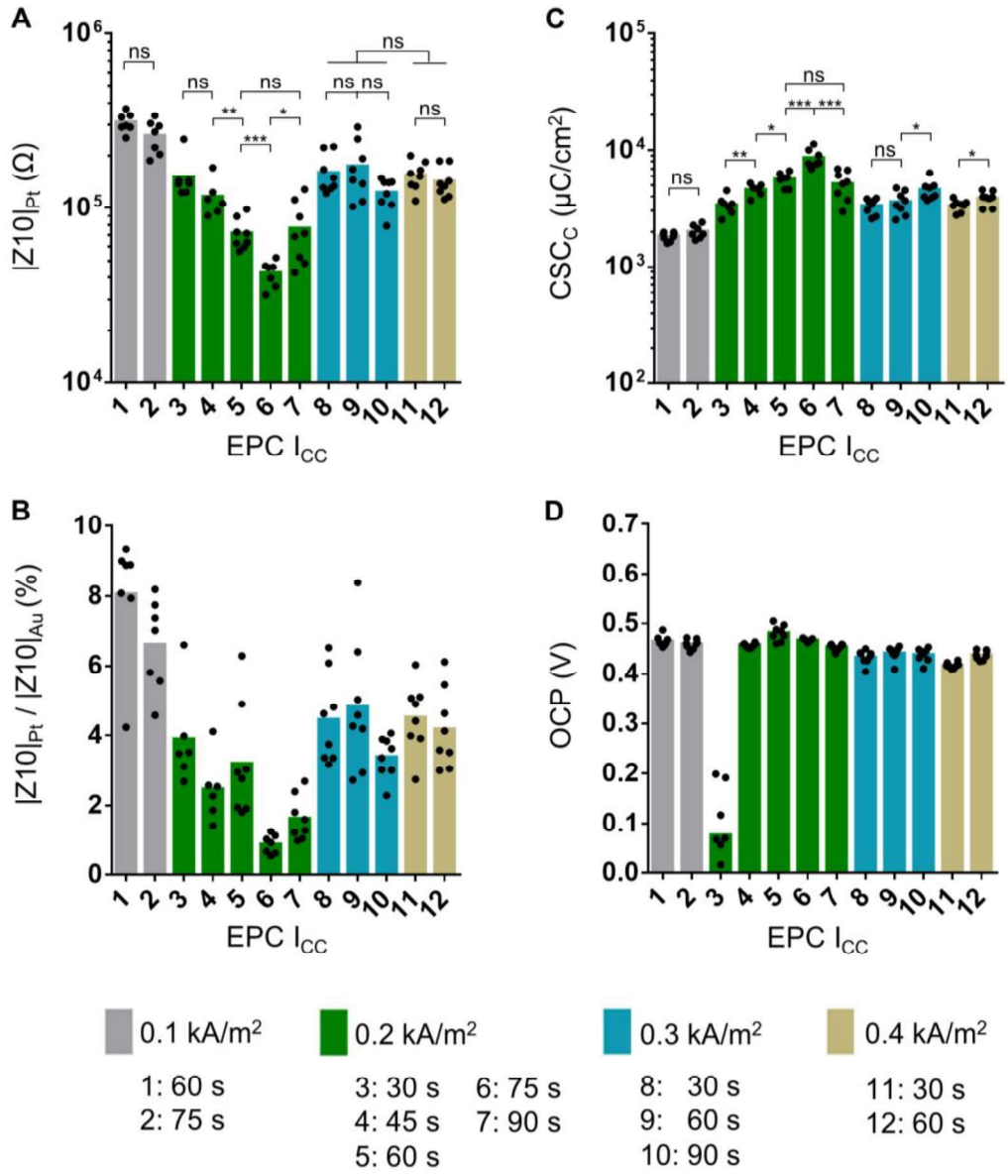

Figure 4.4: Electroplating with constant current (I_{CC}) for round-shaped electrodes. The best results (lowest magnitude of impedance and highest cathodic charge storage capacity (CSC_C)) were achieved for a current density of 0.2 kA/m^2 and an electroplating time of 75 s (EPC I_{CC}6). A) Impedance magnitudes at f = 10Hz (|Z10|). B) Relative change in impedance magnitudes compared to the gold electrodes at f = 10 Hz. C) CSC_C of platinized electrodes. D) Open circuit potentials (OCP) after 300 s in saline against an Ag/AgCl-reference electrode. (Statistical analysis: two-tailed t-test; * p < 0.05; ** p < 0.01; *** p < 0.001, ****p < 0.0001)

4.2.3 Pulsed current electroplating generates similar results for round-shaped and rectangular-shaped electrodes

Round-shaped electrodes

The round-shaped electrode contacts were electroplated with pulsed currents of three different current densities ranging from 0.2 kA/m^2 to 0.4 kA/m^2 (see Chapter 3.2.3). 60 pulses, 90 pulses, or 120 pulses were applied. In addition, the results of different ultrasound (US) power settings (50% or 100%) were tested for the current densities of 0.3 kA/m^2 and 0.4 kA/m^2.

The magnitude of the impedances of the electrode impedance at the frequency of 10 Hz were lower than 100 kΩ for all pulsed current electroplating processes (Figure 4.5A). Compared to the impedance magnitudes of the gold electrode, these values were approximately in the range of 1% to 4% from the original measurements (Figure 4.5B). Across the different electroplating current densities, the electroplating processes with 0.2 kA/m^2 resulted in the same impedance range than the electroplating processes with 0.4 kA/m^2. The impedance magnitudes generated with a plating current of 0.3 kA/m^2 were approximately 20% lower than in the other conditions. The number of applied pulses had only an effect at the electrodes' impedance, when low currents or small number of electroplating pulses were used. With one exception (electroplating condition 3 to 4), no significant difference between the settings of 50% or 100% US power. Both indicated that a certain amount of electrical charges was needed to decrease the variability in the impedance of the electrodes. Compared to the electroplating with constant currents, the impedances after both electroplating methods were in the best cases very similar.

In line with the results of the impedance magnitudes, the achieved CSC_C were best for the electroplating with a current density of 0.3 kA/m^2 ranging from 9,200 µC/cm^2 to 12,700 µC/cm^2 (Figure 4.5C). Thereby, the CSC_C was also in the same range as in the best case with constant current. As with the impedance, there was no indication that the ultrasound power had a directed impact on the result. Over all electroplating conditions, there were no significances, once an improvement at 100 % (condition 4 to 7), and once at 50 % (condition 9 to 11) US power visible. The OCP mean values were within 0.42 V to 0.49 V (Figure 4.5D). With the exception of PC5 (138 mV) and PC11 (244 mV), the OCPs of the electrodes were within a range of 100 mV. This range was

almost twice as high as the values from the electroplating with constant current. The low OCPs in PC11 indicated that the electrode sites could have defects in the coatings.

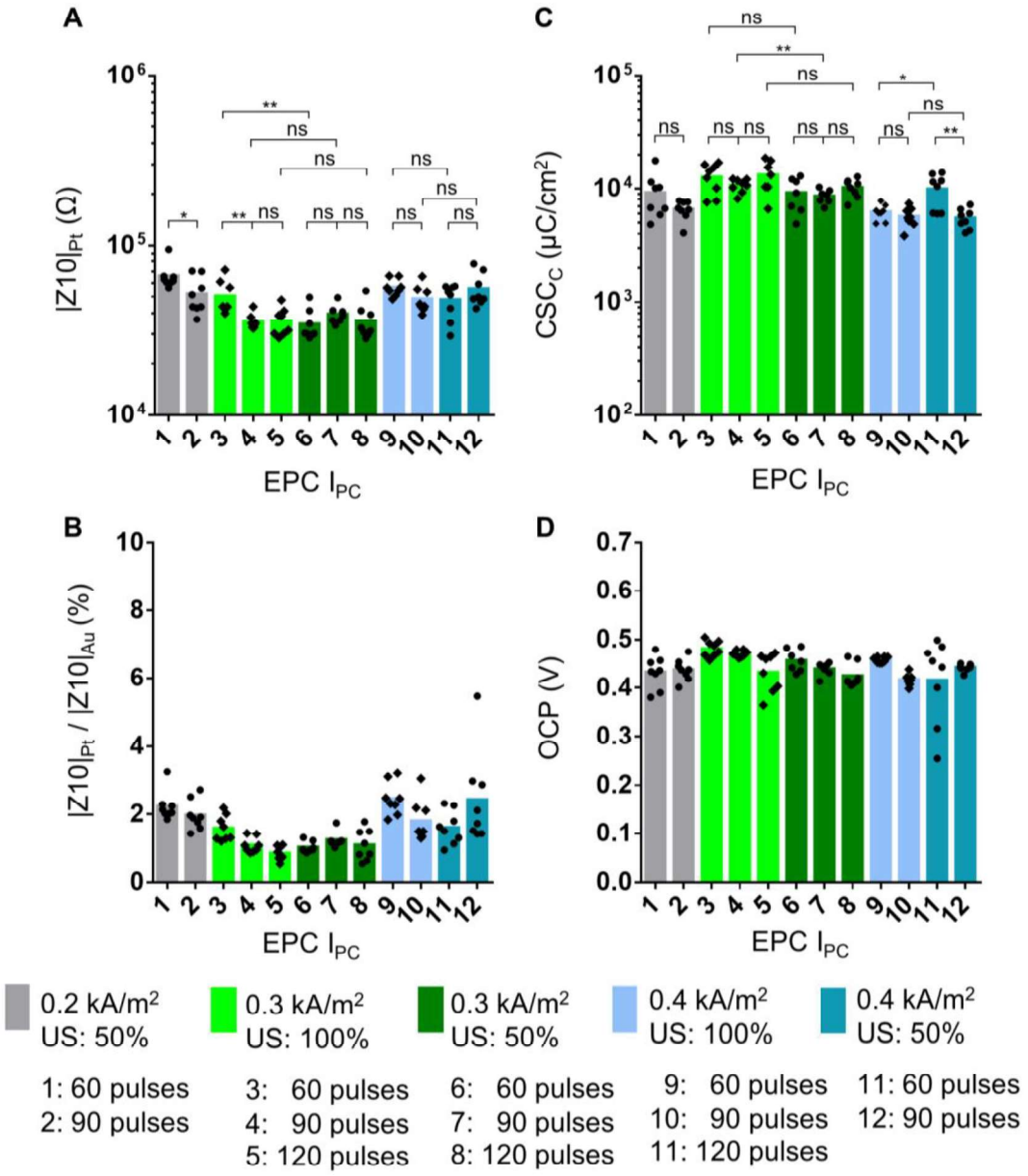

Figure 4.5: Electroplating with pulsed current for round-shaped electrodes. The best results (lowest magnitude of impedance and highest cathodic charge storage capacity (CSC_C)) were found for current densities of 0.3 kA/m^2. A) Impedance magnitudes at f = 10Hz (|Z10|). B) Relative change in impedance magnitudes compared to the gold electrodes at f = 10 Hz. C) CSC_C of platinized electrodes. D) Open circuit potentials (OCP) after 300 s in saline against an Ag/AgCl-reference electrode. (Statistical analysis: two-tailed t-test; * p < 0.05; ** p < 0.01; *** p < 0.001, ****p < 0.0001)

Rectangular-shaped electrodes

The rectangular-shaped electrodes were coated with platinum driven by pulsed currents. Current densities of 0.2 kA/m^2, 0.3 kA/m^2, and 0.4 kA/m^2 and ultrasound in 50% power setting were applied. For each current density, 60 pulses, 90 pulses, or 120 pulses were used.

The measured impedance magnitudes at 10 Hz were in the range from 6 kΩ to 28 kΩ (Figure 4.6A). The best results were achieved at 0.2 kA/m^2 with 120 pulses and 0.3 kA/m^2 with 90 pulses (Figure 4.6A, B). The electrodes' impedances were very poor using current densities of 0.4 kA/m^2. The reduced impedances were within 1-5% compared to the impedance of the gold sites (Figure 4.6B). Taking the geometric surface area into consideration, an 'area impedance' could be calculated by impedance magnitude multiplied with geometric surface area. Based on all measurements, for the rectangular electrodes, values of 0.48 kΩmm^2 (6 kΩ) to 2.24 kΩmm^2 (20 kΩ), and for the round-shaped electrodes coated with pulsed currents values of 0.54 kΩmm^2 (30 kΩ) to 1.8 kΩmm^2 (100 kΩ) were estimated. With a current density of 0.3 kA/m^2 and 90 current pulses the values were 0.54 kΩmm^2 to 0.9 kΩmm^2 for the round-shaped electrodes and 0.48 kΩmm^2 to 0.68 kAmm^2 for the rectangular-shaped electrodes. This indicated that the electroplating process produced comparable surface porosities for both types of electrodes.

The CSC_C were highest for 0.3 kA/m^2 and 60 pulses with values around 12.000 µC/mm^2 (Figure 4.6C). Considering the higher variation of the CSC_C of the round-shaped electrodes, the values of the rectangular-shaped electrodes were also similar to the previous one. The mean OCP ranged from 0.39 V to 0.49 V (Figure 4.6D) and was mostly within a range of 100 mV. This was also in line with the measurements of the round-shaped electrodes.

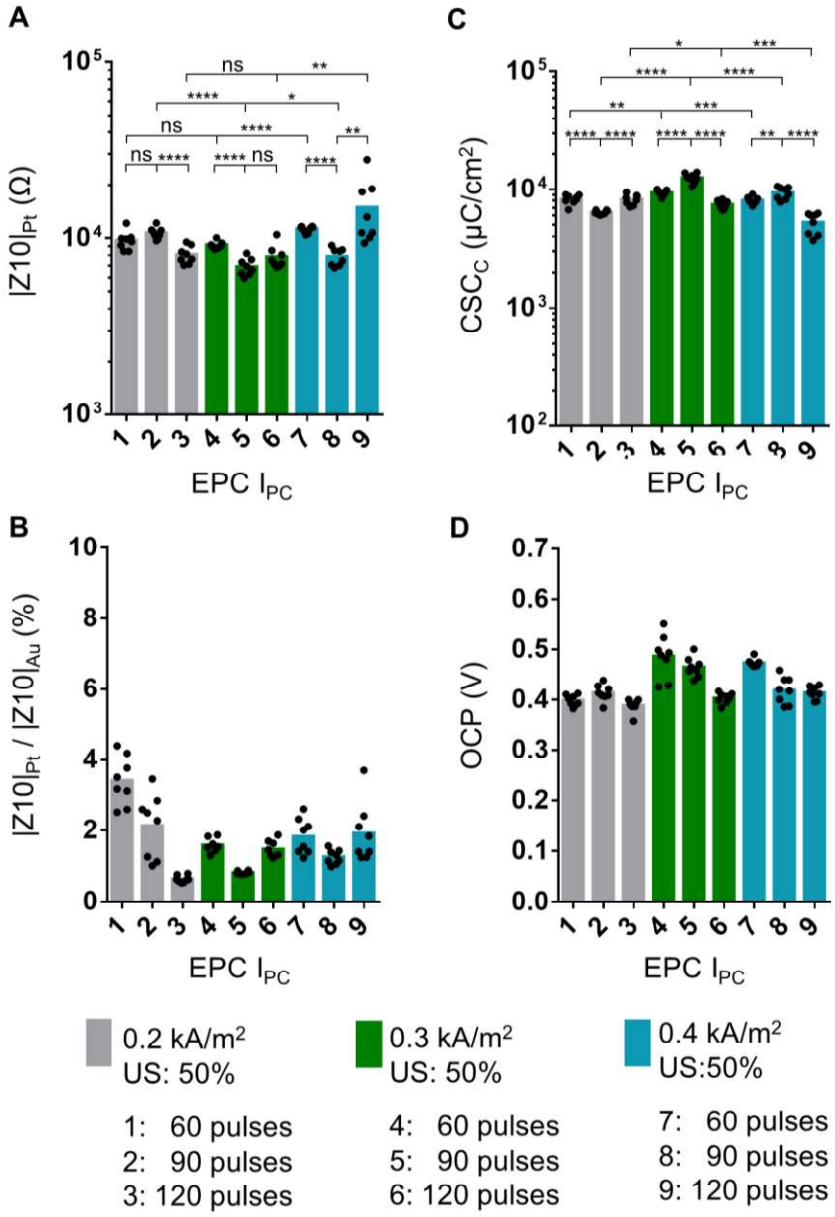

Figure 4.6: Electroplating with pulsed current for rectangular-shaped electrodes. The results were similar compared to the round-shaped electrodes electroplated with pulsed currents. A) Impedance magnitudes at f = 10Hz (|Z10|). B) Relative change in impedance magnitudes compared to the gold electrodes. C) Cathodic Charge Storage Capacities (CSC_C) of platinized electrodes. D) Measured open circuit potentials after 300 s in saline against an Ag/AgCl-reference electrode. (Statistical analysis: two-tailed t-test; * $p < 0.05$; ** $p < 0.01$; *** $p < 0.001$, ****$p < 0.0001$)

4.2.4 Electrode model parameters reflect the increase in surface porosity

The extraction of the model parameters (for constant phase element (CPE), solution resistor (R_S), diffusion resistor (R_F); Chapter 1.4.3) was done for all measurements of platinum electrodes. Due to the size of the electrode sites and the measurement frequency range, R_F could not be reliably determined (values from 1 MΩ to 1 TΩ). For analysis of the model parameters, R_S and the angle factor (α) of the CPE were set in relation to the admittance value (Y_0) of the CPE (Figure 4.7).

R_S for the round-shaped electrodes after both electroplating methods was in the range of 2 kΩ ± 300 Ω. This indicated a measurement variance due to room temperature change as well as some manufacturing tolerances of the electrode sites (Figure 4.7A, C). For the rectangular-shaped electrodes, R_S was within 0.95 kΩ ± 100 Ω (Figure 4.7E), which was approximately the half of the round-shaped electrode value due to the larger electrode. Over all measures, no relation between R_S and Y_0 was visible indicating that the geometric areas were not differently affected by the electroplating process (Figure 4.7A, C and E). However, the impedance variations from the previous chapters were also visible in the value distribution of Y_0. The angle factor α ranged from 0.85 to 0.94 over all electroplating processes and had no dependence on Y_0 (Figure 4.7B, D and F).

In the results of the pulsed current plating process, some higher derivations were visible. For these points, there were also higher Y_0 and lower R_S values. For the electroplating processes I_{PC} 5 and I_{PC} 11 (strongest derivation) also, the OCP had a high variability compared to the other processes, indicating inhomogeneous coatings. Y_0 of the rectangular electrodes was within 1.5 Ss^{α} to 4 Ss^{α} (Figure 4.7E) and therewith four times higher than Y_0 of the round-shaped electrodes with the same electroplating process. This matched the ratio of geometric surface areas and demonstrated the reliability of the electroplating process. The angle factor α (Figure 4.7F) was also in the same range as for the other plating processes with the highest variation for the highest current strength.

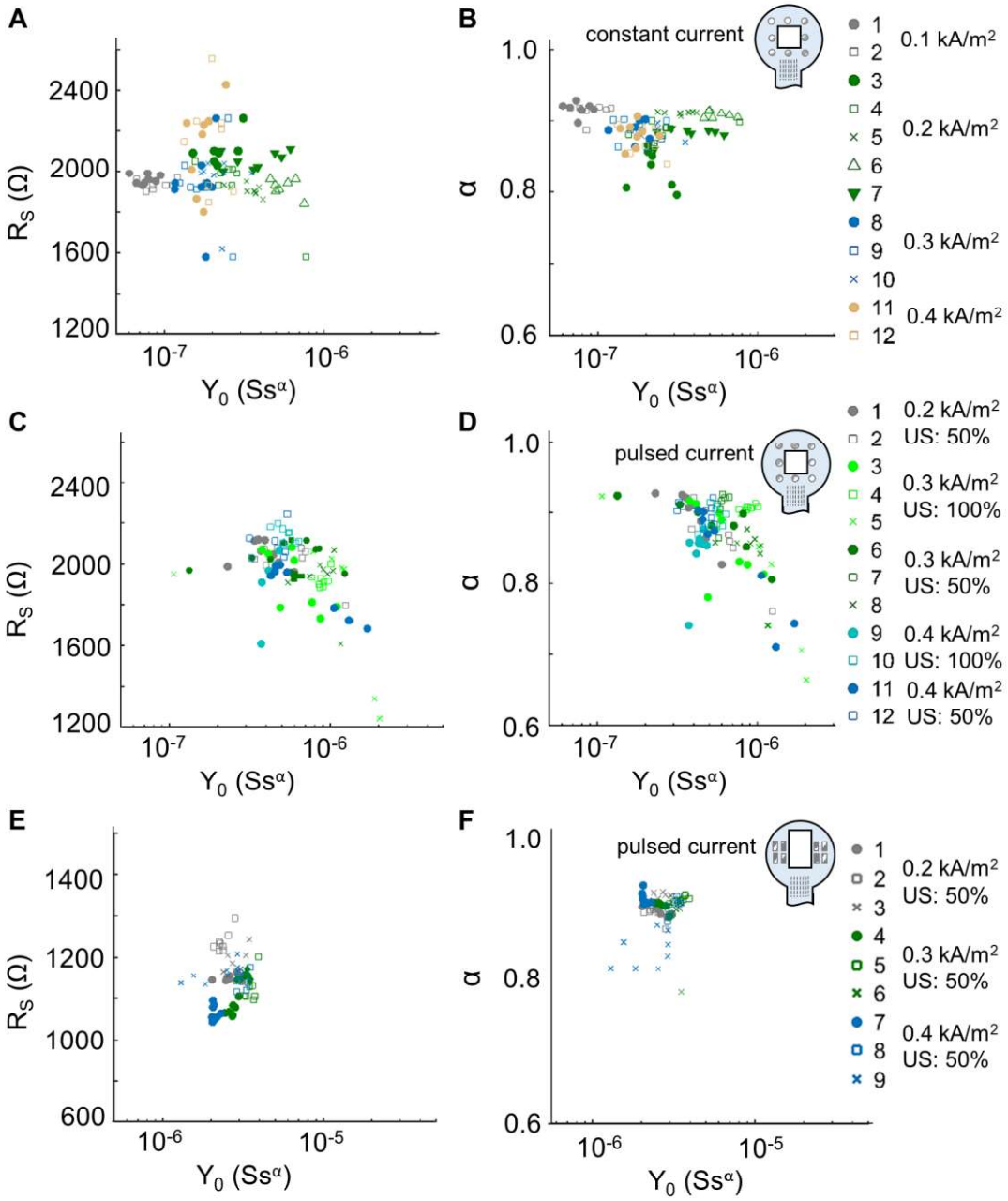

Figure 4.7: Electrode model parameters of the platinized electrodes. A, B) Solution resistor (R_S) and angle factor (α) of constant phase element (CPE) for electroplating with constant current of the round-shaped electrodes. C, D) R_S and α for electroplating with pulsed current of the round-shaped electrodes. E, F) R_S and α for electroplating with pulsed current of the rectangular-shaped electrodes

4.3 Electrode design supports an fast and reliable application in standard surgeries

4.3.1 Electrodes applied during craniotomy

Electrodes could be placed on the dura during a standard craniotomy, which was adapted from Cupido and colleagues (Cupido et al., 2014). Using a scalpel, scissors, and a forceps, the skin and hairs at the head were removed (Figure 4.8A). A driller (GG 12, PROXXON) and a drill bit with a diameter of 0.9 mm (FST 19008-09, Fine Science Tools) were used to make a small hole in the bone over the somatosensory cortex of the left hemisphere or the cerebellum. A short platinum wire (Ø350 µm, TM11S0351N, CONATEX) acting as ground and reference electrode was placed into the hole and fixed with dental cement (RelyX®, 3M ESPE) on the skull. With a second drilling, the craniotomy was made over the somatosensory cortex (lateral = 1.5 mm and longitudinal = 2 mm from the bregma) of the right hemisphere with diameters between 3 mm and 5 mm. During the drilling processes, a cortex buffer was used to clean the scull and to keep the bone slightly wet.

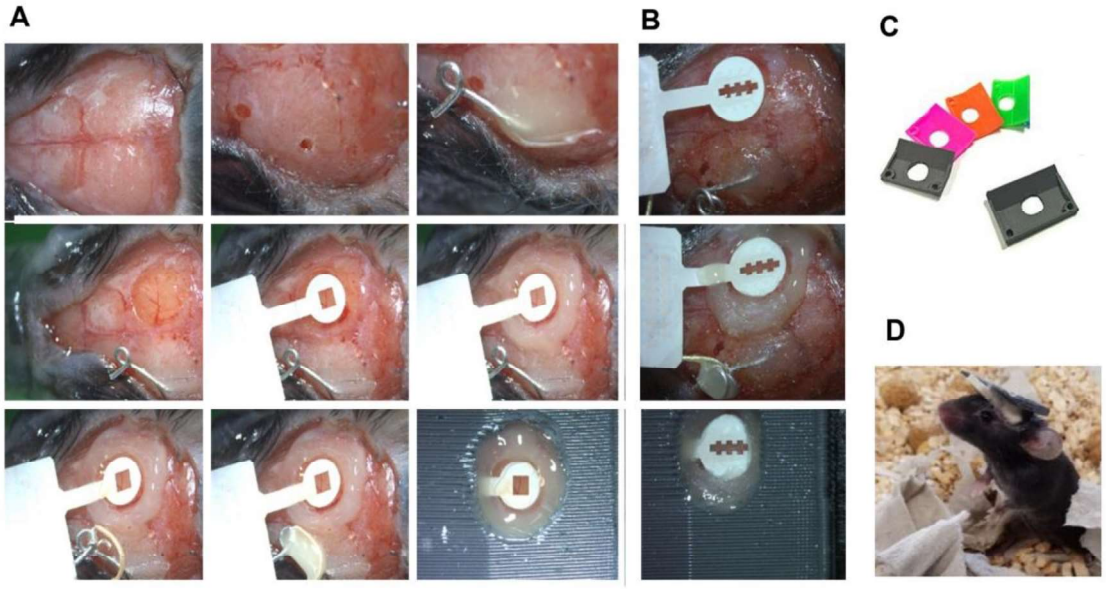

Figure 4.8: Electrode application during a craniotomy. A) Stepwise implantation of an electrode array with eight round-shaped electrode sites and one platinum wire. B) The sixteen-channel electrode was applied in the same way as the eight-channel electrode. C) 3D-printed head holder to cover the surgery site, to secure the electrode connector and to fasten the mouse under the 2P-LSM. D) Mouse after surgery and first recovery of approximately one hour.

After removing the bone, the sterilized (70% Ethanol) and cleaned (cortex buffer) electrode array was placed. A round-shaped coverslip was put on the electrode head and fixed to the bone with dental cement. The wire from the electrode was tightly wrapped around the platinum wire and also fixed with dental cement. A custom-made 3D-printed head holder (Figure 4.8B, technical drawing in Appendix Chapter 8.7) was glued (dental cement) on top. The mouse became used to the electrode and head-holder within approximately 1h after surgery and had no difficulty wearing the system. The weights of a head-holder and of an electrode were 0.66 g or 0.08 g, respectively.

4.3.2 Electrodes applied during a laminectomy

After the first successful implantation of the surface electrodes onto the cortex, two electrodes with three electrode sites were designed for the spine application (Figure 4.9). The assembling process was the same as for the cortex electrodes (soldering connector, fixation with epoxy resin, and electroplating). A standard 3-pin connector with 1 mm pitch was used, and the size of the electrodes' sites was 400 µm x 200 µm.

The electrodes were applied during a modified laminectomy process (Fenrich et al. 2012) directly on the dorsal surface of the lumbar spinal cord after resection of the dorsal laminae of the vertebrae T13 and L1 to expose the lumbar spinal segments L1 and L2 for chronic 2P-LSM imaging. Therefore, the animals` spinal column was fixed with modified paper clips and clamps to stabilize the spinal cord and to lift up the body while imaging sessions to prevent breathing artefacts. After removal of the laminae and cleaning the meninges from debris with ACSF, a separate platinum (Ø350 µm, TM11S0351N, CONATEX) wire was put into the surgery site and a thin sheet of cured silicone (approximately 0.5 mm, Fresh® clear, Dreve Dentamid GmbH) was placed on the electrodes. An additional thin layer of liquid silicone was put on the first silicone layer. After that, a cover slip was placed on the silicone and fixed with dental cement. The catwalk and connector pad were glued to the skin. The mirrored electrodes enabled the connection of the stimulation and recording system. The platinum wire was used as ground electrode.

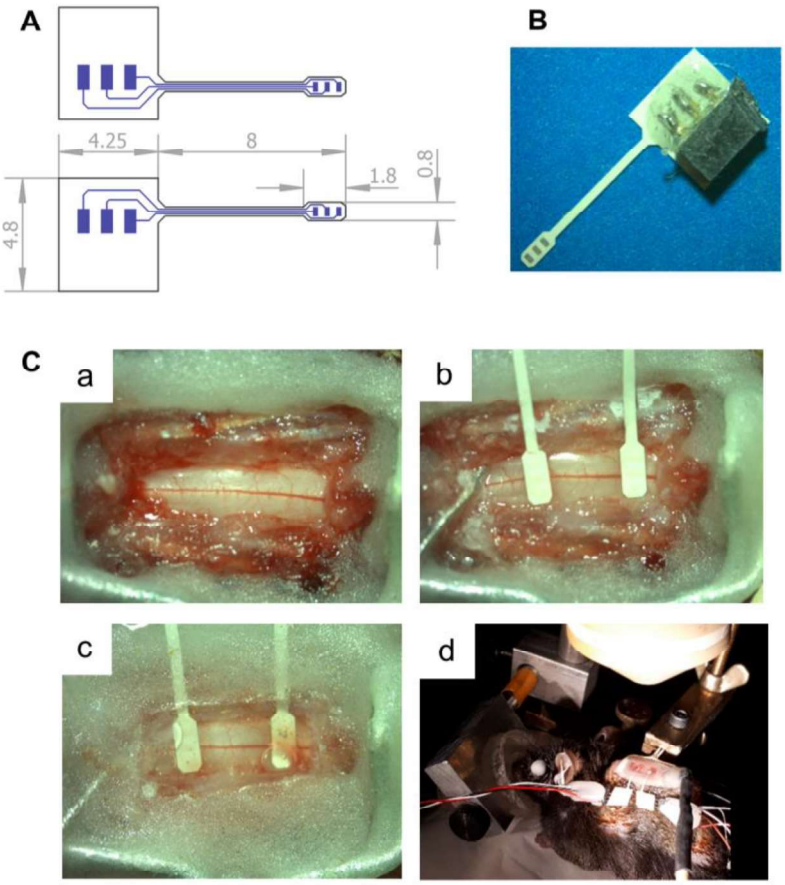

Figure 4.9: Spinal surface electrodes. A) Electrode design of two mirrored arrays with three electrode sites. B) Assembled and platinized electrode. C) Overview of the surgery procedure (a-c). a) Surgery site after removal of the vertebras and artificial stabilization. b) Surgery site with applied electrodes and ground wire. c) Surgery site after application of silicone, cover slip, and fixation with dental cement. d) Mouse under the 2P-LSM with connected electrodes for stimulation and recording.

4.4 Electrode arrays do not cause inflammation at cellular level

The cellular reaction after craniotomy and electrode application was investigated in short-term (three days after electrode application (3 pdE) and long-term (28 dpE) conditions. For this, four different immunostainings were used in brain slices to visualize the cell nuclei (DAPI), GCaMP3 in astrocytes, GFAP in astrocytes and microclia. The checkerboard pattern in the GFAP-based image (Figure 4.10) indicated that the signal gain of the image acquisition device was at the upper limit. Hence, only few reactive

astrocytes were visible in the entire brain slices and especially in the cortex. In addition, the following details could be obtained from the various images.

- No difference in signal intensity of the DAPI signal on both hemispheres for the short-term and long-term conditions, indicating that no cell death occurred after electrode implantation.
- No impact to the Ca^{2+} indicator GCaMP3 (GFP staining) in astrocytes by the electrode or its application.
- On the ipsilateral hemisphere, a small increase in the number of reactive astrocytes (GFAP staining) could be observed after three and 28 days following the electrode surgery. Considering the high signal amplification, however, only a small immune response was visible.
- Compared to the contralateral hemisphere, after three days, a very weak tendency towards higher microglia activity was observed, which was no longer visible after 28 days after the electrode application. Thus, the result showed no continuous inflammation caused by the LCP surface electrode. This also suggests that the small increase of reactive astrocytes could be due to the craniotomy.

Overall, the comparison of the two cortical hemispheres showed that the surface LCP electrodes including the application method were biocompatible.

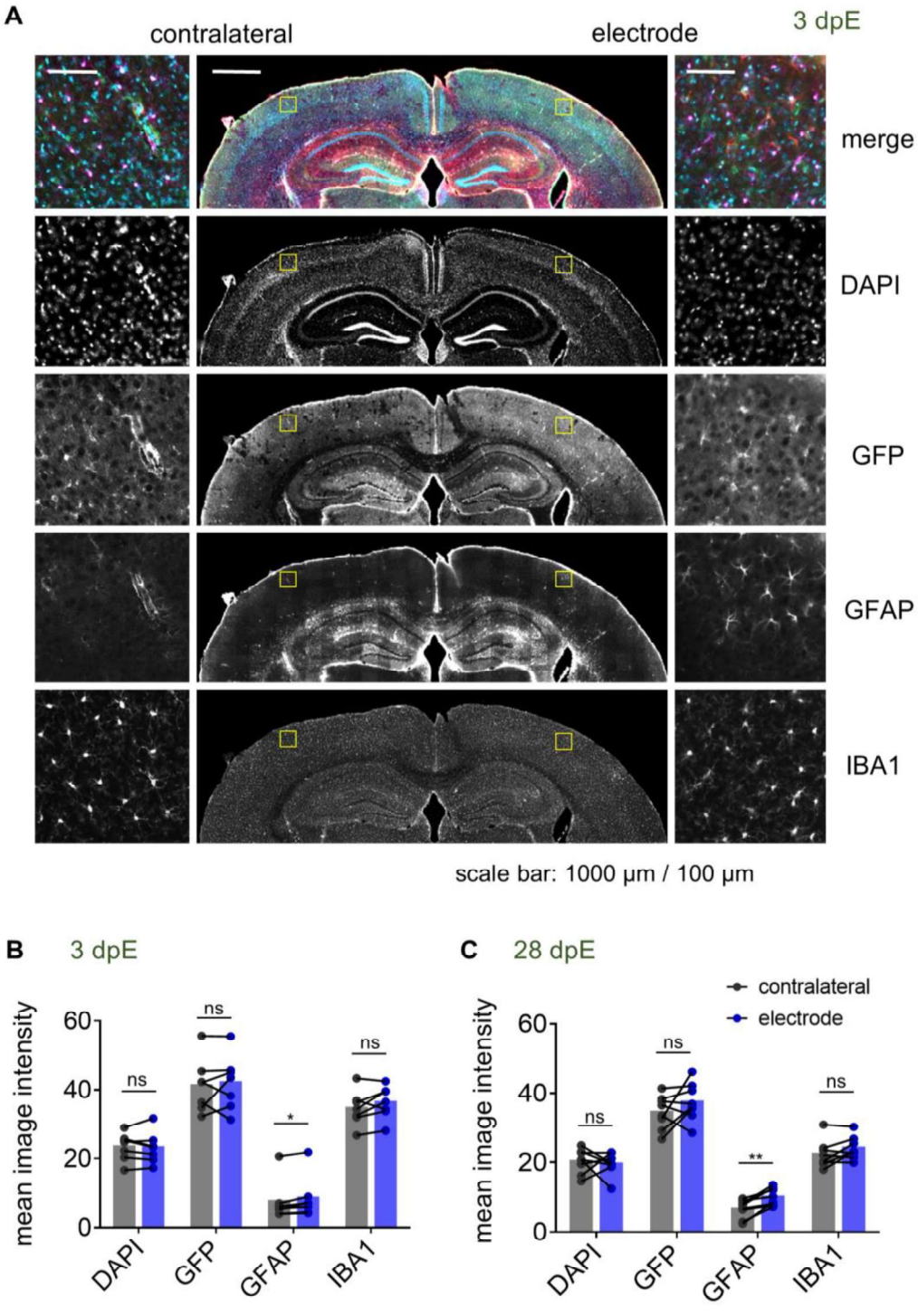

Figure 4.10: Cellular reaction to surface electrode. A) Example of the different stainings for one brain slice at 3 dpE (DAPI: cell nuclei; GFP: Ca^{2+} indicator GCaMP3 in astrocytes; GFAP: reactive astrocytes; IBA1: microglia. B, C) Comparison of mean image intensity for the short-term condition (3 dpE) and the long-term condition (28 dpE). (Statistical analysis: Wilcoxon matched-pairs signed-ranks test; * $p < 0.05$; ** $p < 0.01$; *** $p < 0.001$, ****$p < 0.0001$)

4.5 Craniotomies with electrodes are stable over long-term implantation periods

The electrodes were placed on the dura after a craniotomy, meaning that part of the skull had to be removed. This implies that with the surgery a repair process would be triggered having a potential impact on 2P-LSM and electrophysiology. For this reason, the tissue response was visually investigated.

4.5.1 Bone regrowth limits visual access to the cortical tissue

Bone regrowth was observed with a bright field microscope, and a CCD camera was used to take images from the craniotomies. The optical window became more and more blurred after the surgery (Figure 4.11A, B). This was due to the regeneration of the bone which started with angiogenesis and the generation of a thin tissue layer. The tissue layer (Figure 4.11C) started growing under the electrode. With time, the bone grew inside the complete craniotomy and the electrode grew in (Figure 4.11B).

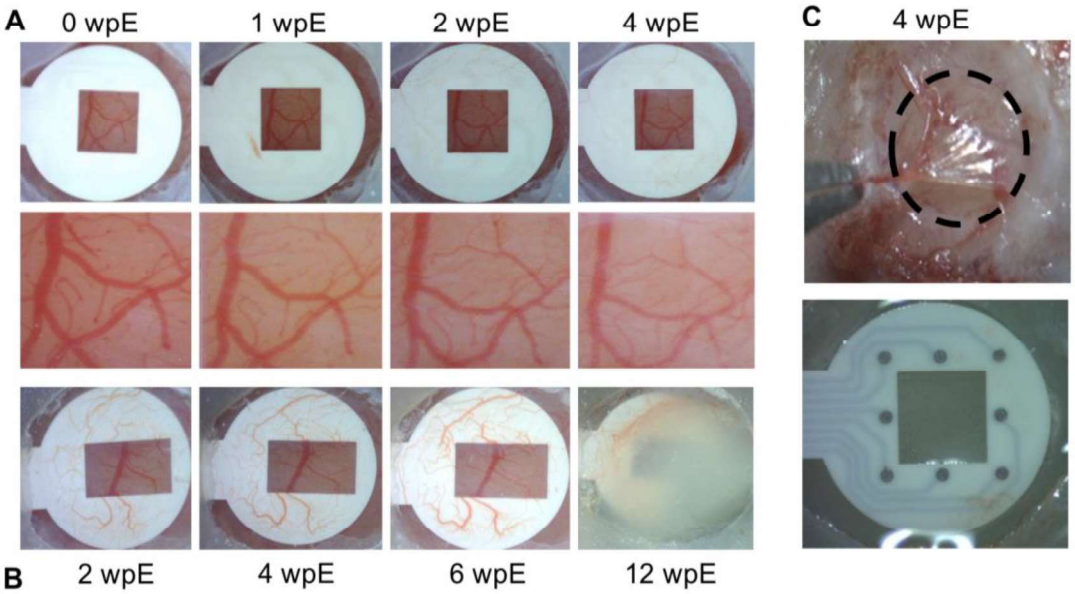

Figure 4.11: Transparency of the craniotomy. A) Top: Images of an eight-channel electrode after surgery with low angiogenesis level. Bottom: Cortical tissue within the electrode window. The bone regrowth was visible from week four. B) Images from an eight-channel rectangular-shaped electrode with a strong angiogenesis on the surface. At week 12, the electrode array was almost completely overgrown. C) Thin tissue layer under the electrode after four weeks (black circle indicates the position of the craniotomy) and explanted electrode without any defects.

With a thin bone layer, 2P-LSM was still possible (Yang et al., 2010), but the image quality became worse and a higher laser power was needed. The angiogenesis could be easily observed on the surface of the electrode. After explantation, the electrodes were visually checked for defects (e.g. removal of platinum coating), but no defects were visible.

4.5.2 Dexamethasone has no influence on angiogenesis

Angiogenesis is generally a positive sign of healing effects and, in case of implants, it indicates that the implanted materials are well accepted (Laschke et al., 2006). However, as an indicator for tissue and bone regrowth, it was also associated with the limitation of the optical access of the cortical tissue. Three different dexamethasone injection protocols were used to investigate whether dexamethasone might be a good candidate for reducing the growth rate of blood vessels. Therefore, the area of the electrode head surface covered by vessels was automatically estimated (Figure 4.12). The results showed a very fast growth within the first two weeks after the surgeries, which continued with an ongoing reformation of the vessels. The vessels covered a maximum of approximately 12% of area of the LCP electrode head (6.1 mm^2). For a better comparison, the data points were evaluated on a weekly basis. If there was no data point available for a mouse, a linear interpolation from the previous and subsequent data point was used. The resulting diagram showed no effect on angiogenesis related to the dexamethasone protocol. This could be confirmed with the subjective visual inspection. It was more likely that small bleedings that occur during surgery will have a major impact on angiogenesis in the first two weeks.

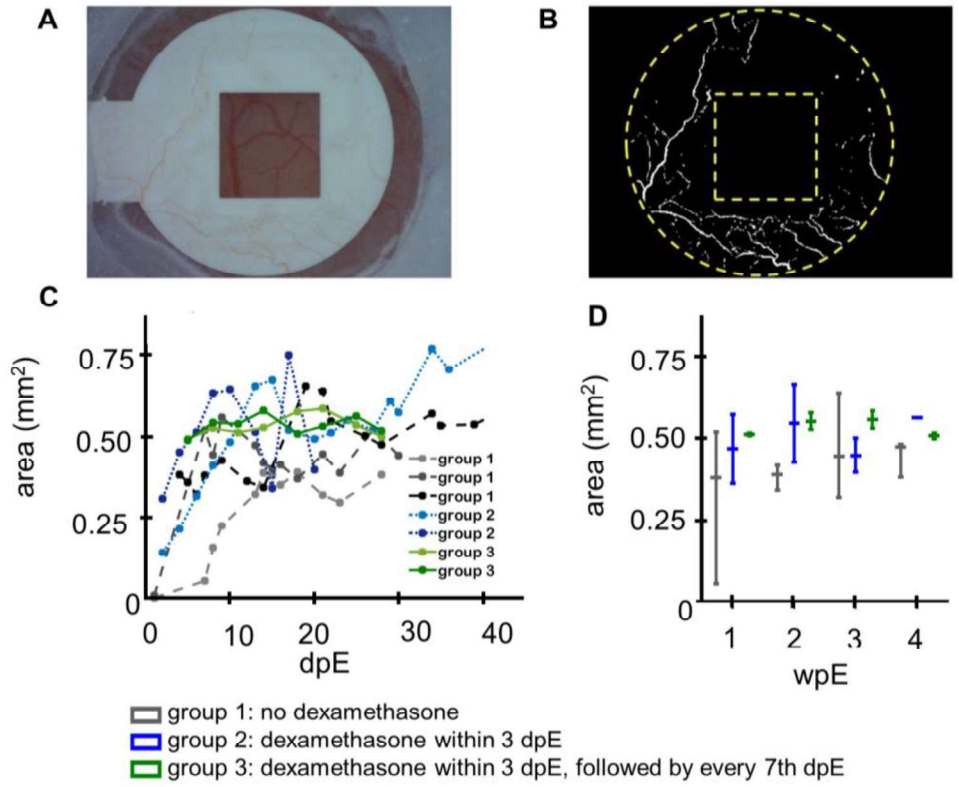

Figure 4.12: Angiogenesis on the electrode arrays for different dexamethasone injection protocols. A) Example of an electrode surface partly covered with blood vessels. B) Result of the vessel detection for the example of A). C) Time traces of coverage by the vessels for the single mice within the dexamethasone groups. D) Grouped data points at full weeks.

4.6 Electrode arrays can be used for recordings of spontaneous and evoked ECoGs

4.6.1 ECoG of awake and anaesthetized mice

The sixteen-channel electrodes were used in recording studies to test the recording quality and to gain knowledge about the spatial distribution of signal events. The depth of anaesthesia was changed (isoflurane from 1.5% to 0%) to vary the pattern of the bioelectrical activity. The recordings showed a typical synchronous burst activation of neurons when the mice were anaesthetized (Figure 4.13A). With decreasing anaesthesia, the mice woke up and the time between the bursts became shorter and the signal amplitude lower, indicating a loss of synchrony. When the mouse was

completely awake, the burst pattern was no longer visible. The difference in neuronal activity was also visible in the spectrograms (Figure 4.13B) of the signals. In the anaesthetized mouse, the highest signal intensities were at frequencies below 10 Hz, and frequencies higher than 30 Hz were temporarily visible when the neurons fired synchronously. Since there was no evidence of signal components with a broad frequency range during the burst suppression phases, it could be estimated that there was no detectable noise affecting the signal quality. In the awake state, the highest signal intensity was also below 10 Hz, but the higher frequencies were always present due to the continuous spiking activity.

The individual signal traces show a high similarity as well as some differences between the individual channels (Figure 4.13A). To characterize the channel similarity, the correlation between the recorded signals were calculated. A stepwise calculation (sliding window of 2 s, step time 1 s) demonstrated the dependence of the synchrony along the cortical electrical activity (Figure 4.14A). The channel similarity was lower if there was high spike activity (bursts and neuronal activity in the awake state). In addition, the correlation decreased with channel distance. Correlations were calculated for 30 s traces in relation to the distance of the electrode sites (Figure 4.14B). The distances of the electrode sites were normalized geometric distances (value of 1 means 750 µm, 1.41 means 1057.5 µm, …, 4.24 means 3180 µm). This diagram confirms the results from the stepwise calculation. The correlation coefficient was high for electrode sites nearby and decreased with increasing distance. For awake mice, the results were lower as for mice under anaesthesia. The variation within one electrode distance came from the different signals in the single sections and from the various channel pairs.

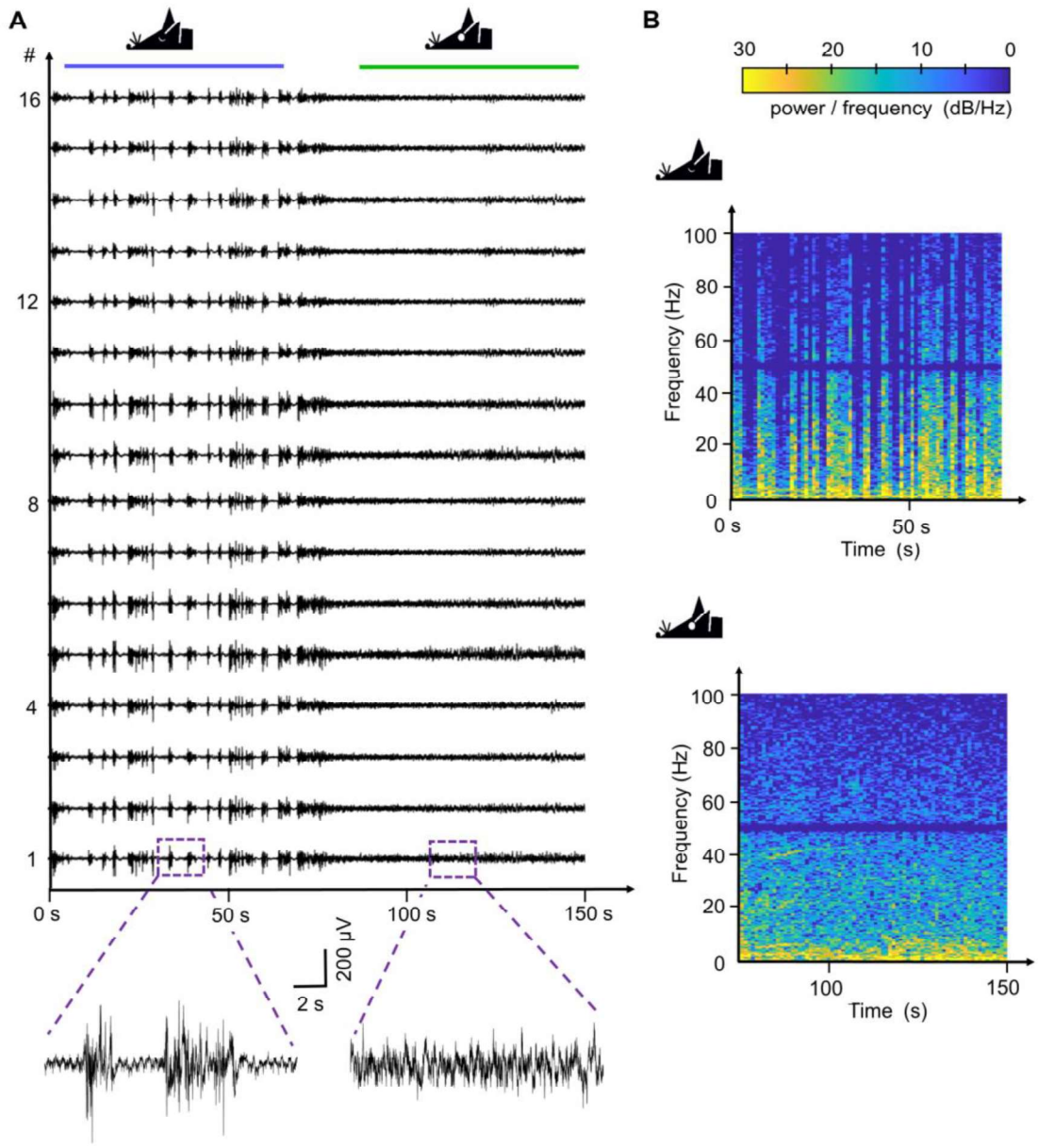

Figure 4.13: ECoG recorded with a 16-channel electrode array at a slightly anaesthetized mouse with decreasing anaesthesia (sampling rate: 1.2 kHz, bandpass filtering: 0.5 Hz – 250 Hz, notch filter: 50 Hz). A) Time traces of all sixteen channels. Subsets from channel one present a single signal trace for anaesthetized (left) and awake (right) mouse. B) Spectrograms of channel two (after short-time Fourier transform with a sliding window of 2 s shifted in steps of 1 s). The horizontal dark lines were caused by the 50 Hz notch filter of the recording device.

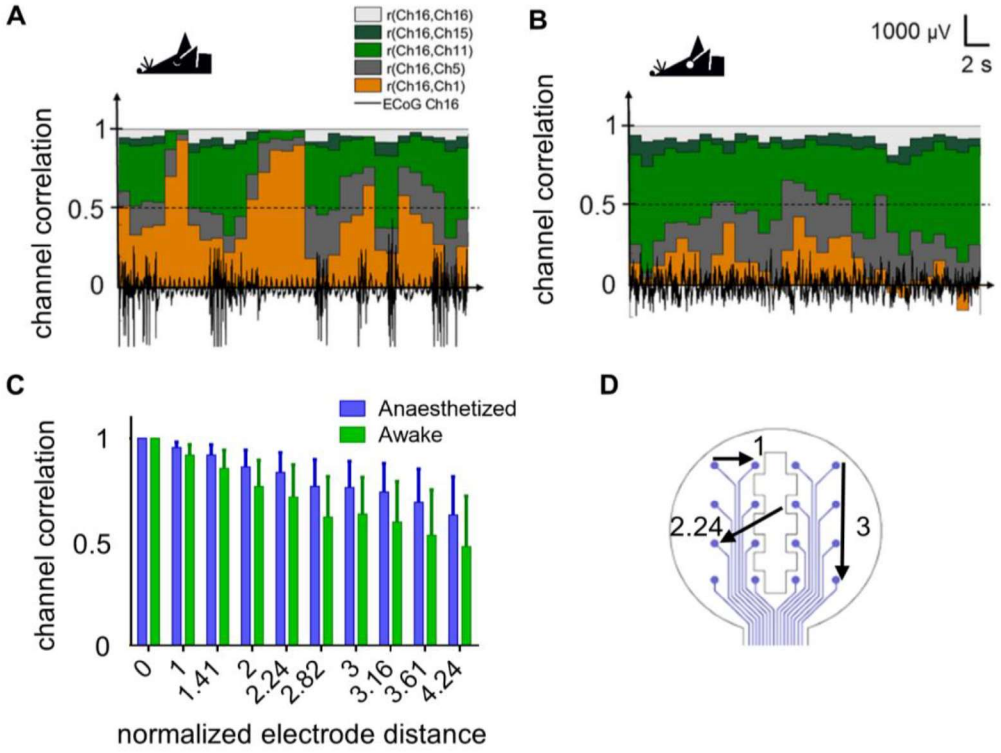

Figure 4.14: Channel correlation shows high similarity of neighboring channels. A, B) Sections of 30 s ECOG signal (sampling rate: 1.2 kHz, bandpass filtering: 0.5 Hz – 250 Hz, notch filter: 50 Hz) and stepwise correlation (window size: 2 s, step time: 1 s) for neighboring channels (channels 16 and 15) and for the channels along the diagonal axis (channels 16 and 11; 16 and 5; 16 and 1). For control, the autocorrelation of channel 16 is also included. A) Anaesthetized mouse. B) Awake mouse. C) Correlation results of 30 s time traces sorted along the normalized geometric electrode distance of all possible channel combinations. (Anesthetized: 23 signal sections of four recordings; awake: 21 signal section of 4 recordings; bars: mean value, whiskers: standard deviation) D) Sixteen channel electrode head with three examples of normalized distances.

4.6.2 Demyelination process induced by cuprizone is visible in visually evoked potentials

To prove the hypothesis that cuprizone-induced demyelination should be visible in visually evoked potentials (VEP), a series (128 pulses) of short green flashes (50 ms) was applied to the left eye of the mouse. The mice were placed into a dimmed Faradaic cage. The VEP was recorded at different time points after the electrode surgery and appeared slightly different for each mouse and recording session (Figure 4.15, Appendix Chapter 8.6). The quality of the recording was always high and the VEP could

be clearly identified. The VEPs were analysed by identifying the maximum value that appeared approximately 75 ms from stimulation onset and by the calculation of the signal energy.

All values were set in relation to the values on the 14th day after the electrode surgery to minimize the influence of the differences between individual mice. Nevertheless, the results showed a high variation between the single recordings. But in contrast to normally fed mice, the signal energy (Chapter 3.6.3) of cuprizone-fed mice decreased continuously over time. No clear tendency was visible for the peak value of VEP. The frequency analysis showed that the delta, theta, and alpha bands were prominent about the complete observation period for both groups of mice. The decrease in the signal energy was related to these bands for the cuprizone-fed mice.

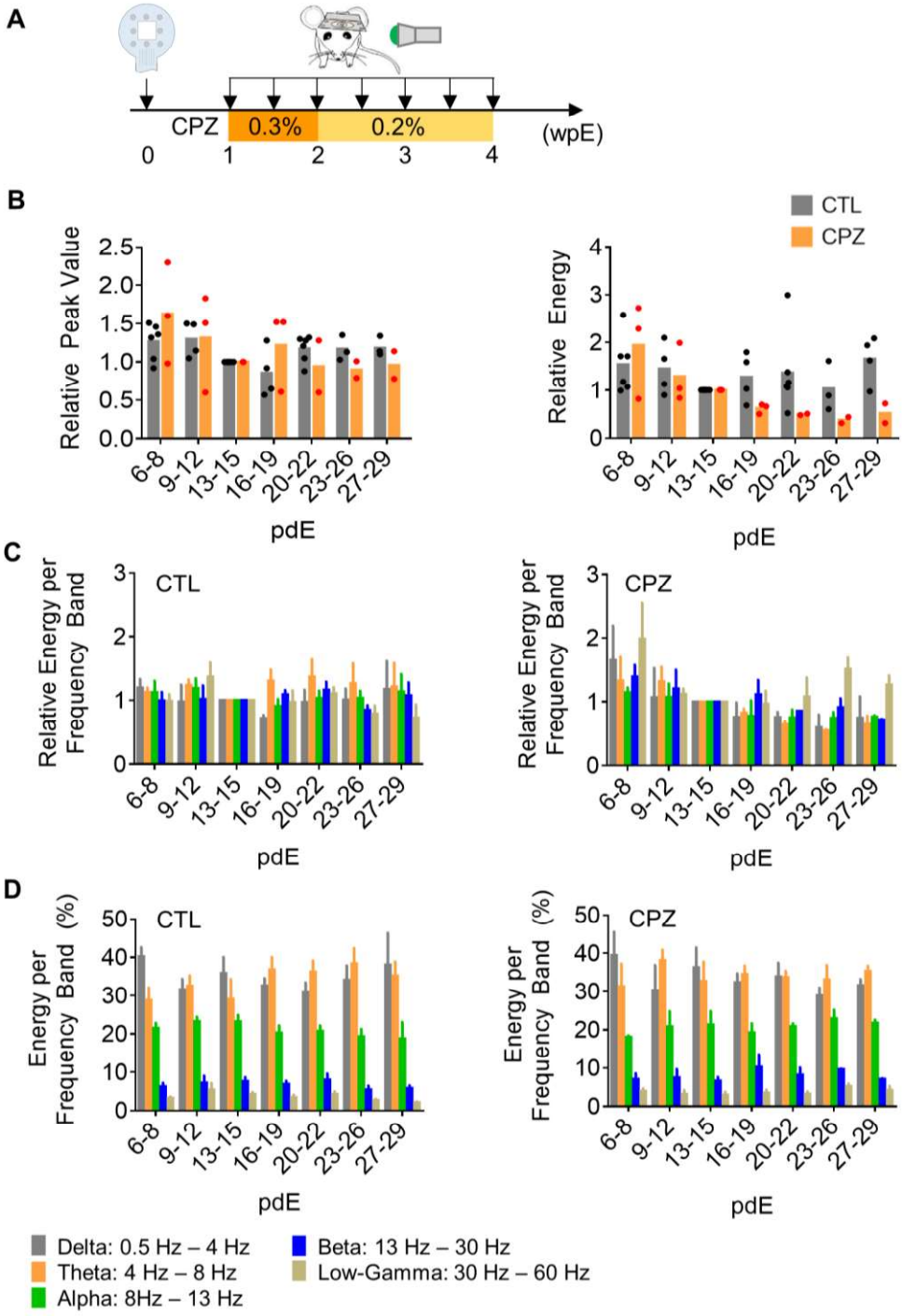

Figure 4.15: VEP analysis of normal-fed mice and cuprizone-fed mice. A) Study set-up. Awake GLAST-CreERT2 x R26-CAG-lsl-GCaMP3 mice (three CPZ-feed and six normal-fed mice) with applied eight-channel electrode were used for VEP recording (sampling rate: 1.2 kHz). Mice were positioned in dimmed environment and green light flashes (50 ms) were applied. Measured data points were grouped together into half weeks. B) Comparison of the peak value (left) and of the signal energy (right) for the two different groups. The values are normalized to day 14. C) Normalized signal energies in the different frequency bands for the normal-fed mice (left) and cuprizone-fed mice (right). D) Distribution of the signal energy within the frequency bands.

4.7 Electrodes can be used as a local coordinate system

The white surface of the LCP electrodes was visible in the two-photon images due to the reflection of the IR laser beam and non-ideal optical filtering to separate the different light wavelength. This offered the possibility to determine the position of the field of view in relation to a corner of the observation window (Figure 4.16). In addition, three corners of the observation window could be used to generate a local coordinate system and thus calculate the orientation of the electrode to the two-photon microscope and thus to the captured images. Owing to the very good visibility of the electrode in 2P-LSM, a better combination of the two different methods was possible besides a fast detection of the field of view. This enabled, for example, the use of the weighted average value of the ECoG at the FOV or the use of differential voltages from the individual electrode locations around the FOV. In addition, the local coordinate system could be used to check the positioning of the mouse in repeated imaging sessions.

To find the global coordinates of the window corners, the following process was established. The scan head of the microscope was sequentially moved to three corners of the window until each corner was inside a target cross to find the x- and y-coordinate. The target cross was printed on a transparency and fixed on the monitor. The z-coordinate (distance to the objective) was determined by the image brightness. The z-values could be identified by the focused laser beam as soon as the maximum image intensity was reached at the corner. These coordinates were used to calculate two vectors ($\vec{p}_1, \vec{p}_2$) between the three corners and the normal vector $\vec{n}$ of the electrode plane (with the vector product of the two vectors). The upper-left corner was used as the origin (point p_0) for the local and global coordinate system so that the position of the FOV could be determined with respect to a common reference point (Figure 4.16B, C, calculation of rotation angles are in Appendix Chapter 8.8). In addition, the relation of the FOV to the cortical surface could be estimated more easily (Figure 4.16D). Since the top-left corner was selected as the origin, the FOV was in the negative x-axis, negative y-axis, and positive z-axis areas with respect to the global coordinate system. The accuracy of this method depended strongly on the identification of the corners of the observation window. To be able to estimate the detection error, the coordinates of point 3 (p3) were calculated from the measured coordinates of p1 and p2 and compared with the measured coordinates of p3. (Figure 4.16E). Despite this manual and subjective procedure (position to the target cross and image

brightness), all coordinate deviations were in the lower µm range, with the error in the z-direction being slightly higher than in the x- and y-directions.

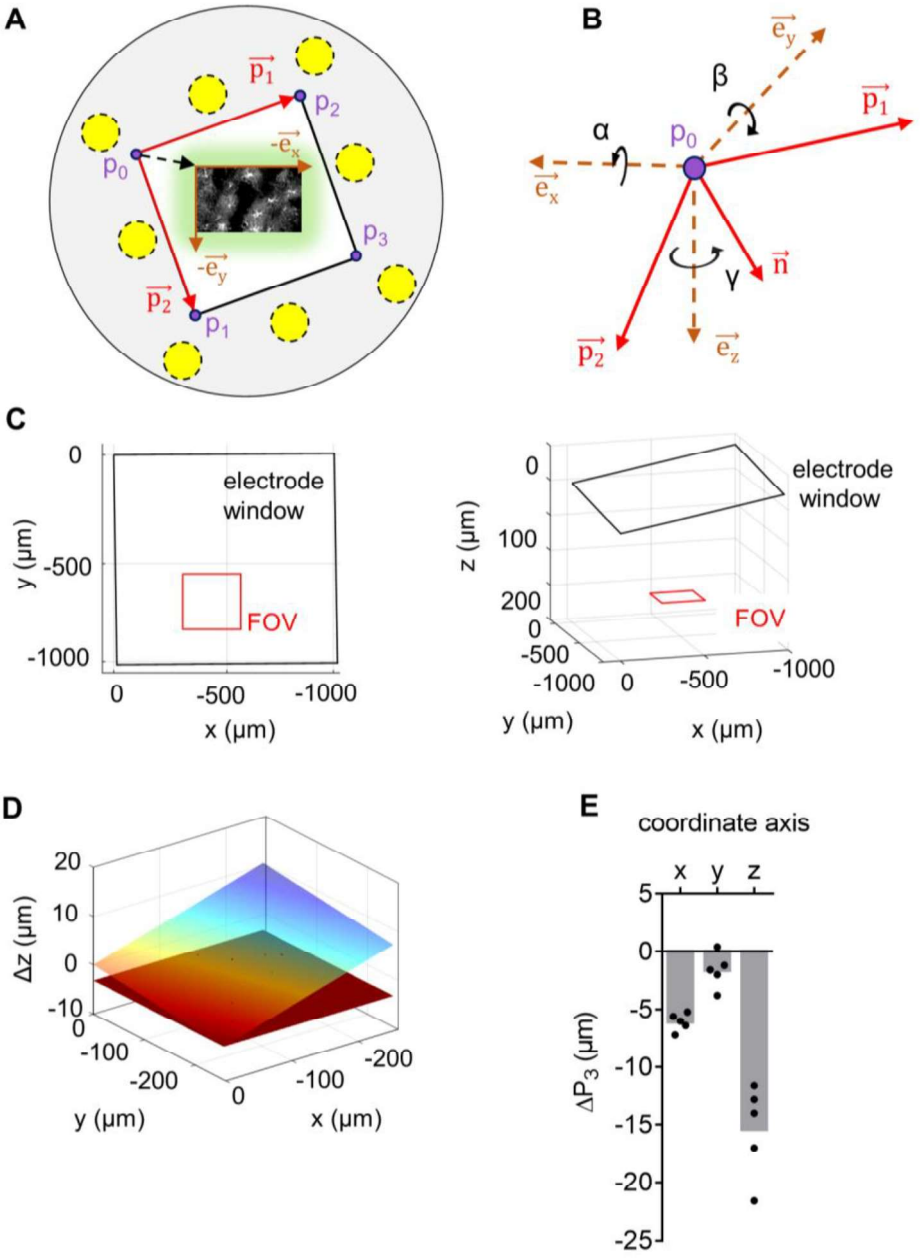

Figure 4.16: Using electrode geometry to specify location and orientation of FOV. A) Example of translation and orientation shift between the electrode and two-photon image. B) Graphical representation of local and global coordinate systems in the 3D room, including rotation angles. C) Example of the orientation of one square electrode window and FOV position. Left: top view. Right: 3D view. D) Distance difference in the z-direction between the electrode window (cortical surface) and the FOV. The red plan represents the FOV. The multi-coloured plan is orientated to the electrode window (surface). The FOV were nearest to the surface at coordinate (x = 0, y = -256) and most distant at coordinate (x = -256, y = 0). E) Measurement error. Derivation of the coordinates from the calculated point 3 (p3 = p1+p2) to the measured p3.

4.8 Linking Ca^{2+} signals and electrical recordings

4.8.1 Depth of anaesthesia affects ECoG and Ca^{2+} signals

To demonstrate the functionality of the combination of ECoG recording and Ca^{2+} signals by 2P-LSM, the depth of anaesthesia was varied to change the physiological condition and thus the activity of neurons and astrocytes. The electrical signals were recorded with the multichannel g.USBamp system at a sampling rate of 1.2 kS/s and bandpass filtering of 0.5 Hz to 250 Hz. In addition, a notch filter (50 Hz) was applied. In each study, an eight-channel electrode array with round-shaped electrode sites was applied to a GLAST-CreERT2 x R26-CAG-lsl-GCaMP3 mouse (Ca^{2+} signals in astrocytes). The synchronization of 2P-LSM and recording was achieved by acquiring a mirror control signal with one channel of the recording system. In this way, a high synchronization accuracy within a single 2P image could be realized. Still, thirty-five days after electrode application, high-quality 2P-LSM and ECoG recording over a long period of time (>30 minutes) was possible without any limitations (Figure 4.17).

An increase in the overall number of Ca^{2+} events occurred when the anaesthesia was decreased (Figure 4.17D) which was in line with reports of others (Thrane et al, 2012). The event classification also showed that the numbers per time of large, medium, and small signals in a mouse within the same condition were different (for example see awake situations Figure 4.17D). This means that an exact determination of the actual depth of anaesthesia only from the Ca^{2+} related signals was not possible. The mean image brightness reflects the strength of the Ca^{2+} signals and becomes high with low anaesthesia. The recorded ECoG could be used to differentiate various conditions ranging from deeply anaesthetized to awake.

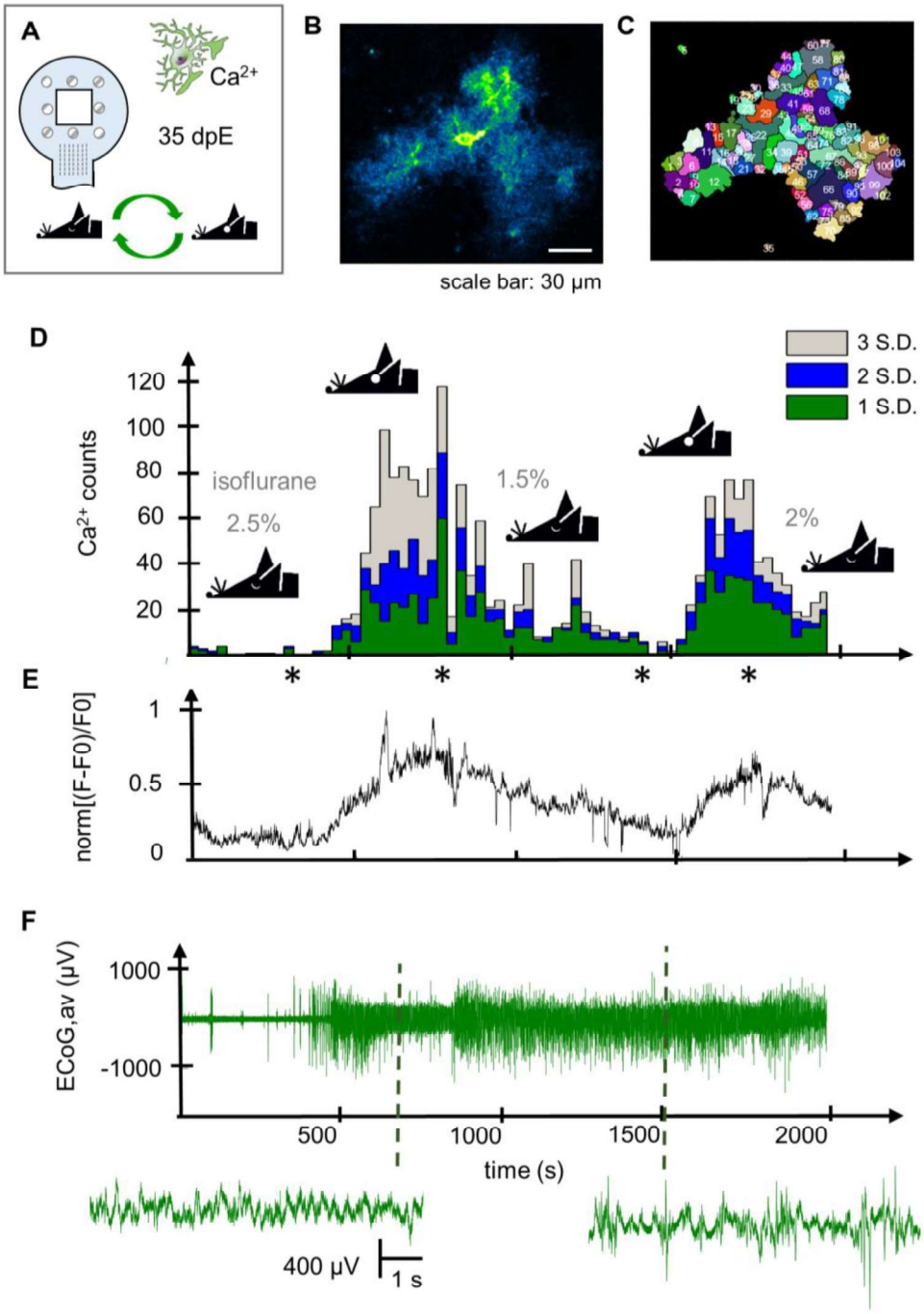

Figure 4.17: Ca^{2+} signals in astrocytes and ECoG change with anaesthesia. A) Study set-up. Long-term 2P-LSM of Ca^{2+} signals in a GLAST-CreERT2 x R26-CAG-lsl-GCaMP3 mouse (laser power: 17%; frame rate: 1.5 Hz; FOV size 180 µm x 180 µm; resolution: 360 pixel x 360 pixel). ECoG recording with an eight-channel electrode array (sampling rate: 1.2 kHz; notch filter: 50 Hz; bandpass filtering: 0.5 Hz – 250 Hz). Study was performed at 35 days post electrode surgery. Isoflurane was changed in the range of 0% and 2%. B) Two-photon image of the FOV with few astrocytes covering distinct regions. C) Automated detection of regions of interest (software MSparkles). D) Time trace of Ca^{2+} event classification. Black stars indicate time points of isoflurane concentration change. E) Normalized mean image brightness of the complete images. F): Average ECoG trace of all channels with two subsets. Left: awake mouse; right: anesthetized mouse.

4.8.2 Cortical injection of kainate increases synchronized neuronal spiking activity followed by astroglial Ca^{2+} signals

With the injection of kainate into the contralateral cortex after three days post electrode application, the activity of the cellular network activity in the cortex was changed. A GLAST-CreERT2 x R26-CAG-lsl-GCaMP3 mouse was used to observe the Ca^{2+} related responses in astrocytes. After kainate injection, large neuronal spiking activity was visible in each channel of the recording (Figure 4.21), showing the global spread of pathological neuronal firing. The correlation between the individual channels resulted in the typical value ranges corresponding to the inter-electrode distance for awake mice in the phases of normal activity. In the high spiking phases, the channel correlation increased dramatically independently of the amplitude of the ECoG. For the analysis of the Ca^{2+} related signals, the mean image brightness was calculated and a classification of single signal events was performed with the software MSparkles.

A small increase in the mean image brightness and in the Ca^{2+} signal events over time was visible (Figure 4.21D) independently to the ECoG. The signal energy (Chapter 3.6.3, Eq. 5) of the averaged ECoG represents the neuronal activity, which changed more than the astrocytic signals. Only if the neuronal activity was strongly increased over a longer period of time, a strong Ca^{2+} signal change was achieved. Mouse movements, which could lead to Ca^{2+} events, could be identified with the calculation of the correlation of two subsequent images. The soft brain tissue was shaken by the mouse movements, leading to different image contents and a rapid and strong decrease in correlation. However, the result showed that no astrocytic signal change could be observed in relation to the movement. Additionally, it became visible that the periods of high spiking neuronal activity ended mostly with a movement of the mouse.

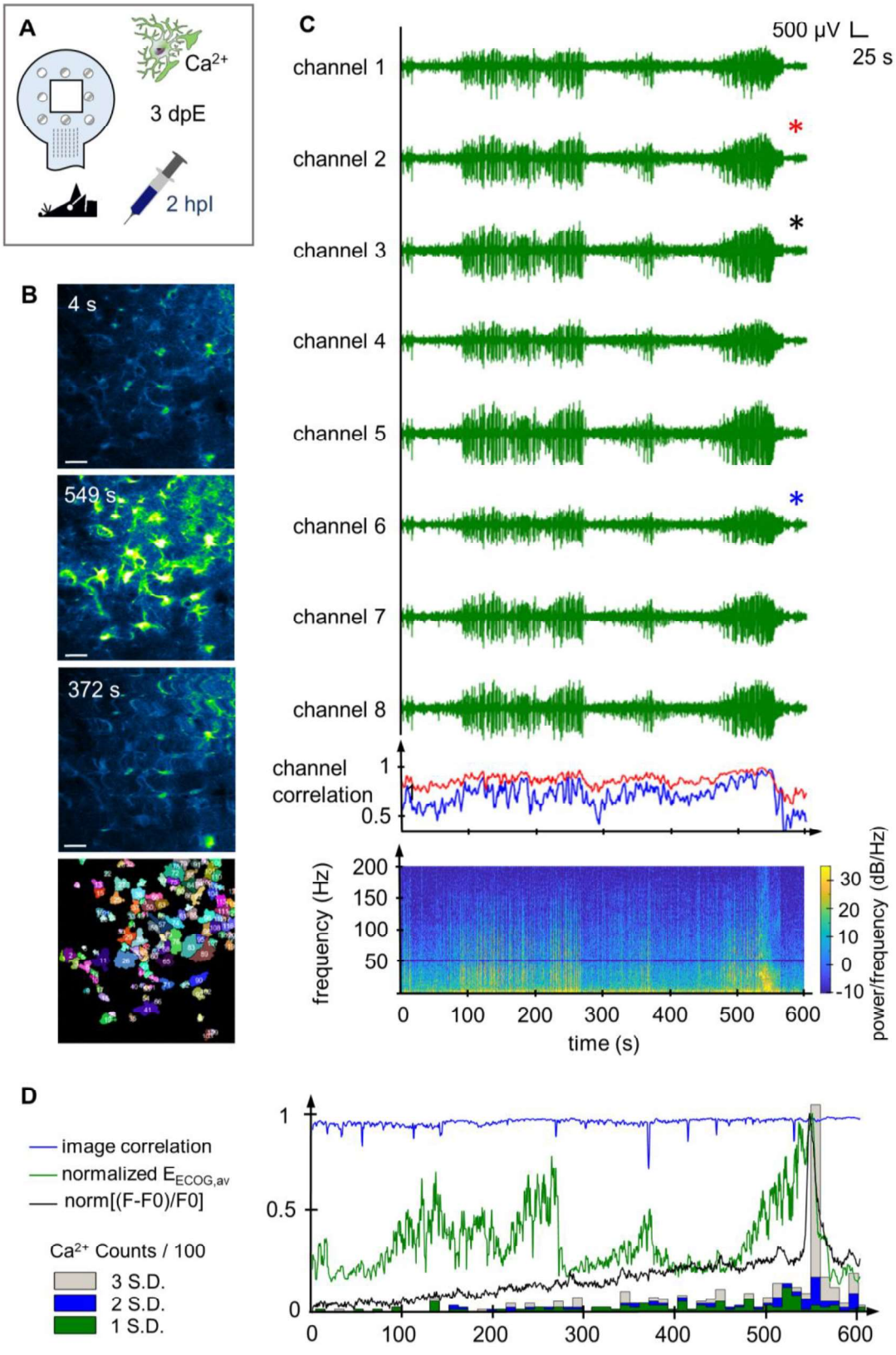

Figure 4.18: Example of kainate-induced neuronal activity and astrocytic Ca^{2+} related signals. A) Study set-up. 2P-LSM of Ca^{2+} related signals in a GLAST-CreERT2 x R26-CAG-lsl-GCaMP3 mouse (laser power: 15%; frame rate: 2 Hz; FOV size: 256 µm x 256 µm; resolution: 512 pixel x 512 pixel). ECoG recording with an eight-

channel electrode array (sampling rate: 1.2 kHz; notch filter: 50 Hz; bandpass filtering: 0.5 Hz – 250 Hz). Study was performed at three days post electrode surgery. Awake mouse approximately two hours post kainate injection. B) Three single two-photon images with a Ca^{2+} related signal in a neuronal non-spiking phase, the Ca^{2+} related signal in the last neuronal high-spiking phase and one image during a movement (scale bar: 50 µm). The last image in the column shows the detected regions of interest (software MSparkles). C) The ECoG of all eight channels show the kainate-induced neuronal spiking activity. The channel correlations of channel three (black star) to channel two (red star, red line) and of channel three to channel six (blue star, blue line) were stepwise calculated (1 s window size, 50% overlap). The spectrogram shows the frequency over time of the ECoG average. D) Line graphs with the normalized traces for the image brightness (black), the signal energy of the averaged ECoG (green) and the result of the image-to-image correlation (blue). The counts of Ca^{2+} event classification are divided by one hundred.

4.9 Surface electrodes can be used for electrical activation of the cortical tissue

The cortical tissue could be electrically activated using the surface electrodes with the eight rectangular-shaped electrode sites. For the stimulation studies, the two inner electrode sites left and right of the observation window were used together to apply an electrical current. This was selected in order to ensure a broad current distribution over the electrode window and thus to allow greater flexibility in the selection of the field of view. The minimum amplitude of the biphasic charge compensated stimulation current had to be estimated prior to each stimulation study. The threshold to activate the cell structure changed over time after electrode application and was therefore associated with the regrowth of the bone. The applied current ranged from 150 µA to 600 µA. Two of the outer electrode sites were used for electrical recording (Figure 4.19). As recording device, the PowerLab system was used, as it was more tolerant of stimulation artefacts compared to the g.tec system. However, during the stimulations, the amplitude exceeded the input range of the amplifier and no signals could be observed. But the electrical network activity was visible before and after the stimulation, with no indication of a direct signal change related to the stimulation.

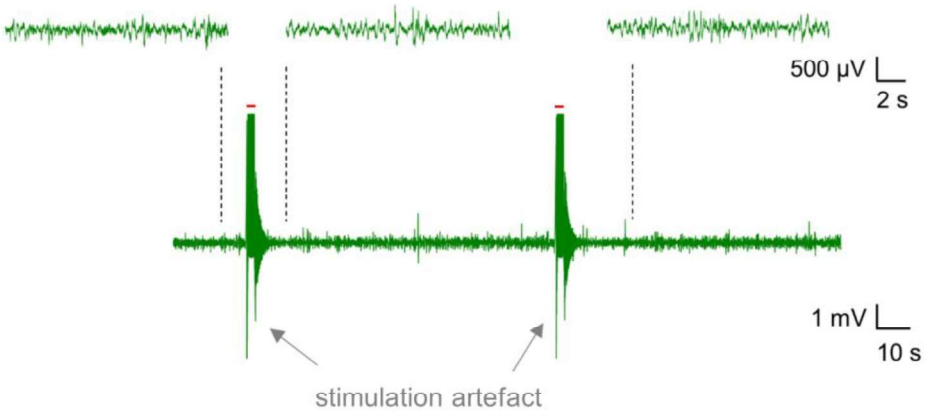

Figure 4.19: Example of ECoG recorded during a stimulation experiment with the PowerLab system (sampling rate: 2 kS/s; notch filter: 50 Hz; bandpass filtering: 0.5 Hz – 200 Hz; biphasic stimulation; 50 Hz; 300 µA, 0.5 ms pulse width; 100 pulses). Red bars indicate stimulation periods. The three insets show zoom-views of the ECoG before and after the electrical stimulation.

4.9.1 Response of the neuronal network changed with stimulation frequency

Train stimulations with two different frequencies and various amplitudes were used to investigate the response of the neuronal tissue (Figure 4.20, Figure 4.21). With a frequency of 50 Hz, increasing Ca^{2+} transients in neurons could be observed with increasing stimulation amplitude. In addition, a stable cell response was visible by applying repetitive train stimulations with 50 Hz train frequency at the same amplitude. This was different using a stimulation frequency of 10 Hz. The Ca^{2+} signals became smaller using the same train stimulation amplitude repetitively. This effect could be overcome by increasing the stimulation current. The peak value of the neuronal response was visible after applying about 100 stimulation pulses. When using more pulses in the train stimulation, a decrease in the Ca^{2+} related signals were visible (Figure 4.21B).

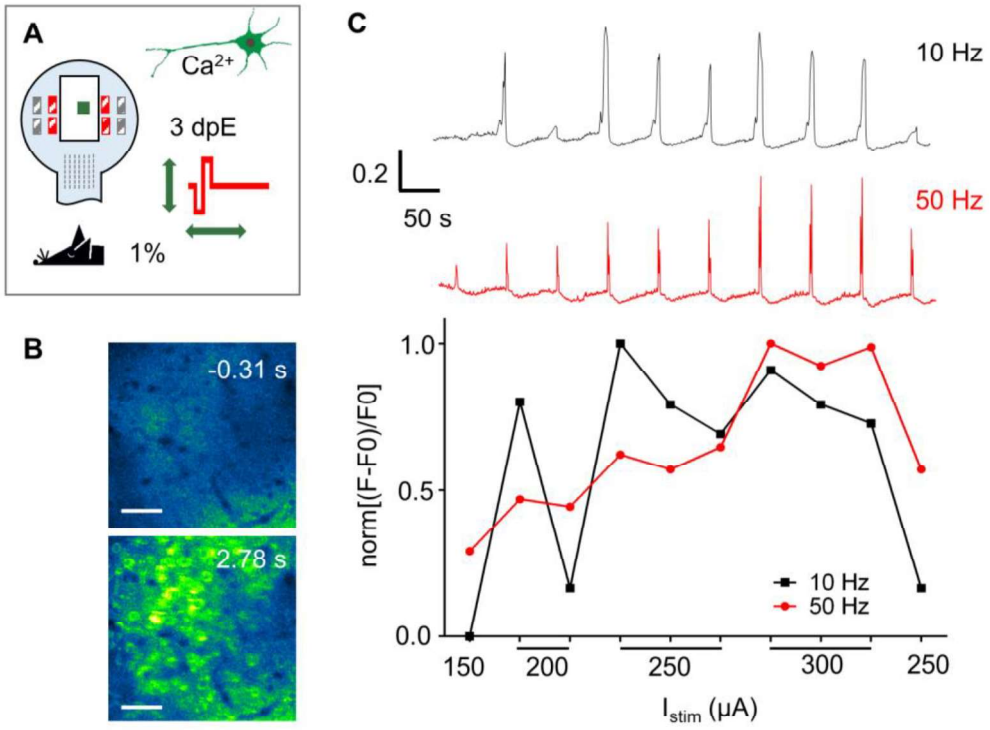

Figure 4.20: Response of the neuronal network to two different stimulation frequencies. A) Study set-up. 2P-LSM of Ca^{2+} related signals in a Nex-Cre x R26-CAG-lsl-GCaMP3 mouse (laser power: 17%; frame rate: 3.2 Hz; FOV size: 256 µm x 256 µm; resolution: 512 pixel x 512 pixel; about 160µm beneath the dura). Biphasic charge compensated stimulation pulses were applied, varied in amplitude (150 µA – 300 µA; 0.5 ms pulse width; 100 pulses, train stimulation every 93 s) and frequency (10 Hz and 50 Hz). The mouse was anaesthetized with 1% isoflurane. B) Two single 2P-LSM images representing the Ca^{2+} signals prior to and during one stimulation (scale bar: 50 µm). C) Relative Ca^{2+} signal change of the mean image intensity during two sequences of electrical stimulation wit current amplitudes of 150 µA, twice 200 µA three times 250 µA and 300 µA and once with 250 µA. Upper trace shows the response to 10 Hz stimulation. Lower trace for 50 Hz. The graph below shows the relation of the peak values ((F-F0)/F0). With 50 Hz stimulation, a Ca^{2+} change was visible at 150 µA and increased with increasing current amplitude and remained stable for the same current amplitude. For electrical stimulation with 10 Hz, the first response was visible at 200 µA and was reduced using the same stimulation amplitude in sequence. A significant decrease was also visible for the last stimulation, where the current amplitude was lower than in the previous one.

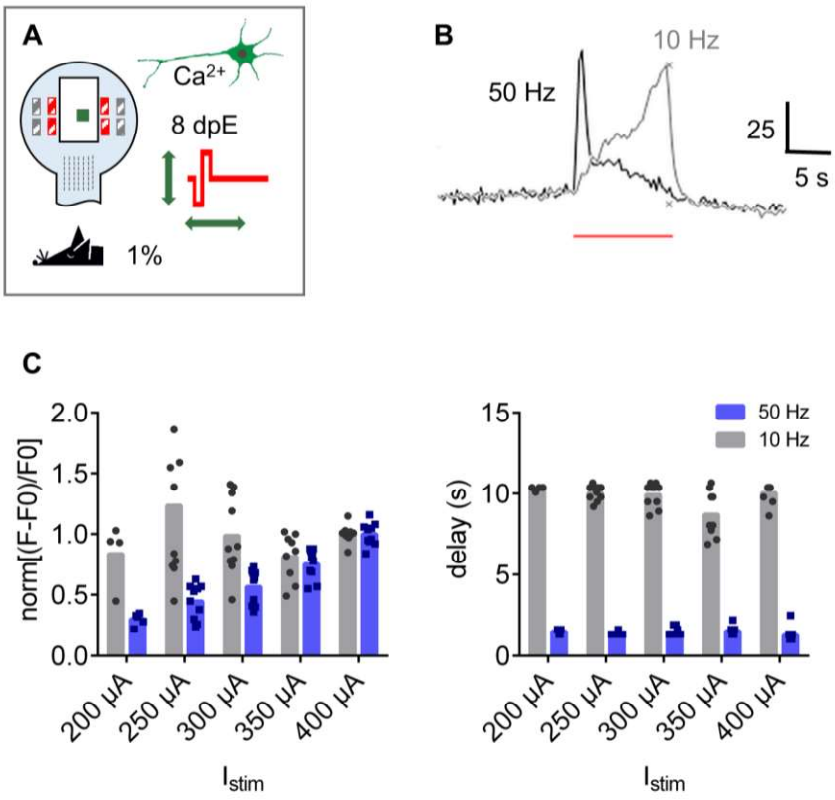

Figure 4.21: Response of the neuronal network to stimulations of 10 s length at two different frequencies. A) Study set-up. 2P-LSM of Ca^{2+} related signals in a Nex-Cre x R26-CAG-lsl-GCaMP3 mouse (laser power: 22%; frame rate: 3.4 Hz; FOV size: 256 µm x 256 µm; resolution: 512 pixel x 512 pixel; about 165 µm beneath the dura). Biphasic charge compensated stimulation pulses were applied, varied in amplitude (200 µA – 400 µA; 0.5 ms pulse width, stimulation time 10 s) and frequency (10 Hz and 50 Hz). The mouse was anaesthetized with 1% isoflurane. B) Response of five neuronal cell bodies within the FOV to train stimulations with 50 Hz and 10 Hz. Each stimulation train was applied twice. C) Statistical graphs representing the normalized peak values (F-F0)/F0 of the mean image intensity value of somas and the delay time between stimulation onset and the peak amplitudes.

4.9.2 Anaesthesia decreased the response of the neuronal network to the electrical activation

Electrical stimulations were performed in mice at different levels of isoflurane concentrations to investigate how anaesthesia affects the response of neuronal networks. A sequence of stimulations with a frequency of 50 Hz was applied for four different isoflurane concentrations (1.5%, 1%, 0.5%, and 0%). Three different current

amplitudes were used, and for each current amplitude, the stimulation was performed twice. The mean image intensity of the two-photon images was analysed.

The neuronal network could be activated across all levels of anaesthesia (Figure 4.22). After each stimulation, the Ca^{2+} signals were reduced in comparison to the previous base level. But, they recovered within a time range of approximately 35 s to 70 s depending on the isoflurane level, but not on the stimulation strength (Figure 4.22B, C). From the presentation of the Ca^{2+} transients, it can be seen that the activation of the neuronal network changes with the depth of anaesthesia (Figure 4.22C). Under lower anaesthesia, two peaks become clearly visible. The sources of these peaks can be estimated from the short image series of every second image from the original recording (frame rate 3.42 Hz, Figure 4.22E). The image at time 0 s is the image directly at the stimulation onset. Two frames later, the activation of the neuropil was clearly visible (first peak in the Ca^{2+} transients in Figure 4.22C ①), which disappears before the cell bodies become activated (second peak, ②).

The graphs (Figure 4.22D) represent the mean values of the signal changes in the neuropil (①) and somata (②) sorted along the stimulation amplitude and isoflurane. The activation of the neuropil seems to be more affected by the stimulation strength than by the isoflurane concentration. The Ca^{2+} related signals increased with increasing stimulation amplitude and with decreasing anaesthesia from 1% to 0%. With an isoflurane level of 1.5% the response to electrical stimulation was higher than for 1%. This might be an effect of biological variation within one experiment. Over all stimulations, the onset of Ca^{2+} signal was always within the first frame (0.29 s for isoflurane level of 1.5% and 1%; 0 s or 0.29 s for isoflurane level of 0.5% and 0%). The first peak appeared at 0.88 s ± 0.29 s (3 frames ± 1 frame), the second peak at 2.63 s ± 0.29 s and the signal ended at 3.51 s ± 0.29 s for isoflurane levels of 1.5% and 1% or 3.51 s ± 0.58 s for isoflurane levels of 0.5% and 0%. A Ca^{2+} signal undershoot became visible after the activation of the somas. The undershoot length (time from end of falling edge until the previous signal intensities were reached; ③) changed along the anaesthesia level. It was independent from the stimulation strength. Thus, the time mean values of all stimulations at one isoflurane level is presented.

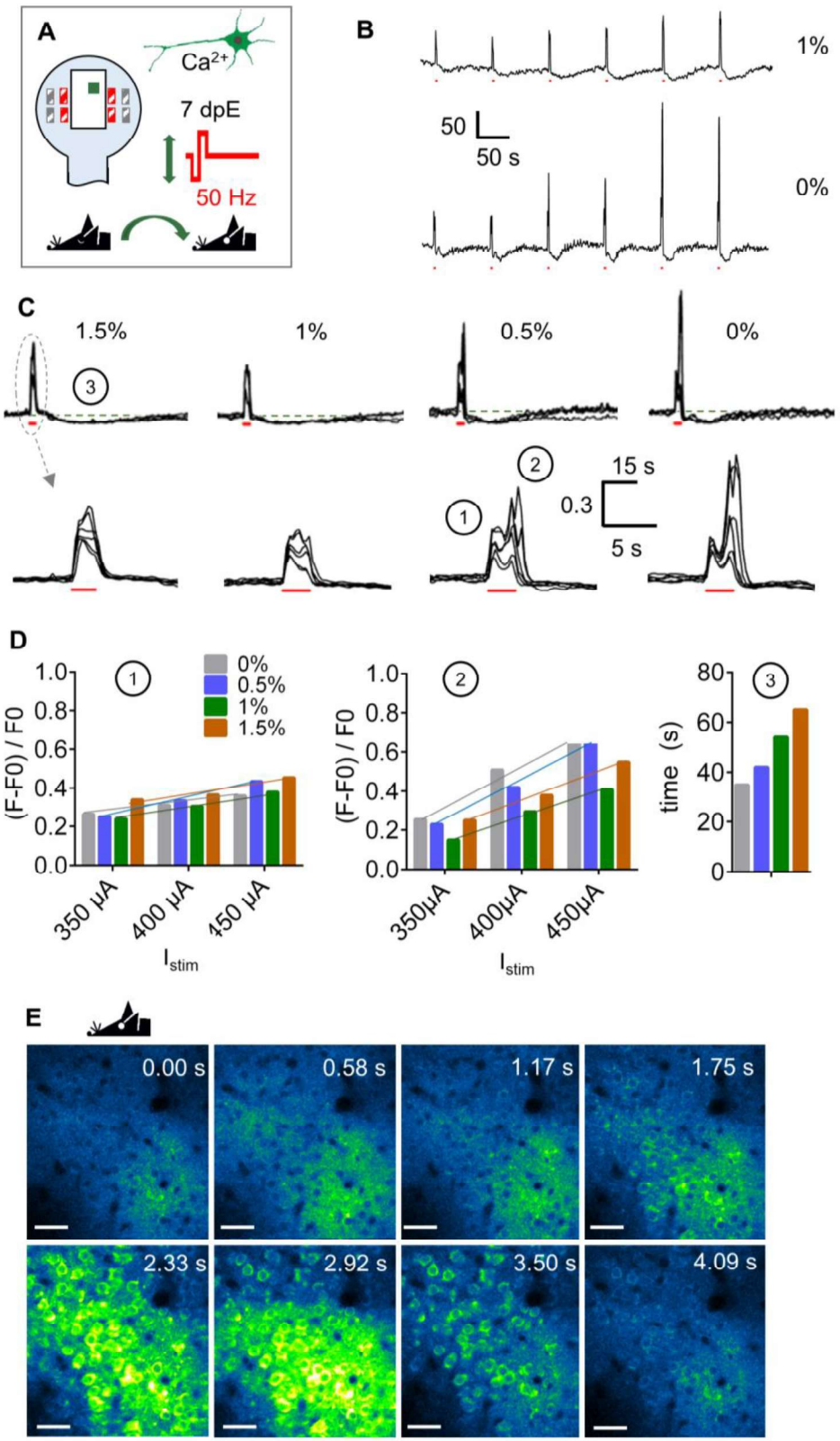

Figure 4.22: Response of the neuronal network to different depths of anaesthesia. A) Study set-up. 2P-LSM of Ca^{2+} related signals in a Nex-Cre x R26-CAG-lsl-GCaMP3 mouse (laser power: 15%; frame rate: 3.4 Hz; FOV size: 256 µm x 256 µm; resolution: 512 pixel x 512 pixel; about 165 µm beneath the dura). Biphasic charge compensated stimulation pulses with 50 Hz with different amplitudes (100 pulses with 350 µA,

400 µA, and 450 µA; 0.5 ms pulse width, every 100 s) were applied. The anaesthesia was changed ranging from1.5% to 0%. B) Fluorescent mean intensity traces of the two-photon images for the stimulation sequence under 1% and 0% isoflurane concentration. Red dots indicate stimulation periods. C) Overlay of the single responses of each stimulation sequence in two different scales. D) Statistics showing the maximum values of first (left graph) and second (middle graph) peak sorted by stimulation amplitude and isoflurane concentration. The right graph shows the times until the Ca^{2+} signal intensity comes back to the base level after stimulation. E) Selected image series of every second image from the original recording. Time index is given from stimulation onset. Scale bar: 40 µm

4.9.3 Estimation of the neuronal Ca^{2+} spreading direction indicates direct electrical activation in layer 1

In the time series of Ca^{2+} images, a direction of cell activation was visible. However, the visual impression was strongly influenced by the spatial variable base brightness, so that bright areas of the images appeared to be activated first. Because of the limited frame rate for a specific image size, it was not possible to accurately detect a time difference in neuronal cell-body activation. To overcome this limitation, the image intensity of every pixel along a line was considered (example given in Figure 4.23A-a, white arrow). With the time series of the values (Figure 4.23A-b) the two steps in activation (① and ②, see previous chapter) were visible, more clearly with 50 Hz stimulation than with 10 Hz stimulation. But, on the 10 Hz stimulation, the time shift of the spatially distributed neuronal activation was better visible due to the higher number of single images per stimulation period. In order to obtain a value in relation to these time shifts, the position of the maximum values per pixel column within selected time points were determined. Thereafter, a linear approximation of these values was calculated using Matlab and the gradient of the linear function was chosen to characterize the time shift along the line.

This method was applied around a centre point for all image directions (Figure 4.23A-a, white circle) and polar plots representing the gradients and thus the spreading directions were created (Figure 4.23A-d). This could be compared with the geometric information found with the electrode corners (orientation and location of the FOV given in Figure 4.23A-c and the difference in the z-direction from the FOV to the cortical surface given in Figure 4.23A-d). As result, a strong direction of activation goes from the cortical surface down to deeper structures. This indicated, that in the field of

view the electrical stimulation activated the axons in layer 1 of the cortex. The change of the stimulation polarity did not largely change the direction of activation (Figure 4.23B). This additionally indicated that the spread of Ca^{2+} signals was along the neuronal structures coming from layer 1.

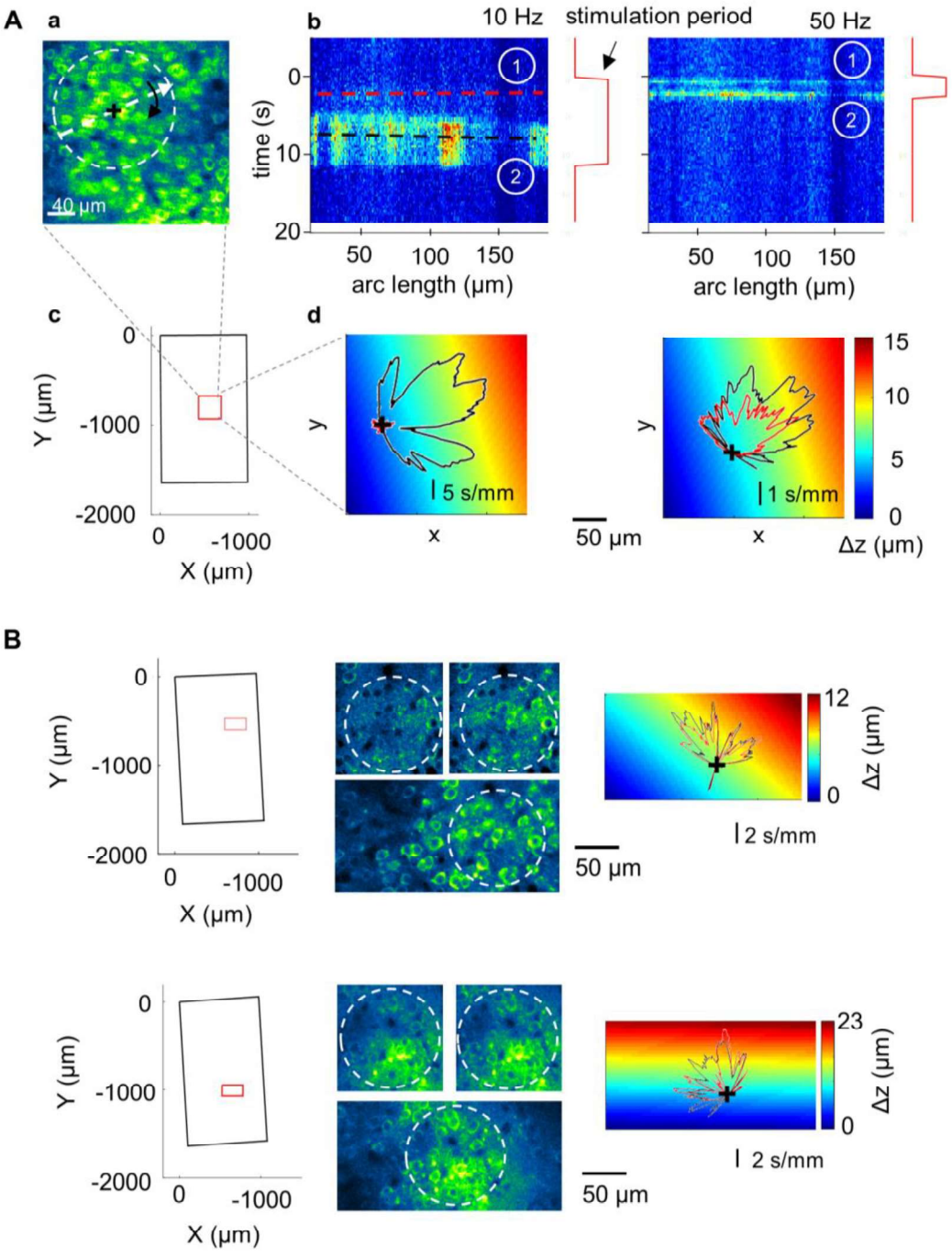

Figure 4.23: Spatial spread of Ca^{2+} signals in neuronal networks. A-a) Image of activated neurons including the single line (black arrow) which was analysed for the activity plots in A-b) for two different frequencies (10 Hz and 50 Hz). ① indicates the first activation, ② the second activation. The two lines (red and black) inside the 10 Hz activity plot represent the linear approximation of the time points of the maximum

values. The red lines right to the activity plots represent the time periods of stimulation. A-c) top view of FOV orientation and position in relation to the electrode window. A-d) heat maps representing the difference in the z-direction over the FOV overlaid with the polar plots of activation. Red: first activation – neuropil. Black: second activation - somas B) Two examples for 50 Hz biphasic stimulation with different stimulation polarities. Viewing from the electrodes left from the window the colours in the polar plots representing the different polarities. Red: cathodic first; black: anodic first. The images in the middle show three subsequent time points of cell activation.

4.9.4 Ca^{2+}-signals of cortical astrocytes follow neuronal activation

Ca^{2+} transients in cortical astrocytes could be provoked by electrical stimulation (Figure 4.24). Owing to the results from the activation of the neurons, trains of stimulation with 100 pulses were used. The cell bodies as well as the processes could be activated. The peak of the astrocytic Ca^{2+} related signals was found after the end of the stimulation and the signals appeared for several seconds.

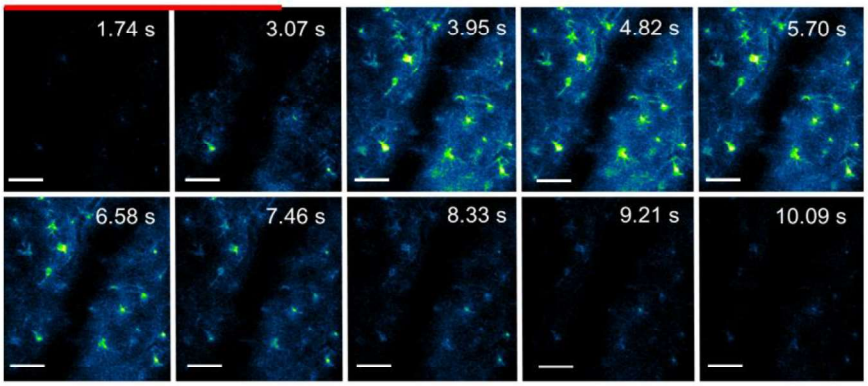

Figure 4.24: Image series of astrocytic Ca^{2+} related signals. Time index is given from stimulation onset. Red bar indicates active stimulation with 50 Hz and stimulation amplitude of 450 µA (GLAST-CreERT2 x R26-CAG-lsl-GCaMP3 mouse, 11 dpE, laser power: 20%; frame rate: 2.3 Hz; FOV size: 256 µm x 256 µm; resolution: 512 pixel x 512 pixel; 90µm beneath the dura). Scale bar: 50 µm

In contrast to the neuronal activation, the raise of Ca^{2+} related signals followed more an all-or-nothing behaviour than a gradual increase in the response with the stimulation amplitude (Figure 4.25). The delay of the activation peak to the stimulation onset indicates that the astrocytic response followed neuronal activation. For 20 Hz stimulation, the activation threshold was higher than for 30 Hz and 50 Hz stimulation. With a current amplitude of 400 µA, no astrocytic reaction was visible, with 450 µA not

every 20 Hz but every 30 Hz and 50 Hz stimulation provoking an astrocytic response. With the exception of 10 Hz stimulation, every stimulation with a stimulation amplitude of 500 µA was effective. Moreover, no significant difference in the electrically activated Ca^{2+} related signals with the variation of the isoflurane concentration were visible at a stimulation amplitude of 500 µA (Figure 4.26).

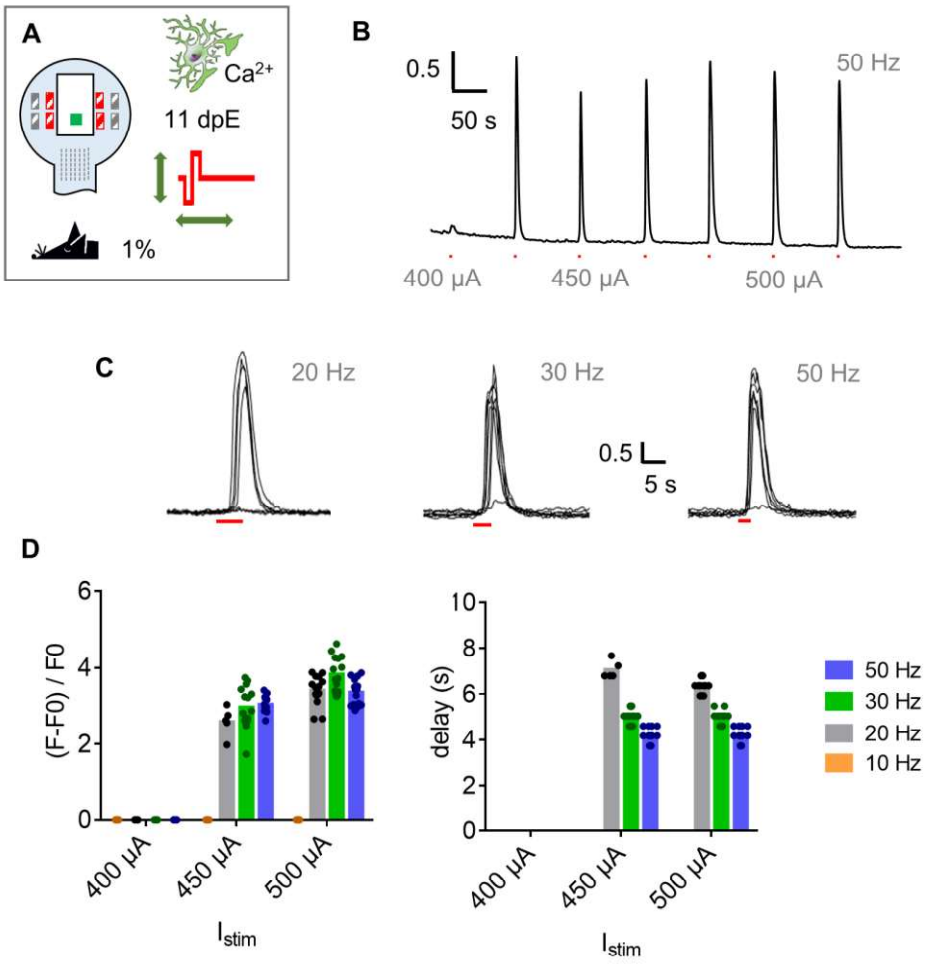

Figure 4.25: Astrocytic Ca^{2+} response to different stimulation amplitudes and frequencies. A) Study set-up. 2P-LSM of Ca^{2} related signals in a GLAST-CreERT2 x R26-CAG-lsl-GCaMP3 mouse (laser power: 20%; frame rate: 2.3 Hz; FOV size: 256 µm x 256 µm; resolution: 512 pixel x 512 pixel; about 90 µm beneath the dura). Biphasic charge compensated stimulation pulses with different frequencies (10 Hz, 20 Hz, 30 Hz, and 50 Hz) and with different amplitudes (100 pulses with 400 µA, 450 µA, and 500 µA; 0.5 ms pulse width) were applied. The anaesthesia was set to 1%. B) Mean image intensity of a stimulation series with a train frequency of 50 Hz (sequence: 400 µA, 3 x 450 µA, 3 x 500 µA). C) Ca^{2+} related signals of an astrocytic cell body for different stimulations. D) Statistical graphs to signal peaks of cell bodies and delay times between stimulation onset and signal peak (at 450 µA and 20 Hz stimulations, only the successful stimulations were included).

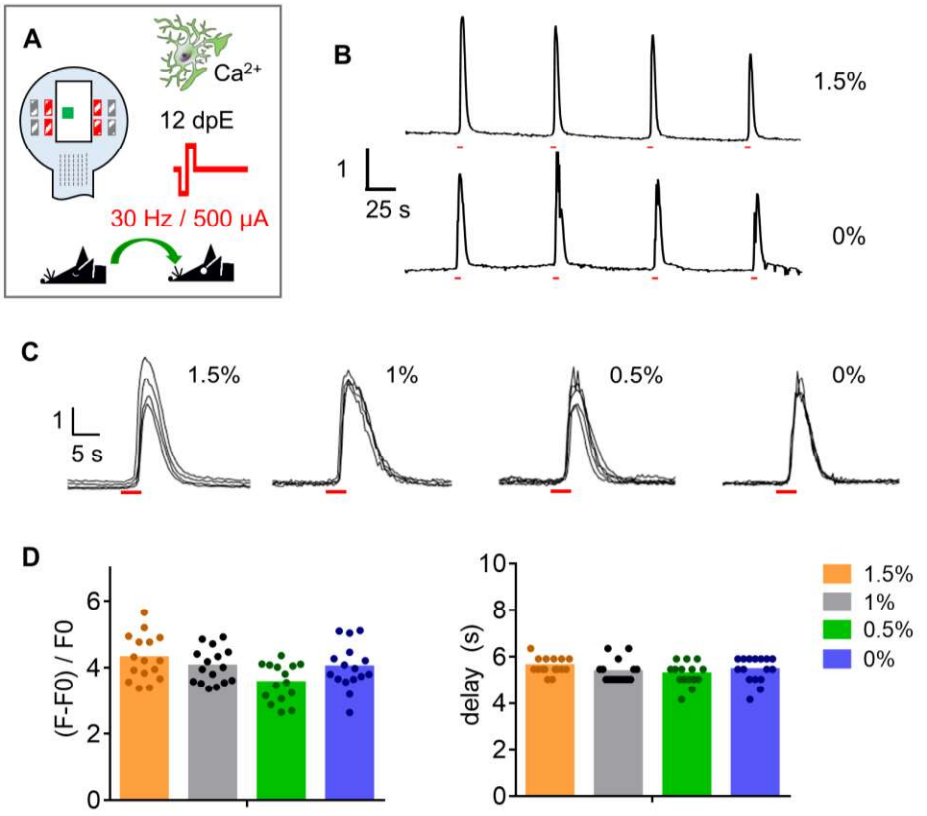

Figure 4.26: Astrocytic Ca^{2+} response to a train stimulation under different anaesthesia conditions. A) Study set-up. 2P-LSM of Ca2+-related signals in a GLAST-CreERT2 x R26-CAG-lsl-GCaMP3 mouse (laser power: 23%; frame rate: 2.3 Hz; FOV size: 256 µm x 256 µm; resolution: 512 pixel x 512 pixel; 85 µm beneath the dura). Biphasic charge compensated stimulation pulses (100 pulses; 0.5 ms pulse width) with a frequency of 30 Hz and an amplitude of 500 µA were applied. The anaesthesia ranged from 1.5% to 0%. B) Mean image intensity of a stimulation series with a train frequency of 30 Hz for an anesthetized and awake mouse. C) Ca^{2+} related signals of an astrocytic cell body for train stimulations during different depths of anaesthesia (1.5%, 1%, 0.5% and 0% isoflurane). D) Statistical graphs to signal peaks of cell bodies and delay times between stimulation onset and signal peak.

4.10 LCP surface electrodes to stimulate and record neural activity of the spinal cord

To investigate the neuronal fibres in spinal cord *in vivo*, two surface electrodes were applied to the spinal cord of GFAP-CreERT2 xRosa26-CAG-lsl-GCaMP3 mice expressing GCaMP3 in spinal astrocytes. The caudal electrode was used for electrical stimulation and the cranial electrode for recording of the electrical activity (PowerLab system; sampling rate: 40 kS/s; 50Hz notch filter). The mice were anaesthetised with an isoflurane level of 1.5%.

4.10.1 Activation of afferent and efferent fibres in spinal cord

In addition to LCP surface electrodes, two needle electrodes (28mm x 0,45mm, SCHULER GmbH Medizintechnik) were applied to the femoral muscle of the left hind leg acquiring the muscle activity (Figure 4.27). The recording capability was proven by recording of the electrical baseline as well as the response of a tactile stimulation by pinching the left hind paw (Figure 4.27B). Paw pinching could be clearly identified and resulted in a signal change of 20 µV to 30 µV. The visible spiking activity in both traces had a repetition rate of 6.3 Hz. Thus, this was most likely related with the heartbeat (378 beats per minute) of the anaesthetized mouse.

Unipolar stimulation pulses in the range of -50 µA to -500 µA (20 pulses per amplitude for signal averaging) with a pulse width of 50 µs were applied to stimulate the spinal cord (Figure 4.27D,E). The stimulation artefact (①) was continuously present. Beginning with a stimulation amplitude of 100 µA, a first neuronal response appeared (②, ③). The fastest response of the afferents (②) was visible approximately 300 µs after stimulation onset. With an interelectrode distance of 5 mm a nerve conduction velocity of about 20 m/s (250 µs) could be estimated. A second response of the sensory fibres (③) appeared within 0.9 ms to 1.7 ms after stimulation onset. Because of the signal shape this response might had been the result of the superposition of several fibres with different nerve conduction velocities in the range of 5.5 m/s to 3 m/s. The electrical evoked response was at least five-fold higher than the tactile evoked neural signals. A leg movement could be visually observed and a signal became visible in the electromyogram (④) if the amplitude was at least -400 µA. An additional response appeared in the electroneurogram.

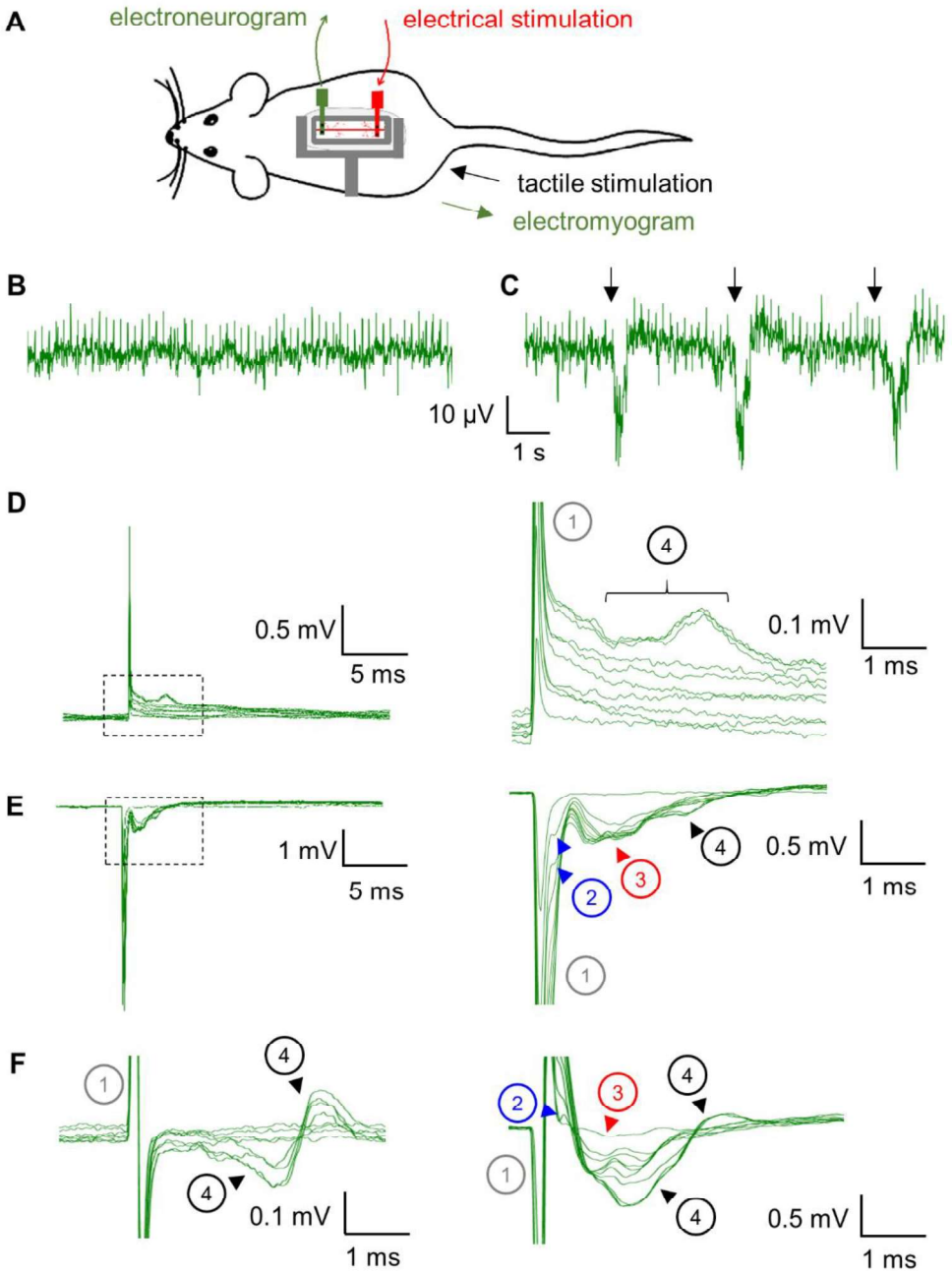

Figure 4.27: Recording of evoked potentials in spinal cord. A) Study set-up. Two spinal surface electrodes were applied. The caudal electrode was used for electrical stimulation, the cranial electrode for recording of the electroneurogram. Two needle electrodes were placed into the left hind femoral muscle to record the electromyogram. A forceps was used to pinch the left hind foot for tactile stimulation. Recording device: PowerLab system; sampling rate: 40 kS/s; 50 Hz notch filter activated. The mouse was anaesthetized using 1.5 % isoflurane. B) 15 s recording of the spontaneous spinal electrical activity. C) 15 s recording of the spinal signal with three tactile stimulations. Traces in B) and C) were filtered with a moving median filter (10 ms window length). D) Electromyogram and E) electroneurogram in two scales after unipolar single pulse electrical stimulation (average of 20 stimulation pulses). Stimulation amplitudes: -50 µA to -500 µA in -50 µA steps; pulse width: 50 µs. F) Electromyogram (left) and electroneurogram (right) to bipolar single pulse stimulation (average of 20 stimulation

pulses). Stimulation amplitudes: ±50 µA to ±500 µA in 50 µA steps; pulse width: 100 µs. ①: stimulation artefact. ②: Electroneurogram related to fastest somatosensory fibres. ③: Electroneurogram of additional somatosensory fibres. ④: Electroneurogram and electromyogram related to muscle activity. Leg movement was visually observed; movement was stronger in the bipolar stimulation than in the unipolar stimulation.

The study had been supplemented by using biphasic stimulation currents (Figure 4.27D). The pulse width of the stimulation currents was set to 100 µs being able to stimulate in a similar current amplitude range, and to avoid an additional enlargement of the stimulation artefact due to the properties of the input amplifier. The electroneurogram contained the same (as above described) signal parts with stimulation artefact (①), two visible responses from the afferent fibres (②, ③), and a response related to the leg movement (④). A stimulation amplitude of ±350 µA was sufficient to induce the movement. With amplitudes of ±400 µA or higher the movement was stronger than before, which was additionally reflected in the electrical recordings.

4.10.2 Astroglial Ca^{2+} events after electrical stimulation of the spinal cord

The combination of electrical stimulation, recording and 2P-LSM was tested with biphasic stimulations with amplitudes of 0.5 mA and 2.5 mA (Figure 4.28). The high stimulation current to induce leg movement was necessary due to an imperfect placement of the electrodes onto the spinal cord. A train of 50 stimulation pulses was applied. Single pulse stimulation did not provoke Ca^{2+} signals. During the electrical stimulation a movement artefact became visible, which was represented by a sharp negative peak in the mean image intensity as well as in the result of image correlation (Figure 4.28D, E). In addition, a change in the electrical recording was visible when the movement was initiated. The raise of the astrocytic Ca^{2+} signals started 1 s to 1.5 s and the peak value was visible at 4.5 s to 6 s after end of stimulation. With ongoing stimulations the base mean fluorescent intensity and the amplitude of Ca^{2+} events decreased. With a stimulation pause or with a stimulation amplitude which did not activate afferent or efferent fibres a slow increase in the Ca^{2+} signals was visible.

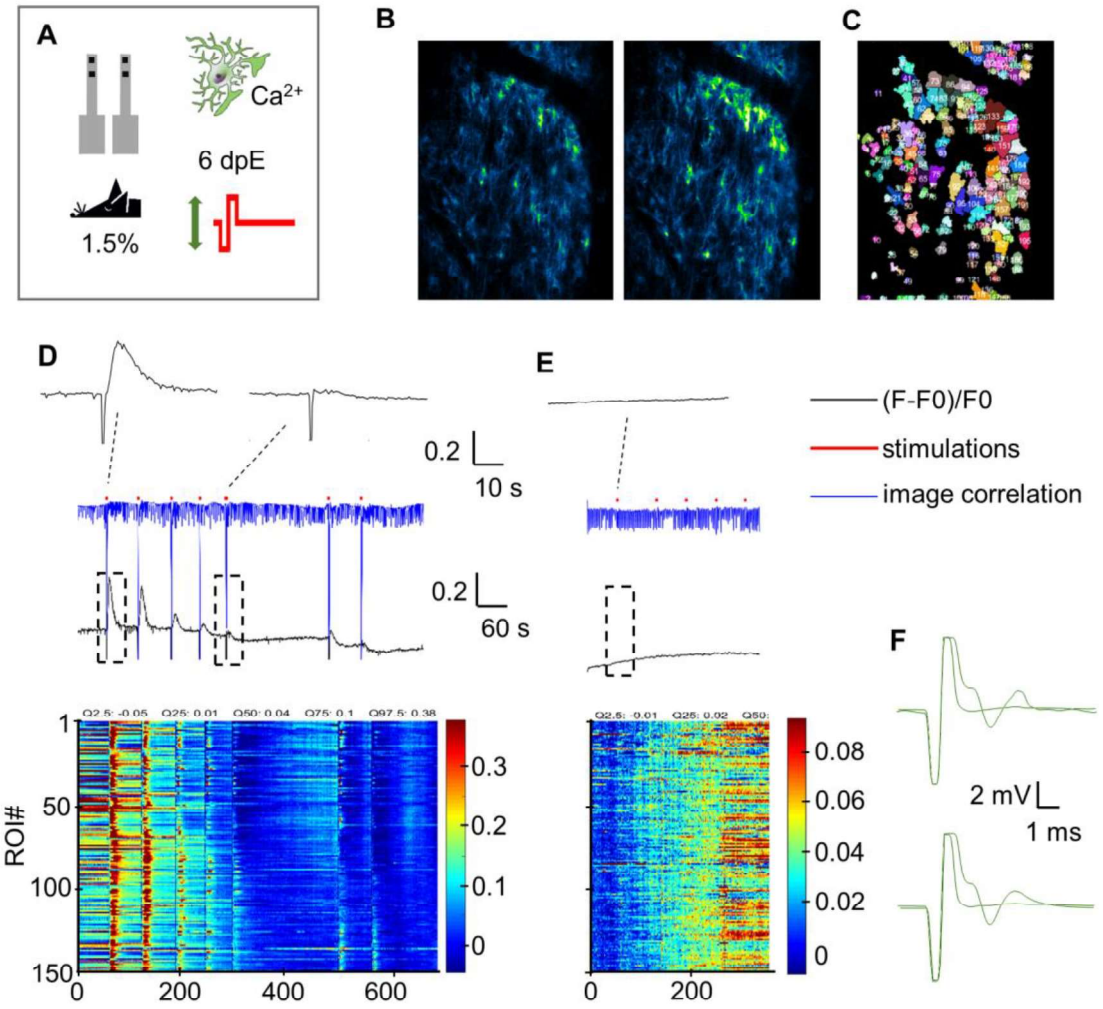

Figure 4.28: Spinal astrocytic Ca^{2+} events after electrical stimulation. A) Study set-up. Two spinal surface electrodes were applied to a GFAP-CreERT2 xRosa26-CAG-lsl-GCaMP3 mouse. The caudal electrode was used for electrical stimulation, the cranial electrode for recording of the electroneurogram. Recording device: PowerLab system; sampling rate: 40 kS/s; 50 Hz notch filter was activated. The mouse was anaesthetized using 1.5 % isoflurane. Biphasic stimulation trains with 0.5 mA and 2.5 mA; pulse width 500 µs, 50 pulses. 2P-LSM with 2 Hz frame rate. B) left: two-photon image prior a stimulation; right: two-photon image with peak Ca^{2+} signal after stimulation. C) ROI-detection of MSparkles. Stimulations with 2.5 mA (D) and subsequent stimulation with 0.5 mA (E). Red dots: stimulation periods; black line: mean image fluorescence intensity; blue line: image correlation result; heat maps: mean fluorescence intensity of 150 region of interests (ROI). F) Electroneurogram of first (top) and fifth (bottom) stimulation for both stimulation amplitudes.

5 Discussion

In this work, electrical stimulation and electrical recordings were combined with *in vivo* two-photon laser scanning microscopy (2P-LSM) in the murine central nervous system (CNS). A set of multichannel electrode arrays including the final assembly and application procedures for use in standard craniotomies and laminectomies were developed. Several pilot studies demonstrated the electrode biocompatibility at the cellular level and *in vivo* experiments showed their usability to investigate brain functions.

5.1 Electrochemical improvement of the surface electrodes

In order to improve the electrochemical properties of the liquid crystal polymer (LCP) electrodes, an electroplating system for platinum electroplating was built and various electroplating parameters were tested (Chapter 3.2). The use of ultrasound was essential during the electroplating process to apply a complete platinum layer to the electrodes. In the literature, an improvement of the coatings by ultrasound has been described, e.g. to remove loose particles (Boretius et al., 2011) or to avoid cracking due to internal material stress (Ohsaka et al., 2008). For the LCP electrodes, gas bubble formation by electrolysis on the electrode surface was the reason for incomplete coatings.

Constant current electroplating was performed with current densities of 0.1 kA/cm^2 – 0.4 kA/cm^2. The best result was found at a current density of 0.2 kA/m^2

and an electroplating time of 75 s. At this time, the highest porosity for the electrodes seemed to be found due to the best crystal nucleation, which generally resulted in the lowest electrode impedance and the highest CSC_C. On the one hand, the time factor was apparently decisive for whether the electrode was completely coated, which was not necessarily the case with very short times. On the other hand, the rough structures of the gold electrode were probably smoothed by the platinum layer if the plating times were too long.

A similar result was achieved with pulse electroplating. For one current density (0.3 kA/m^2), the optimization was best and the values were lower to those of constant current electroplating (round-shaped electrode sites: |Z(f=10 Hz)| =32 kΩ - 52 kΩ as best for constant current; |Z(f=10 Hz)| =29 kΩ - 50 kΩ as best for pulsed current (mean value ± standard deviation)). For the tested parameters, however, no time dependence and a lower dependence on the current density were recognizable. This could be due to the fact that pulse electroplating produces different nucleation and plating rates within one pulse and thus inhomogeneous surfaces. The electroplating parameter with pulsed current could generated similar results for the round-shaped electrode sites to the rectangular-shaped sites (magnitude of impedance multiplied with site area for current density of 0.3 kA/m^2 and 90 current pulses: 0.54 kΩmm^2 to 0.9 kΩmm^2 for the round-shaped electrode sites and 0.48 kΩmm^2 to 0.68 kAmm^2 for the rectangular-shaped electrode sites. Thus, the method showed a good robustness for the different electrode site sizes.

The variations in electroplating results per condition have most likely two reasons. On the one hand, the impedance values of the gold electrode sides have manufacturing variations (round shaped electrodes: |Z(f=10 Hz)| =3.3 MΩ – 7.2 MΩ; rectangular-shaped electrodes: |Z(f=10 Hz)| =0.5 MΩ – 1.1 MΩ). On the other hand, the temperature of the plating solution changed over time due to the internal ultrasonic module (see Appendix, Chapter 8.9). To minimize the influence, the basin and the plating solution were exchanged after four or eight plating processes, but a small temperature influence could not be prevented. An external ultrasound module could solve this problem and could allow further studies with an accurate temperature control.

5.2 LCP surface electrodes are biocompatible

Minimizing the effects of the electrode on the tissue was a crucial point for the investigation of cell functions or the complex network interaction. Therefore, the concept with surface electrodes was selected and the biocompatibility could be successful demonstrated.

5.2.1 No detection of cellular reactions or morphological changes after electrode implantation

In contrast to the reported tissue response in rodents to intracortical electrodes (Minnikanti et al., 2010; Potter et al., 2012; Salatino et al., 2017), no information was obtained about the tissue response to epidural electrodes (Chapter 4.4). Consequently, in this work the biocompatibility on the cellular level was tested in a short-term (three days post electrode surgery) as well as in a long-term (28 days post electrode surgery) experiment. The three-day condition was selected because this was the minimum recovery time for mice in chronic experiments. In contrast to intracortical electrodes, no continuous inflammation process or scar tissue generation were caused by the LCP surface electrodes. This makes it possible to examine physiological or pathological tissue.

In general, the prevention of tissue damage began with the surgery. During cortical application, the skull had to be carefully opened and the tissue was protected from desiccation. The design of the electrode arrays with a separated connection wire for a ground or reference electrode supported a simple and fast application. The standard craniotomy procedure could be used, and only had to be completed with an intermediate step from opening the skull to closing it with a cover glass. The electrode was safely placed within two minutes so that no tissue damage was observed during this step. The platinum wire (ground electrode) was placed beforehand and the connection to the electrode was done after making the craniotomy (Chapter 4.3.1). The thickness of approximately 75 µm of the LCP electrodes, which were considerably thicker than other electrodes made from polyimide or Parylene C (overall thickness less than 10 µm possible; Donahue et al., 2018; Ledochowitsch et al., 2011), had no consequences in application. However, the LCP electrodes were still thinner than the skull of the mouse and thus had enough space between the cortical

tissue and the cover slip. The electrodes did not push the cortical tissue down in a non-anatomical way.

A laminectomy itself was more complicated than a craniotomy, as more single steps were required. The opening was larger, the spine has to be intensively cleaned, and the vertebra has to be stabilized. For electrode application, silicone was used to fill the space between the applied electrodes, spine, and the cover slip. But also in this case the electrodes could be applied without any problems due to the robust technology. A future improvement might be the use of a special holder to support the fixation of the electrode connector, which was glued to the skin.

5.2.2 Angiogenesis detection indicated no inflammation-affected bone regrowth

A limiting factor of long-term studies has been bone regrowth (Chapter 4.5). And indeed, bone regrowth was observed via the angiogenesis as the first essential responder in healing processes in tissue or bone (Laschke et al., 2006; Claes et al., 2012). Since the mice of this study received dexamethasone in addition to the painkiller after the operation, the influence of this anti-inflammatory drug was analysed. No dependence between angiogenesis and dexamethasone was found. This supported the outcome from the immunohistochemistry, which showed no inflammation process. The differences in the growing speed and reorganisation of vessel formation, especially in the first week (vessels coverage on electrode head was about 0.7% - 10%), underlined individual variations and were mainly influenced by the quality of the surgery. A small bleeding could dramatically speed up the complex mechanism of angiogenesis, because with the blood angioblasts to start vessel formation could be transported (Lampri and Ioachim, 2013). Small bleedings could also occur after a craniotomy was made and the mouse was moving in the cage. It could hit the head holder against the cage, moving the brain tissue toward the bone edge created by the craniotomy.

A MATLAB script was created to analyse the angiogenesis (Chapter 3.4.2). The detection of the reddish vessels was based on a different grey-colour value to the white background. Because of the visibility of the interconnection lines and electrode sites, in an intermediate processing step a background image was calculated and subtracted from the original image. The median filtering in this step led to an error in

detection. The vessels looked slightly blurred, but this error seemed to be tolerable and should be similar across all images. An additional positive effect of this algorithm was to minimize the influence of blood spots during vessel formation, which were detected as background. Additional filter steps or a more intelligent recognition algorithm (self-learning neural networks) could probably improve the result and should be considered in the future.

5.3 Surface electrodes enabled electrical recordings of spontaneous und evoked potentials in the CNS

5.3.1 Physiological conditions and cuprizone induced-changes in VEPs could be identified

One reason for the recording of the neuronal activity from the cortex was to determine the physiological condition of the mouse during the experiments, because the stress level of the mouse was an unmeasurable but important factor. With both LCP surface electrode arrays (round-shaped and rectangular-shaped electrode sites), electrocorticograms (ECoGs) low-noise recordings were achieved by appropriate bandpass (0.5 Hz to 250 Hz) and notch filtering (50 Hz). Thus, it was possible to differentiate whether and how deep the mouse was under anaesthesia (Land et al., 2012) in acute and in chronic animal studies. However, more studies with ongoing data analysis are required to identify small ECoG changes, for example in case of inducing synaptic plasticity with electrical stimulation.

Visually evoked potentials (VEPs) were applied to cuprizone-fed and normal-fed mice. The signal form of the recorded VEP was similar to that from the literature for VEP recordings over the visual cortex or in layer 1 of the visual cortex (Ridder and Nusinowitz, 2006; Porciatti et al., 1999). A reduction in the signal energy of the VEPs might be observed for the cuprizone-fed mice. No difference in the amplitude of the first response was visible. The reason therefore could be that the signal transmission speed of the optic nerve and a first brain information processing was not noticeably changed. However, further processing within the complex neuronal network (Harris and Mrsic-Flogel, 2013; Thomson and Lamy, 2007) of the visual input might be

affected, which could lead to a change in the electrical response. For further clarification, the degree of demyelination of the optic nerve and cortical tissue has to be investigated by immunohistochemistry. Probably the myelin was not sufficiently reduced, either by the model itself or due to a regeneration effect resulting from the repeated visual stimulation.

5.3.2 Multichannel surface electrodes enabled the recording of cortical electrical network information

To design the electrode arrays, special attention was given to the size and the separation distance of the contact points. Only little information was available from previous studies. On one hand, the electrode sites are selected as small as possible down to the 10 µm range in order to be able to detect the firing of individual neurons (Khodagholy et al., 2015). On the other, the electrode arrays with larger electrode sites were used to acquire more global activities and to analyse which cortical areas were active, for example using the current density analysis (Buzsáki et al., 2012). Thus, a channel similarity study (Chapter 4.6.1) was performed for the LCP electrodes by calculating the correlation of the individual channels. The result indicated that there was a high similarity between the channels in the awake as well as in the anaesthetized mouse. This should allow the determination of regional global activity within the observation window for further analysis. However, some signal differences were also found owing to the decreasing correlation results for more distant electrode sites. This indicated that very specific local signals were present and recordable with the electrode arrays. So far, there were no valuable starting points to combine the difference voltages of the channels for spontaneous signals with 2P-LSM. This might be different for sensory evoked potentials. For example, the propagation along the cortex (Mohajerani et al., 2013) could be followed and compared with functional 2P-LSM to gain deeper insights in the role of microcircuits across the different cell populations.

5.3.3 Spinal surface electrodes recorded somatosensory and electrically evoked potentials

The electrical recording of neural signals from the surface of the spinal cord was possible for somatosensory (hind paw pinch) and for electrically evoked potentials (Chapter 4.10). Electrical stimulation was performed with a second spinal surface electrode located closer to the tail. The signal difference of the electrically evoked potential (>150 µV) was at least five-fold higher than of the somatosensory evoked potential (20 µV to 30 µV). Thus, the electrical stimulation activated a higher number of fibres generating large combined action potentials.

During the activation of neuronal fibres i*n vivo* fibre, two different observations were made. With lower current amplitudes, the afferent fibres were activated, due to their closer position to the stimulation electrode. By increasing the stimulation amplitude, the signal of the electromyogram changed together with the appearance of a leg movement. The fastest nerve conduction velocity of the afferents was found at approximately 20 m/s. However, we cannot exclude that, due to the stimulation artefact, a fast component of the neural signal might have been obscured. Thus, it remained unclear if this was the response of the fastest fibres. In previous studies, fastest nerve conduction velocities have been reported in the range of 17 m/s to 28 m/s for anaesthetized mice depending on temperature of the spinal cord (Dibaj and Schomburg, 2017). In addition, the complex response of slower fibres with a conduction velocity in the range of 5.5 m/s to 3 m/s could be recorded. Unlikely as for the peripheral nerves (different fibre groups with conduction speeds ranging from approximately 1 m/s to 45 m/s; Steffens et al., 2012; Walsh et al., 2015), no detailed information were found for nerve conduction velocities of murine spinal fibres *in vivo* for comparison.

Measuring the electromyogram with needle electrodes has to be improved for future studies. The insertion of two needles in the small femoral muscle required a strong fixation, which impeded a physiological leg movement. In addition, long-term or repetitive experiments could lead to strong muscle damage. A non-invasive approach that allows physiological leg movements is preferable.

5.4 Successful combination of electrophysiology and 2P-LSM

With the new electrodes and head-holder, combined studies could be carried out. Owing to the higher border of the holder, sufficient amount of water could be filled in for laser coupling for long-lasting imaging studies. 2P-LSM was performed within the cortex at a depth of 50 µm - 200 µm to observe Ca^{2+} changes in neurons and astrocytes. Together with a maximum FOV size of 256 µm x 256 µm, the shadow effect of the electrode was not interfering. In addition to the use of MSparkles, semiautomatic MATLAB scripts for image and signal processing were developed, enabling a step-by-step analysis and verification of the acquired data.

5.4.1 LCP electrodes supported data analysis with spatial information

The high reflective surface of the LCP electrode was visible in the two-photon images (Chapter 4.1.1), even when the laser power was set to the lowest possible value (around 1%). This enabled a fast navigation to the optical window of the electrode. In addition, the identification of a prominent marker (the upper-left corner) made it possible to locate the FOV. With three corners of the electrode window, a complete coordination system could be generated to gain more knowledge about the orientation of the FOV to the electrode (Chapter 4.7). However, the verification of this method showed that the detection of the corners was affected by a certain error in the µm range. In relation to the edge length of the electrode window of at least 1 mm, the error seemed acceptable to determine the position and orientation of the FOV. The error in z-direction was much greater than in x- and y-direction because the image brightness was evaluated instead of aligning the electrode corner to a target cross. In addition to the individual subjective evaluation, the alignment was also influenced by the electrode orientation and thus by the different direction of the electrode reflection in combination with the corner (for example, the reflective surface for the upper left corner was on the left and top side and for lower right corner on the right bottom side).

5.4.2 Isoflurane and kainate could be used to alter cellular responses

To combine ECoG and 2P-LSM, a mirror control signal from the microscope was captured with the recording system. This made it possible to synchronize the different data frame by frame. Mice with the genetically encoded Ca^{2+} indicator GCaMP3 expressed in astrocytes were used in the combined imaging studies. Anaesthesia (isoflurane concentration) was altered or an injection of kainate into the contralateral hemisphere of the cortex was used to alter neuronal and astrocytic activity. Isoflurane increases the activity of $GABA_A$ receptors and potassium channels (Lissek at al., 2016), thereby reducing neuronal excitability. Kainate activates respective ion channels (AMPA as well as kainate-type glutamate receptors) located on presynaptic and postsynaptic terminals, dendrites, and axons (Lerma, 2003; Lerma and Marques, 2013) and thus has a considerable influence on the neuronal activity. It can induce seizures, change astrocytic signalling and acts as a model of temporal lope epilepsy (Bedner et al., 2015).

Using the electrode array, highly synchronized neuronal spiking activity could be detected in the contralateral hemisphere after kainate injection into the ipsilateral hemisphere. Under anaesthesia and after kainate injection, the ECoGs appeared to be similar for both synchronized spiking activities, but the correlation results reflected a higher synchronization for the kainate-changed neuronal activity. A variation in the number of Ca^{2+} events per time could be observed when the anaesthesia was altered. Approximately 0.05 Ca^{2+} events / s to 0.7 Ca^{2+} events / s in the anaesthetized and 2.5 Ca^{2+} events / s to 4 Ca^{2+} events / s in the awake mouse were detected. Previously a ten-fold reduction of spontaneous somatic signals were described for astrocytes when the mouse was anaesthetized (Thrane et al., 2012). The anaesthesia level was a crucial factor and could be monitored with the combined ECoG recordings. With a more comprehensive database the Ca^{2+}-events per time should be intensively compared with the depth of anaesthesia estimated via the ECoG (Land et al., 2012, Lissek et al., 2016). Together with a differentiation of astroglial Ca^{2+}-events in somata and processes our knowledge on the role of astrocytes for brain function will increase.

From a more general perspective, the astroglial Ca^{2+} signals were reduced when the neurons fire more synchronously. This effect could be observed after kainate injection, where less than 0.3 Ca^{2+} events / s were observed while the mouse was not under anaesthesia. When the ECoG indicated an epileptic seizure the astrocytic

activity raised at seizure end within few seconds to about 4 Ca^{2+} events / s and dropped back afterwards. So far, it is not clear if the astrocytes only following the general synaptic transmission and thereby the release of neurotransmitters (Volterra and Medolesi, 2005; Guerra-Gomes et al. 2018) or if they actively damp the neuronal activity. Thus, the multichannel recordings along the cortex and the knowledge about the neuronal synchrony might be a promising approach in different physiological and pathophysiological in vivo studies.

5.4.3 Axons rather than neuronal cell bodies were directly activated by electrical stimulation

The electrode arrays with the rectangular-shaped electrode sites were used for electrical stimulation of the cortical tissue. Stimulation experiments were performed with mice expressing the genetically encoded Ca^{2+} indicator GCaMP3 in neurons or in astrocytes. A direct stimulation response was visible from Ca^{2+} related signals in neurons, which changed with stimulation amplitude, stimulation frequency, and anaesthesia. However, the threshold of network activation changed with the time between electrode application and stimulation study. The reason was the bone regrowth under the electrode, resulting in a different current distribution between the electrode sites. For this reason, the threshold value was determined before each experiment. By using two interconnected electrodes, the minimum stimulation current was about 150 µA for studies performed three days after electrode surgery. This resulted in a calculated current density of about 950 µA/mm^2 at the electrode surface, which should enable the stimulation of the axonal structure (Tehovnik et al., 2006). With the geometric information about the FOV, calculated by the electrode edges, the Ca^{2+} spreading direction of neuronal transmission could be aligned to the 3D cellular structure. Prominent was the direction from the cortical surface down to deeper cortical layers. Thus, the electrical stimulation activated directly the axons in cortical layer 1.

The response of the neuronal network increased with increasing stimulation amplitude and decreasing anaesthesia because of a wider range of axonal excitation and a higher neurotransmitter release at the synapses. Using a frequency of 50 Hz, a stable neuronal activation could be observed in repeated electrical stimulation.

Changing the frequency to 10 Hz, the stimulation did not provoke stable responses. The Ca^{2+} related signal decreased in case of stimulations with the same amplitude. This might be an effect of short-term depression, a form of synaptic plasticity, due to the low density of long-lasting train stimulations (Citri and Malenka, 2008).

5.4.4 Cortical stimulation activated frequency-dependent local and global network activity

The observation of the spreading direction of the neuronal Ca^{2+} related signals was more advantageous with a 10 Hz stimulation, but to avoid the change of the neuronal network response, 50 Hz stimulation had to be used. In addition, with stimulations at 50 Hz two Ca^{2+} transients became clearly visible. The first came mainly from the activation of the neuropil and the second mainly from the activation of the somas (Figure 4.21). After the raise of the somatic Ca^{2+} signals a drop (within the imaging speed) was observed while the stimulation was still active. This might be an effect of activated Ca^{2+} pumps restoring the intracellular Ca^{2+} homeostasis.

In addition, a fast (within imaging speed) and a slow decrease (about 5 s) was visible in somatic Ca^{2+} related signals for 50 Hz stimulation when the stimulation was about 10 s. The fast reduction might be induced by Ca^{2+} pumps as it was probably seen in the neuropil. However, the slow signal change could be an effect of the global network activity, because a similar effect was described in a recent published study (Michelson et al., 2018). A 16-channel silicon single-shank electrode was used to activate small populations of neurons and to investigate the response of *in vivo* Ca^{2+} signals (GCaMP6) in cortical layer 2/3 with two-photon imaging to different stimulation frequencies from 10 Hz to 250 Hz. The stimulation amplitude was set to 50 µA and a pulse width of 50 µs was used (Michelson et al., 2018). In these experiments, the stimulation time was 30 s, followed by a pause of 90 s. The highest activation and the largest activity spread were found for stimulation frequencies of 30 Hz and 50 Hz (Michelson et al., 2018). In this study, also a decrease in Ca^{2+} signals could be observed after a few seconds of stimulation for neurons with a distance of 115 µm. This effect was not visible in the neurons next to the stimulation electrode. It was pointed out that an explanation can only be found if the functionality of the complex neuronal and non-neuronal (glial) network will be investigated

(Michelson et al., 2018). Incidentally, this study has also indirectly addressed the problems with implantable electrodes. The tissue responded directly to electrode implantation, resulting in mechanical stress-related Ca^{2+} signals.

Unlike this work, the study (Michelson et al., 2018) provided no visual information or description of a signal undershoot within a period of about 35 s to 70 s after stimulation. However, the pause of 90 s between the single stimulation could be an indication that some time was required restoring a base situation. The dependence to the level of anaesthesia might be an indication that this was a combined effect resulting from active Ca^{2+} pumps and synaptic transmission opening Ca^{2+} channels (Nowycky and Thomas, 2002). Thus, the interaction of reducing Ca^{2+} and increasing Ca^{2+} could be a combined effect of the activity of single neurons, neuronal network and astrocytes.

In another combined *in vivo* stimulation study (Histed et al., 2009), using needle electrodes made of tungsten or platinum-iridium or a glass pipette, no of these effects were described. Short train stimulations at a frequency of 250 Hz were performed with a selected stimulation amplitude close to the identified stimulation thresholds (up to 25 µA). In the acute *in vivo* experiments, a Ca^{2+} increase in few neurons around the electrode tip and the neuropil within a radius of approximately 40 µm was observed (Histed et al., 2009). Both studies (Michelson et al., 2018; Histed et al., 2009) in combination indicate, that by observing neurons more distantly from the stimulation site and using ‘long-lasting’ stimulations might an additional approach to investigate the complex cortical network.

5.4.5 Astroglial Ca^{2+} events could be induced by electrical stimulation of neurons

To study astroglial Ca^{2+} responses after electrical stimulation, mice with GCaMP3 expression in astrocytes were used. The stimulation amplitude, stimulation frequency, and anaesthesia were changed. No astrocytic responses were visible for 10 Hz stimulation, even the stimulation amplitude was selected in the range which was known to safely activate the neuronal network. With higher frequencies of 30 Hz and 50 Hz, a measurable activation was possible. According to the timing of the astrocytic

response, the astroglial activation (50 Hz stimulation: peak value after 4 s to 5 s) was followed the neuronal activation (50 Hz stimulation: peak value after approximately 2 s). Thereby, they responded to the release of neurotransmitters (Volterra and Meldolesi, 2005; Shigetomi et al., 2016; Guerra-Gomes et al., 2018).

In contrast to the electrically evoked Ca^{2+} signals in neurons, the stimulated Ca^{2+} signals in astrocytes did not clearly change gradually with the change in anaesthesia or stimulation amplitude. One reason for this could be that the astrocytes were more restricted in their regional extent (Volterra and Meldolesi, 2005) than neurons and that astrocytes react to the integrated synaptic activity (Guerra-Gomes et al., 2018). Thus, the stimulation frequency might have a greater influence on astrocyte activity than the stimulation amplitude, which could be an explanation for the missing Ca^{2+} transients in 10 Hz and partly in 50 Hz stimulations. The astrocytes appeared to react at a threshold value as it might have been detected after kainate injection. However, the Ca^{2+} signals in astrocytes and in neurons after electrical stimulation have to be further investigated for a comprehensive understanding.

In addition to the cortical application, electrical stimulation and 2P-LSM was performed in the spinal cord *in vivo*. However, it had been more difficult to induce astroglial Ca^{2+} signals in the spinal cord than in the cortex by electrical stimulation of the neurons. In one of five studies an activation of the astrocytes, which was clearly related to the electrical stimulation, was possible. The Ca^{2+} signal decreased with the stimulation series and did not recover to a normal activity level within several minutes, which made it more difficult to identify Ca^{2+} events. In this individual experiment a higher stimulation current to stimulate the spinal cord was necessary due to an imperfect placement of the electrodes. However, this could lead to an increased spinal area of neuronal stimulation. In literature, *in vivo* astroglial Ca^{2+} related signals in the dorsal horn of the anaesthetized mouse were only found after noxious stimulation of the hind foot by intraplantar formalin injection (Yoshihara et al., 2018). Paw pinching or brushing did not provoke Ca^{2+} events (Yoshihara et al., 2018). In addition, tail pinching did not increase astroglial Ca^{2+} related signals if the mouse was anaesthetized (Sekiguchi et. al., 2016). However, strong tail pinching could induce astrocytic activity when the mouse was awake (Sekiguchi et. al., 2016). In combination with our findings, astrocytic Ca^{2+} waves only arouse if intensive neuronal stimulation were performed. In future studies, mice with expressing Ca^{2+} fluorophore in neurons might be used. Identification of the volume of active electrical stimulation could help to generate and understand Ca^{2+} transients in astrocytes.

5.4.6 Boundaries for cortical surface electrodes

With the development of the LCP electrodes, different technical limitation had to be considered, resulting in some restrictions for use. These included the active integration of a window for the 2P-LSM and technical limitations in the miniaturization of the electrode.

The technology of a thin, flexible, and transparent surface electrode with 16 channels - based on parylene C with graphene electrode sides and interconnections - was introduced for recording and stimulation application (Park et al., 2014; Park et al., 2018). Fluorescent imaging was done at the cortical surface with one-photon excitation (UV light) over a cortex area of 4.6 x 3.4 mm^2 so that the entire electrode was visible. It was pointed out that the transparency was over 90% (Park et al., 2014). This made it possible to acquire Ca^{2+} signals directly at the electrode sites (Park et al., 2018). A comparison to a parylene C electrode with platinum electrode sites was shown. The metal structure blocked the visual access, but the electrode impedance (|Z(f=10Hz)| ≈ 8 MΩ, 200 µm in diameter) was at least one-order smaller than the impedance of the graphene electrodes (|Z(f=10Hz)| ≈ 100 MΩ, 200 µm in diameter; Park et al., 2018). The platinum electrode sites of this work showed an impedance in the range of |Z10Hz| ≈ 30 kΩ to |Z10Hz| ≈ 40 kΩ for an electrode diameter of 150 µm.

For stimulation with graphene electrodes (electrode site diameter of 150 µm), stimulation currents of 50 µA to 150 µA in train stimulation with a frequency of 150 Hz applied for 650 ms (around 100 pulses, pulse width: 205 µs) were used. However, stimulation currents of 150 µA resulted in total electrode failures (Park et al., 2018). The peak in Ca^{2+} signals and the widest, almost concentric, lateral spread of activation, which was approximately 600 µm, were found after a time of approximately 200 ms (Park et al., 2018). However, considering bone regrowth, higher currents would be required as it is currently possible to drive with this type of electrode.

Another recent study (Donahue et al., 2018) pointed out the result of the combination of an electrode array made from Parylene C (thickness approximately 4 µm) and gold interconnections (thickness approximately 100 nm) with two-photon imaging. The square electrode sites had a size of 25 µm x 25 µm, and the width of the interconnection lines was around 20 µm at the electrode head (Donahue et al., 2018). The routing of the interconnection line was selected in a way that the visual access through inner area of the electrode head was maximized. With that design,

heating and photoelectric effects were minimized (Donahue et al., 2018). However, this reflects the problem that metal structures within the optical field generate heat as a result of laser light adsorption. This might also be the reason why the imaging was mainly performed between the electrode sites (electrode spacing 400 µm; Donahue et al., 2018) and not around an electrode site.

Currently, there does not seem to be any electrode technology that can be used without restrictions. With the high-level microsystem-produced electrodes, a high degree of miniaturization and improved flexibility would be possible. However, a global transparency could be only generated if the electrode contacts were also realized with transparent conductive materials. But, these materials still seem to have deficits in electrode impedance and current transfer capability.

6 Conclusion and outlook

Within this work reliable and cost-effective liquid crystal polymer surface electrodes have been developed, allowing the combination of two-photon imaging and electrophysiology in the murine CNS *in vivo*. Various helpful set-ups and tools were created to prepare the individual studies and data analysis. The pilot studies highlighted the biocompatibility and the new opportunities provided by the technology. It has been shown that the complexity of the cortical and spinal cellular network needs to be investigated with the combination of different methods. This is important to understand diseases of the CNS and to develop suitable treatments. Therefore, the novel technology is one important step in this direction.

Astroglial signalling in the cortex after kainate injection has to be further investigated and supplemented with Ca^{2+}-imaging in neurons within this model. The multichannel recording of the electrical activity might be helpful in identification of global network synchrony, which probably was an important factor affecting the number of astroglial Ca^{2+} events. The results of the cortical electrical stimulation by observing the different network activities of neurons and astrocytes displayed complex interactions. Induced synaptic plasticity as a local regulation mechanism, or the Ca^{2+} signal suppression in neurons as potential part of a global regulations strategy complemented with astroglial Ca^{2+} events are of considerable interest. So far, the complex underlying mechanism of Ca^{2+} signals in spinal astrocytes have not been identified. Electrical stimulation and recording with the LCP electrodes was possible and thus could help to generate a better understanding. The combination of cortical and spinal electrodes in one mouse could gain additional information about the information transfer and processing of the entire CNS. Depending on the placement of the cortical electrode, sensory information could be recorded or movement could be electrically induced.

7 References

1. Adkins DL (2015) Cortical Stimulation-Induced Structural Plasticity and Functional Recovery after Brain Damage. In: Kobeissy FH, editor. Brain Neurotrauma: Molecular, Neuropsychological, and Rehabilitation Aspects. Boca Raton (FL): CRC Press/Taylor & Francis; Chapter 43
2. Allen Mouse Brain Atlas: Lein, E.S. et al. (2007) Genome-wide atlas of gene expression in the adult mouse brain, Nature 445: 168-176.
3. Akerboom J, Chen TW, Wardill TJ, Tian L, Marvin JS, Mutlu S, Calderón NC, Esposti F, Borghuis BG, Sun XR, Gordus A, Orger MB, Portugues R, Engert F, Macklin JJ, Filosa A, Aggarwal A, Kerr RA, Takagi R, Kracun S, Shigetomi E, Khakh BS, Baier H, Lagnado L, Wang SS, Bargmann CI, Kimmel BE, Jayaraman V, Svoboda K, Kim DS, Schreiter ER, Looger LL (2012) Optimization of a GCaMP calcium indicator for neural activity imaging. J Neurosci. Oct 3;32(40):13819-40
4. Basser PJ, Roth BJ (2000) New currents in electrical stimulation of excitable tissues. Annu Rev Biomed Eng; 2:377-97.
5. Bedner P, Dupper A, Hüttmann K, Müller J, Herde MK, Dublin P, Deshpande T, Schramm J, Häussler U, Haas CA, Henneberger C, Theis M, Steinhäuser C (2015) Astrocyte uncoupling as a cause of human temporal lobe epilepsy. Brain. May;138 (Pt 5):1208-22.
6. Beudel M, Brown P (2016) Adaptive deep brain stimulation in Parkinson's disease. Parkinsonism Relat Disord;22(Suppl 1):S123–S126
7. Bihler E, Hauer M, Bagen S (2017) Embedding of active Components in LCP for Implantable Medical Devices. Talk at 44th IMAPS New England Symposium. Presentation slides available at URL http://www.imapsne.org/virtualCDs/2017/2017%20presentations/D/D1.pdf. Last call at 22.08.2019.
8. Boretius T, Jurzinsky T, Koehler C, Kerzenmacher S, Hillebrecht H, Stieglitz T (2011) High-porous platinum electrodes for functional electrical stimulation. Conf Proc IEEE Eng Med Biol Soc. 2011:5404-7
9. Boehler C, Stieglitz T, Asplund M (2015) Nanostructured platinum grass enables superior impedance reduction for neural microelectrodes. Biomaterials. Oct; 67:346-53
10. Buzsáki G, Anastassiou CA, Koch C (2012) The origin of extracellular fields and currents — EEG, ECoG, LFP and spikes. Nature Reviews Neuroscience volume 13, pages 407–420
11. Chen and Holt-Hindle (2010) Platinum-Based Nanostructured Materials: Synthesis, Properties, and Applications. Chem. Rev, 110, 3767–3804

12. Claes L, Recknagel S, Ignatius A (2012) Fracture healing under healthy and inflammatory conditions. Nat Rev Rheumatol. 31;8(3):133-43.
13. Ciobanu M, Wilburn JP, Krim ML, Cliffel DE (2007) Fundamentals. In: Handbook of Electrochemistry. Editor: Zoski CG. Elsevier Science. ISBN: 978-0-444-51958-0
14. Citri, A., Malenka, R. (2008) Synaptic Plasticity: Multiple Forms, Functions, and Mechanisms. Neuropsychopharmacol 33, 18–41
15. Cupido A, Catalin B, Steffens H and Kirchhoff F (2014). Surgical procedures to study microglial motility in the brain and in the spinal cord by in vivo two-photon laser-scanning microcopy. In Confocal and Multiphoton Laser-Scanning Microscopy of Neuronal Tissue: Applications and Quantitative Image Analysis, ed. Bakota L & Brandt R, pp. 37-50. Springer.
16. Cogan SF (2008) Neural Stimulation and Recording Electrodes. Annu. Rev. Biomed. Eng. 10:275–309
17. Datta A, Baker JM, Bikson M, Fridriksson J (2011) Individualized model predicts brain current flow during transcranial direct-current stimulation treatment in responsive stroke patient. Brain Stimul. 2011 Jul;4(3):169-74
18. Defelipe J (2011) The evolution of the brain, the human nature of cortical circuits, and intellectual creativity. Front Neuroanat. 2011 May 16;5:29. doi: 10.3389/fnana.2011.00029. eCollection 2011.
19. Derdikman D, Knierim JJ (2014) Space, Time and Memory in the Hippocampal Formation. Springer, ISBN: 978-3-7091-1291-5
20. Dibaj P, Schomburg ED (2017) *In vivo* recording of nerve conduction velocity of spinal CNS fibers in the mouse. Physiol Res. 2017 Jul 18;66(3):545-548. Epub 2017 Feb 28
21. Donahue MJ, Kaszas A, Turi GF, Rózsa B, Slézia A, Vanzetta I, Katona G, Bernard C, Malliaras GG, Williamson A (2018) Multimodal Characterization of Neural Networks Using Highly Transparent Electrode Arrays. eNeuro. 2018 Jan 10;5(6). pii: ENEURO.0187-18.2018. doi: 10.1523/ENEURO.0187-18.2018. eCollection 2018 Nov-Dec.
22. Douglas RJ, Martin KA (2004) Neuronal circuits of the neocortex. Annu Rev Neurosci. 2004;27:419-51.
23. Du ZJ, Kolarcik CL, Kozai TDY, Luebben SD, Sapp SA, Zheng XS, Nabity JA, Cui XT (2017) Ultrasoft microwire neural electrodes improve chronic tissue integration. Acta Biomaterialia 53. 46–58
24. Evangelidis GD, Psarakis EZ (2008) Parametric Image Alignment Using Enhanced Correlation Coefficient Maximization. IEEE TRANSS ON PATTERN ANALYSIS AND MACHINE INTELLIGENCE, VOL. 30, NO. 10, 1858-1865
25. Fenrich KK, Weber P, Hocine M, Zalc M, Rougon G and Debarbieux F (2012) Long-term in vivo imaging of normal and pathological mouse spinal cord with subcellular resolution using implanted glass windows. J Physiol 590.16, 3665–3675
26. Fields RD, Burnstock G (2006) Purinergic signalling in neuron-glia interactions. Nat Rev Neurosci. 2006 Jun;7(6):423-36.
27. Franks W, Schenker I, Schmutz P, Hierlemann A (2005) Impedance Characterization and Modeling of Electrodes for Biomedical Applications. IEEE Transaction on Biomedical Engineering, Vol. 52, No 7
28. Geddes LA (1997) Historical Evolution of Circuit Models for the Electrode-Electrolyte Interface. Annals of Biomedical Engineering, Vol 25, pp1-14
29. GENSAT: "The Gene Expression Nervous System Atlas (GENSAT) Project, NINDS Contracts N01NS02331 & HHSN271200723701C to The Rockefeller University (New York, NY)." last call 20.05.2019
30. Guerra-Gomes, S. Sousa, N. Pinto, L. & Oliveira, J. F (2018) Functional Roles of Astrocyte Calcium Elevations: From Synapses to Behavior. Front Cell Neurosci 11:427.

31. Goebbels S, Bormuth I, Bode U, Hermanson O, Schwab MH, Nave KA (2006) Genetic Targeting of Principal Neurons in Neocortex and Hippocampus of NEX-Cre Mice. Genesis 44:611-621
32. Groothuis J, Ramsey NF, Ramakers GM, van der Plasse G (2014) Physiological challenges for intracortical electrodes. Brain Stimul. 2014 Jan-Feb;7(1):1-6.
33. Harris KD, Mrsic-Flogel TD (2013) Cortical connectivity and sensory coding. Nature. 2013 Nov 7;503(7474):51-8. doi: 10.1038/nature12654
34. Harris KD, Sheperd GMG (2015) The neocortical circuit: themes and variations. Nat Neurosci. 2015 February ; 18(2): 170–181. doi:10.1038/nn.3917
35. Helmchen F, Denk W (2005) Deep tissue two-photon microscopy. Nature Methods, 2(12):932-940
36. Hirrlinger PG, Scheller A, Braun C, Hirrlinger J, Kirchhoff F (2006) Temporal control of gene recombination in astrocytes by transgenic expression of the tamoxifen-inducible DNA recombinase variant CreERT2. Glia. Jul;54(1):11-20.
37. Histed MH, Bonin V, Reid R C (2009) Direct activation of sparse, distributed populations of cortical neurons by electrical microstimulation. Neuron. 2009 Aug 27; 63(4): 508–522. doi: 10.1016/j.neuron.2009.07.016
38. Jebelli J, Su W, Hopkins S, Pocock J, Garden GA (2015) Glia: guardians, gluttons, or guides for the maintenance of neuronal connectivity? Ann N Y Acad Sci. 2015 Sep;1351:1-10. doi: 10.1111/nyas.12711. Epub 2015 Mar 9
39. Kandel E R, Schwartz J H, Jessel T M (2000) Principles of Neural Science. Fourth Edition. McGraw-Hill. ISBN: 0-8385-7701-6
40. Kettenmann H, Kirchhoff F, Verkhratsky A (2013) Microglia: new roles for the synaptic stripper. Neuron. 2013 Jan 9;77(1):10-8. doi: 10.1016/j.neuron.2012.12.023.
41. Khodagholy D, Gelinas JN, Thesen T, Doyle W, Devinsky O, Malliaras GG, Buzsáki G (2015) NeuroGrid: recording action potentials from the surface of the brain. Nat Neurosci. 2015 Feb;18(2):310-5. doi: 10.1038/nn.3905. Epub 2014 Dec 22.
42. Kirsch DL, Nichols F. Cranial (2013) Electrotherapy Stimulation for Treatment of Anxiety, Depression, and Insomnia. Psychiatr Clin N Am 2013;36:169–76.
43. Kloke A, von Stetten F, Zengerle R, Kerzenmacher S (2011) Strategies for the fabrication of porous platinum electrodes. Adv Mater. Nov 16;23(43):4976-5008.
44. Kozai TDY, Jaquins-Gerstl AS, Vazquez AL, Michael AC, Cui XT (2016) Dexamethasone retrodialysis attenuates microglial response to implanted probes in vivo. Biomaterials. 2016 May;87:157-169.
45. Kumsa DW, Bhadra N, Hudak EM, Kelley SC, Untereker DF, Mortimer JT (2016) Electron transfer processes occurring on platinum neural stimulating electrodes: a tutorial on the i(Ve) profile. J. Neural Eng. 13
46. Lampri E, Ioachim E (2013) Angiogenesis: Something Old, Something New. In: Angiogenesis – Insights from a Systemic Overview. Ed. Santulli G. Nova Science Publisher. ISBN: 9781626181144
47. Land R, Engler G, Kral A, Engel AK (2012) Auditory Evoked Bursts in Mouse Visual Cortex during Isoflurane Anesthesia. PLoS ONE 7(11): e49855. doi:10.1371/journal.pone.0049855
48. Laschke MW, Harder Y, Amon M, Martin I, Farhadi J, Ring A, Torio-Padron N, Schramm R, Rücker M, Junker D, Häufel JM, Carvalho C, Heberer M, Germann G, Vollmar B, Menger MD (2006) Angiogenesis in tissue engineering: breathing life into constructed tissue substitutes. Tissue Eng. 12(8):2093-104.
49. Ledochowitsch P, Olivero E, Blanche T, Maharbiz MM (2011) A transparent µECoG array for simultaneous recording and optogenetic stimulation. Conf Proc IEEE Eng Med Biol Soc. 2011;2011:2937-40. doi: 10.1109/IEMBS.2011.6090808

50. Lee J H, Kim H, Kim J H, Lee S H (2016) Soft implantable microelectrodes for future medicine: prosthetics, neural signal recording and neuromodulation. Lab Chip, 2016, 16, 959
51. Lerma J (2003) Roles and rules of kainate receptors in synaptic transmission. Nat Rev Neurosci. 2003 Jun;4(6):481-95.
52. Lerma J, Marques JM (2013) Kainate Receptors in Health and Disease. Neuron. 2013 Oct 16;80(2):292-311.
53. Lissek T, Obenhaus HA, Ditzel DAW, Nagai T, Miyawaki A, Sprengel R and Hasan MT (2016) General Anesthetic Conditions Induce Network Synchrony and Disrupt Sensory Processing in the Cortex. Front. Cell. Neurosci. 10:64.
54. Martin JH (1991) The collective Electrical Behaviour of Cortical Neurons: The Electroencephalogramm and the Mechanism of Epilepsy. In Principles of Neural Science. Edited by Kandel, Schwarz, Jessell. 3rd Edition. ISBN 0-8385-8034-3
55. Merrill DR, Bikson M, Jefferys JGR (2005) Electrical stimulation of excitable tissue: design of efficacious and safe protocols. J Neurosci Methods 141:171-98.
56. Minnikanti S, Pereira MG, Jaraiedi S, Jackson K, Costa-Neto CM, Li Q, Peixoto N (2010) In vivo electrochemical characterization and inflammatory response of multiwalled carbon nanotube-based electrodes in rat hippocampus. J. Neural Eng. 7, doi:10.1088/1741-2560/7/1/016002
57. Mohajerani MH, Chan AW, Mohsenvand M, LeDue J, Liu R, McVea DA, Boyd JD, Wang YT, Reimers M, Murphy TH (2013) Spontaneous cortical activity alternates between motifs defined by regional axonal projections. Nat Neurosci. 2013 Oct;16(10):1426-35. doi: 10.1038/nn.3499. Epub 2013 Aug 25.
58. Mollazadeh M, Murari K, Cauwenberghs G, Thakor N. From spikes to EEG: Integrated multichannel and selective acquisition of neuropotentials. 30th Annual International Conference of the IEEE EMBC 2008.
59. Mori T, Tanaka K, Buffo A, Wurst W, Kühn R & Götz M (2006). Inducible gene deletion in astroglia and radial glia--a valuable tool for functional and lineage analysis. Glia 54, 21-34.
60. Najarian K, Splinter R (2012) Biomedical Signal and Image Processing. Second Edition, Taylor & Francis Inc; ISBN: 978-1439870334
61. Nimmerjahn A, Kirchhoff F, Helmchen F (2005) Resting microglial cells are highly dynamic surveillants of brain parenchyma in vivo. Science. 2005 May 27;308(5726):1314-8. Epub 2005 Apr 14.
62. Nowycky MC, Thomas AP (2002) Intracellular calcium signalling. Journal of Cell Science 115, 3715-3716
63. Ohsaka T, Isaka M, Hirano K, Ohishi T (2008) Effect of ultrasound sonication on electroplating of iridium. Ultrason Sonochem. 2008 Apr;15(4):283-8. doi: 10.1016/j.ultsonch.2007.11.002. Epub 2007 Nov 21.
64. Park DW, Schendel AA, Mikael S, Brodnick SK, Richner TJ, Ness JP, Hayat MR, Atry F, Frye ST, Pashaie R, Thongpang S, Ma Z, Williams JC (2014) Graphene-based carbon-layered electrode array technology for neural imaging and optogenetic applications. Nat Commun. 2014 Oct 20;5:5258. doi: 10.1038/ncomms6258.
65. Park DW, Ness JP, Brodnick SK, Esquibel C, Novello J, Atry F, Baek DH, Kim H, Bong J, Swanson KI, Suminski AJ, Otto KJ, Pashaie R, Williams JC, Ma Z (2018) Electrical Neural Stimulation and Simultaneous in Vivo Monitoring with Transparent Graphene Electrode Arrays Implanted in GCaMP6f Mice. ACS Nano. 2018 Jan 23;12(1):148-157. doi: 10.1021/acsnano.7b04321. Epub 2018 Jan 8.
66. Paukert M, Agarwal A, Cha J, Doze VA, Kang JU, Bergles DE (2014) Norepinephrine Controls Astroglial Responsiveness to Local Circuit Activity. Neuron 82, 1263–1270

67. Porciatti V, Pizzorusso T, Maffei L (1999) The visual physiology of the wild type mouse determined with pattern VEPs. Vision Research 39, 3071–3081
68. Potter KS, Buck AC, Self WK, Capadona JR (2012) Stab injury and device implantation within the brain results in inversely multiphasic neuroinflammatory and neurodegenerative responses. Neural Eng. 9.
69. Radman T, Ramos RL, Brumberg, JC, Bikson M. Role of Cortical Cell Type and Morphology in Sub- and Suprathreshold Uniform Electric Field Stimulation. Brain Stimul 2009;2:215-28.
70. Rattay F, Analysis of the Electrical Excitation of CNS Neurons. IEEE Transaction on Biomedical Engineering, Vol. 45, No. 6, 1998
71. Rattay F and Wenger C (2010) Which elements of the mammalian central nervous system are excited by low current stimulation with microelectrodes? Neuroscience. 170(2):399-407
72. Rattay F (2013) Research in Electrical Stimulation Fundamentals. Artif Organs. Dec;37(12):1023-6
73. Remington LA (2012). in Clinical Anatomy and Physiology of the Visual System (Third Edition), Elsevier. 978-1-4377-1926-0
74. Ricard C, Arroyo ED, He CX, Portera-Cailliau C, Lepousez G, Canepari M, Fiole D (2018) Two-photon probes for in vivo multicolor microscopy of the structure and signals of brain cells. Brain Struct Funct. 223(7):3011-3043
75. Ridder WH 3rd, Nusinowitz S (2006) The visual evoked potential in the mouse--origins and response characteristics. Vision Res. 46(6-7):902-13
76. Saab AS, Tzvetavona ID, Trevisiol A, Baltan S, Dibaj P, Kusch K, Möbius W, Goetze B, Jahn HM, Huang W, Steffens H, Schomburg ED, Pérez-Samartín A, Pérez-Cerdá F, Bakhtiari D, Matute C, Löwel S, Griesinger C, Hirrlinger J, Kirchhoff F, Nave KA (2016) Oligodendroglial NMDA Receptors Regulate Glucose Import and Axonal Energy Metabolism. Neuron Jul 6;91(1):119-32.
77. Salatino JW, Ludwig KA, Kozai TDY, Purcell EK (2017) Glial responses to implanted electrodes in the brain. Nature Biomedical Engineering VOL 1, 862–877.
78. Schüttler M, Doerge T, Wien SL, Becker S, Staiger A, Hanauer M, Kammer S, Stieglitz T (2005) Cytotoxicity of Platinum Black. Conf Proc International FES Society
79. Schüttler M (2007) Electrochemical Properties of Platinum Electrodes in Vitro: Comparison of Six Different Surface Qualities. Conf Proc IEEE Eng Med Biol Soc. 2007:186-9.
80. Sekiguchi KJ, Shekhtmeyster P, Merten K, Arena A, Cook D, Hoffman E, Ngo A, Nimmerjahn A (2016) Imaging large-scale cellular activity in spinal cord of freely behaving mice. Nat Commun. 2016 Apr 28;7:11450. doi: 10.1038/ncomms11450.
81. Shepard G M. (2004) Thy synaptic organization of the brain. Fifth Edition Oxford University Press. ISBN: 978-0-19-515965-1
82. Shigetomi E, Patel S, Khakh BS (2016) Probing the Complexities of Astrocyte Calcium Signaling. Trends Cell Biol. Apr; 26(4):300-312
83. Simons M and Nave KA (2015) Oligodendrocytes: Myelination and Axonal Support. Cold Spring Harb Perspect Biol doi: 10.1101/cshperspect.a020479
84. So PTC, Dong CY, Masters BR, Berland KM (2000) Two-Photon Excitation Fluorescence Microscopy. Annu. Rev. Biomed. Eng. 2000.02:399-429
85. Spataro L, Dilgen J, Retterer S, Spence AJ, Isaacson M, Turner JN (2005) Dexamethasone treatment reduces astroglia responses to inserted neuroprosthetic devices in rat neocortex. Exp Neurol.194(2):289-300
86. Steffens H, Dibaj P, Schomburg ED (2012) In vivo measurement of conduction velocities in afferent and efferent nerve fibre groups in mice. Physiol Res. 2012;61(2):203-14. Epub 2012 Jan 31

87. Stieglitz T (2004) Electrode Materials for Recording and Stimulation. In Neuroprotesthetics Theory and Practice; editors: Horch KW and Dhillon GS; ISBN 981-238-023-X
88. Suner S, Fellows MR, Vargas-Irwin C, Nakata GK, Donoghue JP (2005) Reliability of signals from a chronically implanted, silicon-based electrode array in non-human primate primary motor cortex. IEEE Trans Neural Syst Rehabil Eng. 2005 Dec;13(4):524-41
89. Szepesi Z, Manouchehrian O, Bachiller S, Deierborg T (2018) Bidirectional Microglia-Neuron Communication in Health and Disease. Front Cell Neurosci. 2018 Sep 27;12:323. doi: 10.3389/fncel.2018.00323. eCollection 2018.
90. Szostak KM, Grand L, Constandinou TG (2017) Neural Interfaces for Intracortical Recording: Requirements, Fabrication Methods, and Characteristics. Front Neurosci. 2017 Dec 7;11:665. doi: 10.3389/fnins.2017.00665. eCollection 2017
91. Tan Z, Sun W, Chen TW, Kim D, Ji N (2015) Neuronal Representation of Ultraviolet Visual Stimuli in Mouse Primary Visual Cortex. Sci Rep. 2015 Jul 29; 5:12597
92. Tehovnik EJ, Tolias AS, Sultan F, Slocum WM, Logothetis NK (2006) Direct and Indirect Activation of Cortical Neurons by Electrical Microstimulation. J Neurophysiol 96: 512–521
93. Thomson AM, Lamy C (2007) Functional maps of neocortical local circuitry. Front Neurosci. 2007 Oct 15;1(1):19-42. doi: 10.3389/neuro.01.1.1.002.2007. eCollection 2007 Nov.
94. Thrane AS, Rangroo Thrane V, Zeppenfeld D, Lou N, Xu Q, Nagelhus EA, Nedergaard M (2012) General anesthesia selectively disrupts astrocyte calcium signaling in the awake mouse cortex. Proc Natl Acad Sci U S A. 2012 Nov 13;109(46):18974-9.
95. Tian L, Hires SA, Mao T, Huber D, Chiappe ME, Chalasani SH, Petreanu L, Akerboom J, McKinney SA, Schreiter ER, Bargmann CI, Jayaraman V, Svoboda K, Looger LL (2009) Imaging neural activity in worms, flies and mice with improved GCaMP calcium indicators. Nat Methods. Dec;6(12):875-81
96. Tomassy GS, Dershowitz LB, Arlotta P (2015) Diversity Matters: A Revised Guide to Myelination. Trends Cell Biol. Feb;26(2):135-147. doi: 10.1016/j.tcb.2015.09.002. Epub 2015 Oct 3.
97. Tsuei TW, Henderson RH, Massoud HZ (1991) Optimum Preparation And Storage Of Ag/Cl And Pt Black Microelectrodes For Transmural Cardiac Recording Applications. Conf Proc. IEEE EMBS; Volume 13, 1585-86
98. Volterra A and Meldolesi J (2005) Astrocytes, from brain glue to communication elements: the revolution continues. Nature Reviews, vol. 6, no. 8, pp. 626–640, 2005.
99. Walsh ME, Sloane LB, Fischer KE, Austad SN, Richardson A, Van Remmen H (2015) Use of Nerve Conduction Velocity to Assess Peripheral Nerve Health in Aging Mice. J Gerontol A Biol Sci Med Sci, 2015, Vol. 70, No. 11, 1312–1319
100. Wang B, Petrossians A, Weiland JD (2014) Reduction of Edge Effect on Disk Electrodes by Optimized Current Waveform. IEEE Trans Biomed Eng. 2014 August ; 61(8)
101. Watson C, Paxinos G, Puelles L (2012). The mouse central nervous system. Elsevier. ISBN: 978-0-12-369497-3
102. Winter SM, Hirrlinger J, Kirchhoff F, Hülsmann S (2007) Transgenic expression of fluorescent proteins in respiratory neurons. Respir Physiol Neurobiol. Oct 15; 159(1):108-14. Epub 2007 May 21.
103. Xu Y and Zhang B (2014) Recent advances in porous Pt-based nanostructures: synthesis and electrochemical applications. Chem. Soc. Rev.; 43, 2439—2450
104. Yang G, Pan F, Parkhurst CN, Grutzendler J, Gan W-B (2010) Thinned-skull cranial window technique for long-term imaging of the cortex in live mice. Nat Protoc. 2010 Feb; 5(2): 201–208.

105. Yazdan-Shahmorad A, Kipke DR, Lehmkuhle MJ (2013) High γ power in ECoG reflects cortical electrical stimulation effects on unit activity in layers V/VI. J Neural Eng. 2013 Dec;10(6):066002. doi: 10.1088/1741-2560/10/6/066002. Epub 2013 Oct 8.
106. Ye H, Steiger A. Neuron matters: electric activation of neuronal tissue is dependent on the interaction between the neuron and the electric field. J Neuroeng Rehabil 2015;12:65.
107. Yoshihara K, Matsuda T, Kohro Y, Tozaki-Saitoh H, Inoue K, Tsuda M (2018) Astrocytic Ca^{2+} responses in the spinal dorsal horn by noxious stimuli to the skin. J Pharmacol Sci. 2018 May;137(1):101-104. doi: 10.1016/j.jphs.2018.04.007. Epub 2018 May 3.

8 Appendix

8.1 Standard procedure of immunohistochemistry

8.1.1 Whole body fixation with formaldehyde (FA)

Mice were anaesthetized with Ketamine/Xylazine 0.9% NaCl. The skin was incised in the caudal–rostral axis until the sternum. Subsequently, the abdomen and peritoneum was cut from medial to lateral and the diaphragm was severed longitudinally.

Through lateral severing of the thorax until the sternum, the pericardium can carefully be released from the peritoneum. By inserting a butterfly needle into the left ventricle the perfusion with 1x PBS was started by a peristaltic pump. Simultaneously, an incision of the superior vena cava allows the blood to drain off.

The colour change in the liver from red to pale yellow indicates the change of blood to the perfusion buffer. After perfusion with 15-20 ml PBS, the animals were perfused with 4 % FA in PBS. Fixation was considered complete after perfusion of 20-25 ml FA and when the liver and heart hardened. Subsequently, perfusion was stopped, the brain dissected and stored in a glass recipient filled with 4 % FA for post fixation overnight (4°C). The next day, FA was exchanged for PBS and the fixed brain was used for vibratome slicing.

8.1.2 Preparation of vibratome slices

The fixed brains were sliced into coronal sections of 40 µm thickness, in PBS, at a Leica VT1000S vibratome. These sections were collected in 48-well culture plates containing 1x PBS and were used for immunohistochemistry.

8.1.3 Antibody staining

Vibratome sections were incubated for 1 hour in blocking buffer (5 % HS, 0.3 % Triton X in 1 x PBS) at room temperature. Triton X-100 is employed for permeabilization of the sections for proper antibody diffusion. Horse serum (HS) minimizes unspecific antibody binding by occupying all available binding sites, only becoming available to bind for antibodies with high affinity which thereby displace the HS. Sections were first incubated with GFAP-anti-mouse primary antibody, diluted in the blocking solution for 48 h at 4 °C. Afterwards the sections were incubated overnight with the complete primary antibody mix at 4°C. In the following, slices were washed 3 times for 10 min each in 1x PBS in order to remove any excess or non-specifically bound (low affinity) antibodies. Secondary antibodies were diluted in blocking buffer and incubated for 2 h at room temperature in the dark. Optionally, DAPI was added to the secondary antibody solution. Afterwards, the sections were washed 3 times with 1x PBS for 10 min to remove any non-specifically bound antibody. Finally, sections were placed in a water bath and mounted in Aqua poly mount (Polysciences). The analysis was performed at the AxioScanZ.1 slide scanner (Zeiss Jena, Germany).

8.2 Block diagram 2P-LSM

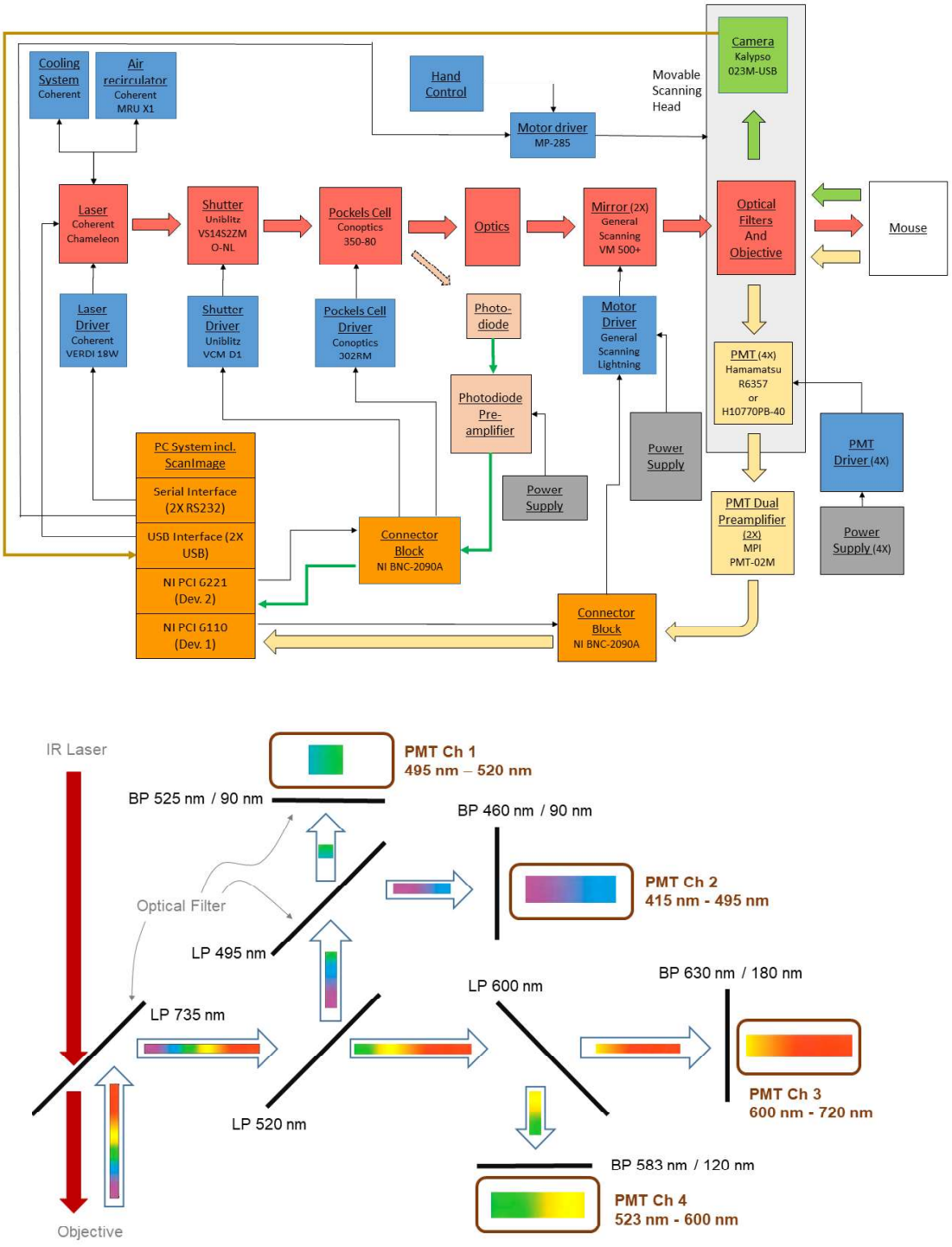

Figure 8.1: Block diagram of the 2P-LSM (top) and filter settings to split the four channels (below).

8.3 Estimation of median filter size

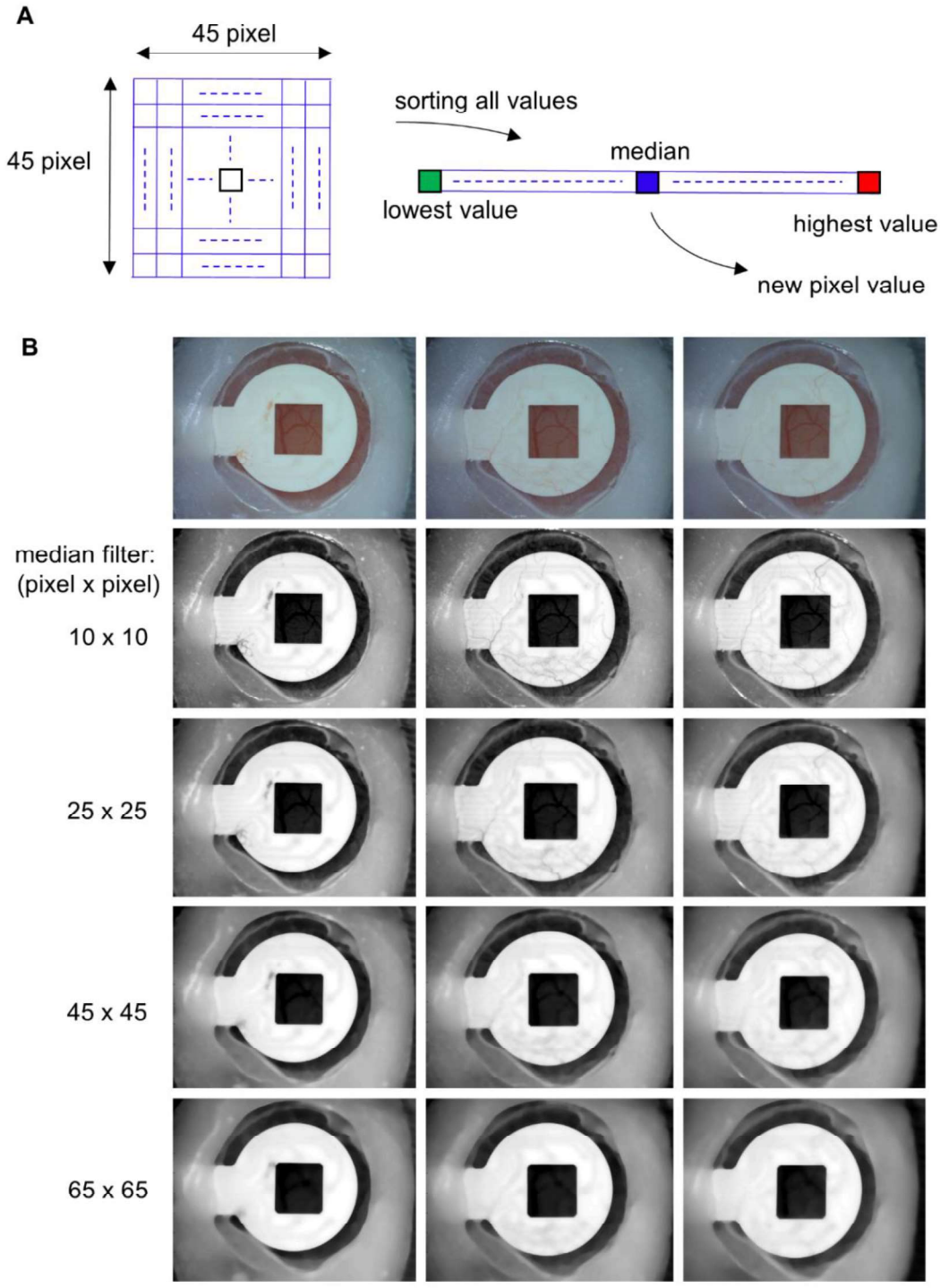

Figure 8.2: Median Filtering. A) Median filter array (left) is used to select pixel values around and including a centre pixel. These values are sorted and the value and the median is taken as new pixel value for the filtered image. B). Overview of different background images in dependence of median filter size. The median filter with size close to the double of the interconnection line width (45 pixel x 2.2 µm/pixel) provided the best ratio (subjective) of blood vessel suppression and interconnection visibility.

8.4 Recording device

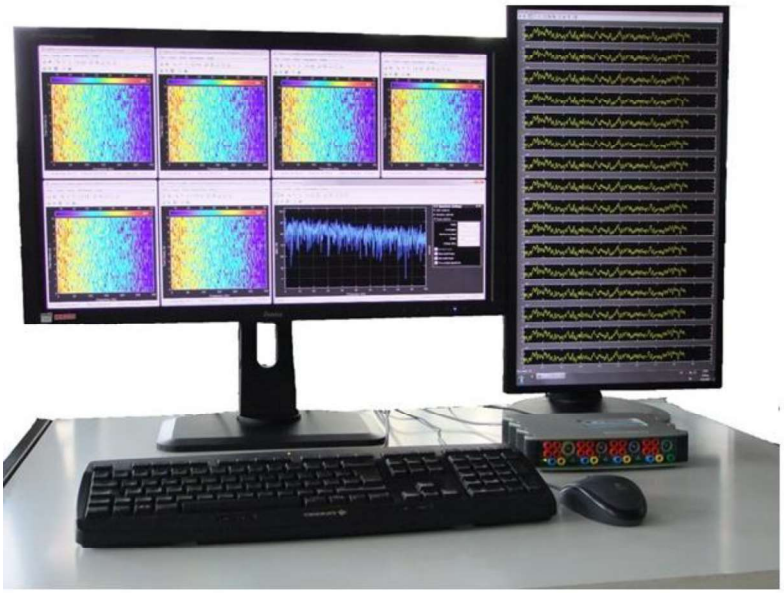

Figure 8.3: 16 channel recording system consisting of the recording device g.USBamp, Fa. g.tec and a self-developed software showing sixteen time traces, six time-frequency plots and one spectrum plot.

8.5 Estimation of VEP parameters

8.5.1 Minimum light intensity

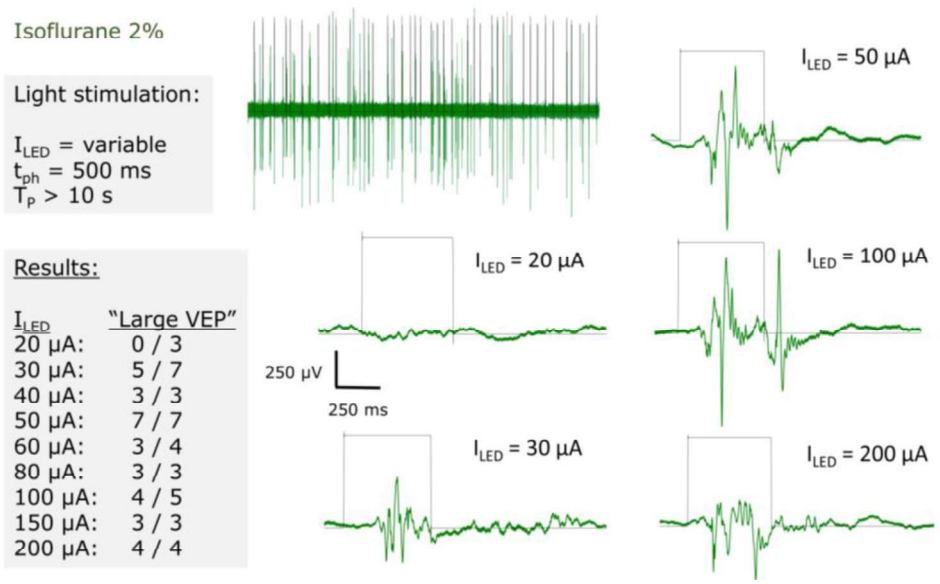

Figure 8.4: Estimation of the minimum LED current to evoke VEPs for a mouse under anaesthesia. If the VEP was evoked, the mouse reacted with a large neuronal response. The number of responses was counted (box Results).

8.5.2 Minimum pulse width

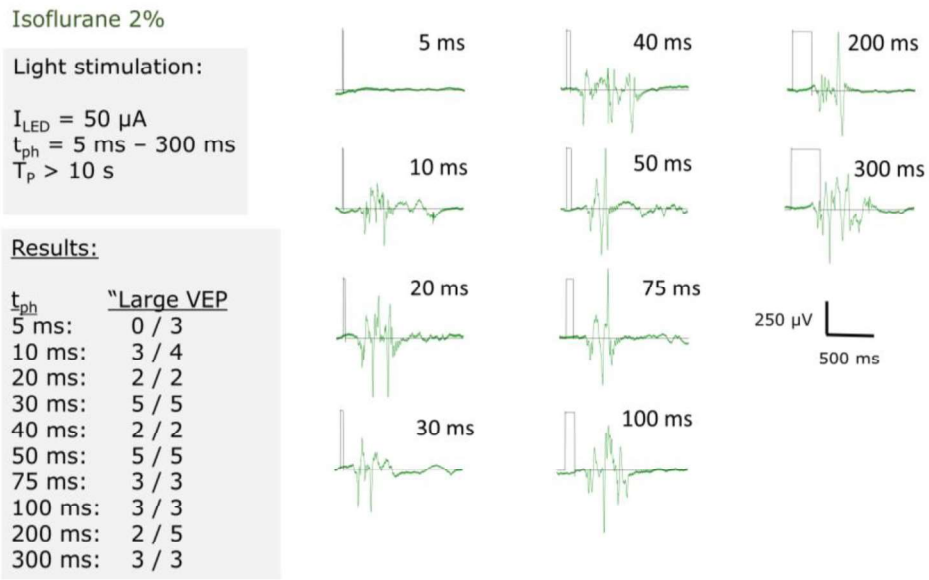

Figure 8.5: Estimation of the minimum length of light flash to evoke VEPs for a mouse under anaesthesia. The LED current was set to 50 µA.

8.6 Examples of VEPs

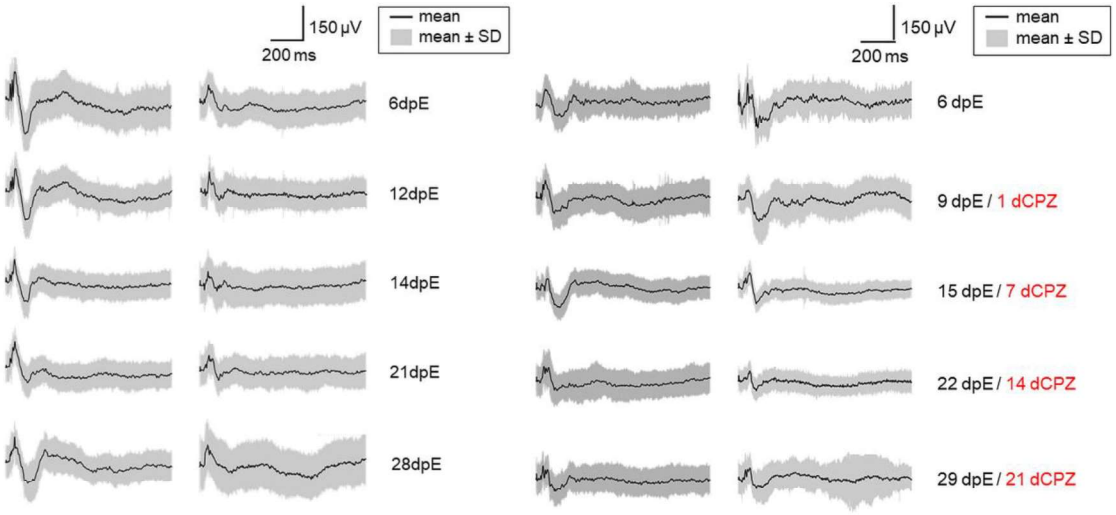

Figure 8.6: Examples of VEPs for different time points of two mice which were fed with normal food (left) and two mice which were fed with cuprizone food (right).

8.7 Head Holder

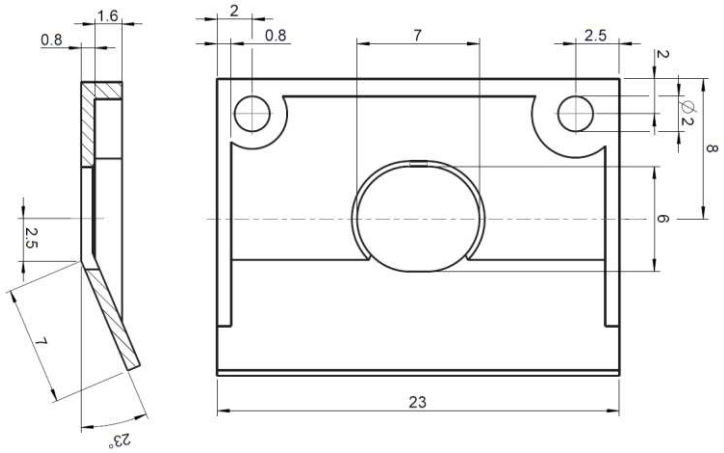

Figure 8.7: Technical drawing of the head holder for covering the electrode and fixation of the mouse under the 2P-LSM.

8.8 Rotation angles between the local and global coordinate system

The rotation angles between the electrodes related (local) coordination system and the microscope (global) coordinate system can be calculated using the following sequence:

- calculation of the normal vector $\vec{n}$ (see eq. 6)
- calculation of the tip angle α between the normal vector and the YZ-plane (global coordinate system) (see eq. 7)
- rotation of $\vec{n}$, $\vec{p}_1$, and $\vec{p}_2$ around the X-axis, resulting in vectors $\vec{n}\,'$, $\vec{p}_1{}'$, and $\vec{p}_2{}'$ (see eq. 8)
- calculation of the tilt angle β between the normal vector $\vec{n}\,'$ and the XZ-plane (see eq. 9)
- rotation of $\vec{n}\,'$, $\vec{p}_1{}'$, and $\vec{p}_2{}'$ around the Y-axis, resulting in vectors $\vec{n}\,'$, $\vec{p}_1{}''$, and $\vec{p}_2{}''$ (see eq. 10)
- calculation of the rotation angle γ between the vector $\vec{p}_1{}''$ and the X-axis using the unit vector $\vec{e}_x$ (see eq. 11)

$$\vec{\mathbf{n}} = \vec{p}_1 \times \vec{p}_2 = [n_x\, n_y\, n_z]^t \qquad \text{eq. 6}$$

$$\boldsymbol{\alpha} = \boldsymbol{arctan}\left({}^{n_y}\!/_{n_z}\right) \qquad \text{eq. 7}$$

$$\vec{n}\,' = \mathbf{R_X}(\boldsymbol{\alpha}) \cdot \vec{n}; \quad \vec{\mathbf{p}}_{1,2}{}' = \boldsymbol{R_X}(\boldsymbol{\alpha}) \cdot \vec{\mathbf{p}}_{1,2} \qquad \text{eq. 8}$$

$$\boldsymbol{\beta} = \boldsymbol{arctan}\left({}^{n'_x}\!/_{n'_z}\right) \qquad \text{eq. 9}$$

$$\vec{n}\,'' = \mathbf{R_Y}(\boldsymbol{\beta}) \cdot \vec{n}\,'; \qquad \vec{\mathbf{p}}_{1,2}{}'' = \mathbf{R_Y}(\boldsymbol{\beta}) \cdot \quad \vec{\mathbf{p}}_{1,2}{}' \qquad \text{eq. 10}$$

$$\boldsymbol{\gamma} = \boldsymbol{arccos}\left({}^{(\vec{p}_1{}'' \cdot\, \vec{e}_x)}\!/_{(|\vec{p}_1{}''| \cdot |\vec{e}_x|)}\right) \qquad \text{eq. 11}$$

The sign of the rotation angle γ has to be corrected with respect to the position of $\vec{p}_1{}''$ in the XY-plane because the definition range of $arccos$ is within [0; π]. An angle correction of α and β is not necessary because the imaging is always from the top of the mouse brain. Rotations around the X-, Y and Z-axes can be performed using the common three-dimensional rotation matrices $R_X(\alpha), R_Y(\beta)$, and $R_Z(\gamma)$.

$$\boldsymbol{R_x}(\alpha) = \begin{pmatrix} 1 & 0 & 0 \\ 0 & \cos(\alpha) & -\sin(\alpha) \\ 0 & \sin(\alpha) & \cos(\alpha) \end{pmatrix}$$

eq. 12

$$\boldsymbol{R_y}(\beta) = \begin{pmatrix} \cos(\beta) & 0 & \sin(\alpha) \\ 0 & 1 & 0 \\ -\sin(\alpha) & 0 & \cos(\alpha) \end{pmatrix}$$

eq. 13

$$\boldsymbol{R_z}(\gamma) = \begin{pmatrix} \cos(\gamma) & -\sin(\gamma) & 0 \\ \sin(\gamma) & \cos(\gamma) & 0 \\ 0 & 0 & 1 \end{pmatrix}$$

eq. 14

8.9 Change in electroplating temperature

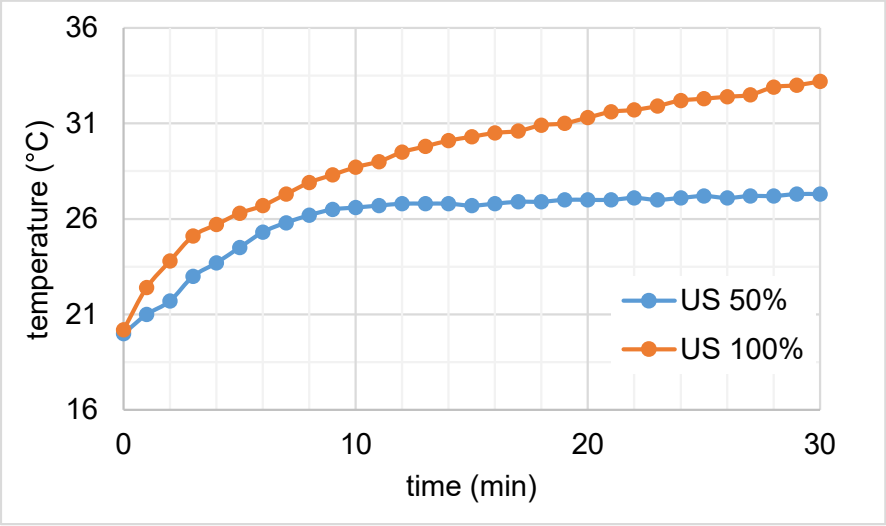

Figure 8.8: Temperature of the electroplating solution over time with ultrasound (US) power of 50% and 100% respectively.

9 List of publication

9.1 Publications

In preparation:

Schweigmann M, Caudal L, Stopper G, Scheller A, Koch KP, Kirchhoff F (2020) Versatile LCP surface microelectrodes for combining electrophysiology and in vivo neuronal and astroglial Ca^{2+}-imaging in the murine CNS.

Schweigmann M, Kirchhoff F, Koch KP (2020) Comparative study of platinum black electroplating to improve micro gold electrode arrays with LCP laminate.

Published:

Schweigmann M, Fabian Auler, Kirchhoff F, Koch KP (2018) Improving electrocorticograms of awake and anaesthetized mice using wavelet denoising. Current Directions in Biomedical Engineering 4(1):469-472. DOI: 10.1515/cdbme-2018-0112

Englert R, Rupp F, Koch KP, **Schweigmann M** (2017) Technical characterization of an 8 or 16 channel recording system to acquire spontaneous and evoked electrocorticograms of mice. Current Directions in Biomedical Engineering 3(2): 595–598. Doi: 10.1515/cdbme-2017-0124

Schweigmann M, Kirchhoff F, Koch KP (2016) Modeling and Simulations in Time Domain of a Stimulation Set-up for Cortical Applications. Eur J Transl Myol. 2016 Jun 13; 26(2):6017. doi: 10.4081/ejtm.2016.6017. eCollection 2016 Jun 13.

9.2 International conferences

Caudal LC, Stopper G, **Schweigmann M**, Bedner P, Steinhäuser C, Scheller A, Kirchhoff F (2019) *In vivo* contributions of astroglial GABAB receptors to pathological network function in temporal lobe epilepsy. XIV European Meeting on Glial Cells in Health and Disease

Schweigmann M, Caudal L, Stopper G, Scheller A, Koch KP, Kirchhoff F (2019) Exploring cortical brain networks with flexible LCP microelectrode arrays in parallel to two-photon imaging of anaesthetized and awake mice. 13th Göttingen Meeting of the German Neuroscience Society

Grochowski L, Kirchhoff F, Koch KP, **Schweigmann M** (2017) Detection of image plane orientation during two-photon laser scanning microscopy in brain tissue of mice using the geometry of stimulation and recording electrodes. Proceeding of Annual Meeting of the German Society for Biomedical Engineering

Caudal LC, Bai X, Bohn CV, Schlosser L, Stopper G, **Schweigmann M**, Scheller A, Kirchhoff F (2017) Contribution of glial transmitter receptors to pathological network function in mouse models of epilepsy. XIII European Meeting on Glial Cells in Health and Disease

Stopper G., **Schweigmann M**, Schlosser L, Scheller A, Koch KP, Kirchhoff F (2017) Recording and analysis of multi-modal brain signals in awake mice. XIII European Meeting on Glial Cells in Health and Disease

Schweigmann M, Schlosser L, Koch KP, Kirchhoff F (2017) A flexible surface microelectrode array to record electrical activity from neocortical neurons during two-photon imaging of astroglial Ca^{2+} signals in mice. XIII European Meeting on Glial Cells in Health and Disease

Schweigmann M, Kirchhoff F, Koch KP (2017) A Flexible Surface Microelectrode array to Investigate Stimulation Effects on Neuronglial Cortical Brain Networks with Two-Photon Imaging in Mice. 13th World Congress of International Neuromodulation Society

9.3 Meetings

Bai X, Stopper G, **Schweigmann M**, Schlosser L, Huang W, Scheller A, Kirchhoff F (2016) Role of the NG2 glial $GABA_B$ receptor in epilepsy. Meeting of ERA-Net Neuron Programme

Stopper G, **Schweigmann M**, Schlosser L, Scheller A, Koch KP, Kirchhoff F (2016) Novel technologies for recording spontaneous and evoked signals in the brain of awake mice. Annual Meeting DFG Priority Programme, Berlin

9.4 Local presentations

Schweigmann M (2019) LCP microelectrode arrays for use of electrophysiology in parallel with two-photon imaging in living mice. Presentation at the 2nd GradPro894 meeting, Homburg

Schweigmann M (2019) LCP Microelectrode for Health Research in the CNS of Mice. Presentation on the day of engineering at the Trier University of Applied Sciences, Trier

Schweigmann M (2017) Als Elektroingenieur mit Berufserfahrung zur Promotion? Warum nicht! Und darüber wie Elektrotechnik und Hirnforschung zusammen passen. Presentation on the day of engineering at the Trier University of Applied Sciences, Trier

Schweigmann M, Reiland R, Rupp F, Grochowski L, Koch KP (2017) Aufbau eines Labors zur Galvanisierung und Charakterisierung von Mikroelektroden für elektrophysiologische Medizingeräte und Implantate, Contribution on the event City Campus trifft Illuminale; Nächtliche Geistesblitze – Wissen schafft Licht, Trier

Schweigmann M, Koch KP (2016) MIRACLE - Multimodal Research and Instrumentation for Rehabilitation of Cells after Stroke and Traumatic Brain Injury. Presentation on the event 13. Nacht der Wissenschaft am Umweltcampus Birkenfeld, Birkenfeld

Schweigmann M, Lackas M, Scheller A, Kirchhoff F, Koch KP (2016) Untersuchung des Zellverbundes des zentralen Nervensystems mit Hilfe der 2 Photonen Mikroskopie und der Erfassung bioelektrischer Signale. Contribution on the event City Campus trifft Illuminale; Nächtliche Geistesblitze – Wissen schafft Licht, Trier

Schweigmann M, Bremm RP, Bernard F, Husch Andreas, Koch KP (2016) Kooperative Promotionen im Feld der medizintechnischen Neurowissenschaften innerhalb der Fachbereiche Technik und Informatik. Contribution on the event Science Meeting Trier University of Applied Sciences, Trier

10 Acknowledgement

Foremost, I would like to thank Prof. Dr. Frank Kirchhoff and Prof. Dr. Klaus Peter Koch for the exciting project and for their support being able to finish my PhD thesis. I thank you for the opportunity to work independently on a highly innovative and multidisciplinary topic in two powerful and fun-loving teams. I am very grateful for all opportunities to participate in scientific congresses that always allowed me to look beyond my own horizon.

I would like to thank all members of the departments Molecular Physiology and Electrical Engineering for their general support and the very good working atmosphere. With a good mood, appropriate calmness, and mutual support we were able to master all challenging situations. Thank you all for the various discussions stimulating new ideas.

Particular, I would like to thank Dr. Laura Stopper and Dr. Bogdan Catalin for their introduction in mouse handling, mouse surgery and in vivo 2P-LSM. I thank Dr. Anja Scheller for establishing the Nex-Cre x R26-CAG-lsl-GCaMP3 mouse line within the CIPMM, for introducing the mouse management software and for her work on the automatic slide scanner. I would like to thank Jörg Fusenig and Michael Lakas for their help in getting a warm start at Trier University of Applied Sciences. In addition, I would like to thank Ute Legler, Linda Meier and Frank Rhode being my first contact persons in organizational issues around orders and travels. Especially, I would like to thank Philip Rieder and Laura Caudal for performing surgeries and for having a great time during the jointly performed experiments. I am very grateful for the provision of the immunohistochemistry by Laura Caudal, which made is possible to prove the biocompatibility of the LCP electrodes.